

REPORT DOCUMENTATION PAGE				Form Approved OMB No. 0704-0188	
Public reporting burden for this collection of information is estimated to average 1 hour per response, including the time for reviewing instructions, searching existing data sources, gathering and maintaining the data needed, and completing and reviewing this collection of information. Send comments regarding this burden estimate or any other aspect of this collection of information, including suggestions for reducing this burden to Department of Defense, Washington Headquarters Services, Directorate for Information Operations and Reports (0704-0188), 1215 Jefferson Davis Highway, Suite 1204, Arlington, VA 22202-4302. Respondents should be aware that notwithstanding any other provision of law, no person shall be subject to any penalty for failing to comply with a collection of information if it does not display a currently valid OMB control number. PLEASE DO NOT RETURN YOUR FORM TO THE ABOVE ADDRESS.					
1. REPORT DATE (DD-MM-YYYY) 01/12/2012		2. REPORT TYPE Final Technical		3. DATES COVERED (From - To) 5/31/2010 - 5/31/2011	
4. TITLE AND SUBTITLE CARBON-NANOTUBE-BASED EPOXY MATRIX THERMAL INTERFACE MATERIALS FOR THERMAL MANAGEMENT IN LOAD BEARING AEROSPACE STRUCTURES				5a. CONTRACT NUMBER	
				5b. GRANT NUMBER FA9550-08-1-0372	
				5c. PROGRAM ELEMENT NUMBER	
6. AUTHOR(S) Vikas Prakash, Mike Bifano and Pankaj Kaul				5d. PROJECT NUMBER	
				5e. TASK NUMBER	
				5f. WORK UNIT NUMBER	
7. PERFORMING ORGANIZATION NAME(S) AND ADDRESS(ES) CASE WESTERN RESERVE UNIVERSITY 10900 Euclid Ave Cleveland, OH 44106				8. PERFORMING ORGANIZATION REPORT NUMBER	
9. SPONSORING / MONITORING AGENCY NAME(S) AND ADDRESS(ES) Air Force Office of Scientific Research Suite 325, Room 3112 875 Randolph Street Arlington, VA 22203-1768				10. SPONSOR/MONITOR'S ACRONYM(S) AFOSR	
				11. SPONSOR/MONITOR'S REPORT NUMBER(S) AFRL-OSR-VA-TR-2012-0895	
12. DISTRIBUTION / AVAILABILITY STATEMENT Distribution A - Approved for Public Release					
13. SUPPLEMENTARY NOTES					
14. ABSTRACT We report fabrication and thermal characterization of Sn-capped VA-MWCNT array composites for thermal management in load-bearing aero-structural applications. In order to obtain thermal characteristics of these multifunctional TIMs, we report measurements of thermal conductivity in VA-MWCNT-epoxy composites as well as in its individual constituents, i.e., bulk EPON-862 (matrix material), Sn thin film, and in individual MWCNTs taken from the same batch as the one used to fabricate the MWCNT-epoxy TIM. A 1-D multilayer thermal model that includes effects of thermal interface resistance is used to interpret the experimental results. The thermal conductivity of the MWCNT-epoxy composite was estimated to be about 5.8 W/m-K and exhibits a slight increase with temperature in the range 240 K to 300K. The results of this study suggests that inclusion of a Sn thin layer on the VA-MWCNT array as well as the morphological structure (defect state) of the individual MWCNT's are dominating factors that control the overall thermal conductivity of the TIM. These results are encouraging in light of the fact that the thermal conductivity of the composite can be increased by an order of magnitude by employing a high temperature annealing step.					
15. SUBJECT TERMS					
16. SECURITY CLASSIFICATION OF:			17. LIMITATION OF ABSTRACT UU	18. NUMBER OF PAGES 146	19a. NAME OF RESPONSIBLE PERSON Dr. Byung-Lip Lee
a. REPORT U	b. ABSTRACT U	c. THIS PAGE U			19b. TELEPHONE NUMBER (include area code) 703-696-8483

CARBON-NANOTUBE-BASED EPOXY MATRIX THERMAL INTERFACE MATERIALS FOR THERMAL MANAGEMENT IN LOAD BEARING AEROSPACE STRUCTURES

AFOSR Grant/Contract Number: FA9550-08-1-0372

PI: Prof. Vikas Prakash

Graduate Students: Mike Bifano and Pankaj Kaul

SPECIFIC PROGRAM OBJECTIVES

The specific objectives of the project were to design and develop novel multifunctional thermal interface materials (TIMs) comprised of carbon nanotubes (CNTs) and epoxy with a particular emphasis on understanding and improving thermal energy transport in load-bearing bonded aerospace structures.

To accomplish the goals of the proposal the following specific tasks were defined and pursued:

Task 1: Fabricate thin film VACNT/epoxy composites as thermal interface materials

Task 2: Characterize thermal conductivity in 2-D thin-film VACNT-epoxy composites. Various CNT diameters, volume fraction and interfacial characteristics will be investigated.

Task 3: Understand interfacial thermal contact resistance between 1-D CNTs and 2-D metal capping layers, e.g. tin thin film; Characterize thermal conductivity of individual metal capping layers; Characterize thermal conductivity of epoxy matrix material.

Task 4: Develop experimental procedures to characterize thermal conductivity of individual CNTs. Various CNT diameters and annealing conditions (graphitic condition of the CNTs) will be investigated.

Task 5: In support of tasks 1 ó 4, pursue analytical and numerical modeling to better understand thermal transport in nanowires and tubes and the VAMWCNT epoxy composites.

TECHNICAL PAPERS PUBLISHED AND/OR SUBMITTED ON THE PROJECT

- Kaul, P.B., Bifano, M.F.P and Prakash, P. "Multifunctional CNT-Epoxy composites for thermal energy management," Special Issue of the Journal of Composite Materials, (Submitted), (2011).
- Kaul, P. B. and Prakash, V. "Thickness and temperature dependent thermal conductivity measurement of nanoscale tin films," Paper No. IMECE2011-65576, Proceedings of the ASME 2011 International Mechanical Engineering Conference and Exposition, November 11-17, Denver, Colorado, USA (2011), pp. 1-10.
- Kaul, P. B. and Prakash, V. "Grain-boundary and twin-boundary scattering dependent thermal conduction in nanoscale tin films," Nanoletters, (Submitted).
- Bifano, M. F. P., Kaul, P., & Prakash, V. (2010). Application of elastic wave dispersion relations to estimate thermal properties of nanoscale wires and tubes of varying wall thickness and diameter. *Nanotechnology* **21** 235704
- Bifano, M. F. P., Kaul, P., & Prakash, V. (2011). The effect of heat treatment on the thermal conductivity of individual multiwalled carbon nanotubes. *Journal of Applied Physics*. (Accepted)
- Bifano, M. F. P., & Prakash, V. (2011). Thermal properties of nanowires and nanotubes with acoustically stiffened surfaces. *Journal of Applied Physics*. (Accepted)
- Bifano, M. F. P. & Prakash, (2011) Thermal Properties of Nanotubes and Nanowires with Acoustically Stiffened Surfaces, IMECE-13302, Proceedings of the ASME 2011 IMECE, Denver, Colorado.
- Bifano, M. F. P., Kaul, P. & Prakash, V. (2011) Thermal Conductivity of Heat Treated and Non-Heat Treated Individual Multiwalled Carbon Nanotubes, IMECE-65406, Proceedings of the ASME 2011 IMECE, Denver, Colorado.
- Bifano, M. F. P., Kaul, P. & Prakash, V., Roy, A. (2009) Application of Elastic Dispersion Relations to Estimate Thermal Properties of Nano-Scale Rods and Tubes of Varying Wall Thickness and Diameter, Proceedings of the ASME 2009 IMECE, IMECE-13302, Lake Buena Vista, Florida.
- P. B. Kaul, Bifano, M.F.P. and Prakash, V. (2011). "Multifunctional CNT-Epoxy composites for thermal energy management," 18th International Conference on Composite Materials, Jeju Island, Korea, pp. 1-6.

1. INTRODUCTION

Thermal management at structural interfaces operating in high thermal environments, such as, supersonic and hypersonic air and space vehicles, have initiated a demand for high performance load-bearing thermal interface materials (TIMs). When two nominally flat surfaces come together at a typical material interface, the solid-solid contact area is limited to 1-2% of the apparent contact area due to surface asperities [1]. As a consequence, heat conduction through the contact junctions and the medium surrounding the non-contact area provide parallel paths for heat flow. Ideally, TIMs are designed to fill the space in place of surrounding medium, requiring them to be highly thermally conducting and also to effectively wet the bounding surfaces. However, real TIMs have a finite thickness (called the bond-line thickness, BLT), and invariably involve dissimilar material surfaces with the bounding surfaces. Moreover, they do not completely wet the surfaces, resulting in gaps with contact resistances at the two bounding surfaces.

For a typical TIM with a bond-line thickness BLT and an effective thermal conductivity k_{TIM} , the total thermal resistance across an interface can be written in terms of the thermal interface contact resistances on either side of the TIM, R_{c1} and R_{c2} , as

$$R_{Total} = R_{c1} + \frac{BLT}{k_{TIM}} + R_{c2} . \quad (1)$$

In order to make the TIM effective, the broader goal of thermal management is to minimize the total thermal interface resistance across the TIM by reducing BLT and increasing k_{TIM} , and minimizing the interfacial contact resistances R_{c1} and R_{c2} , at the bounding surfaces to the TIM.

Particle-laden polymers are one of the most prominent TIMs used in the electronics cooling industry today. As described in Equation (1), the thermal contact resistance of such material systems is not only dependent on the thermal conductivity of the TIM, but also on the bond line thickness (BLT). Prasher et al. (2006) [2] introduced a rheology based semi-empirical model for the prediction of the *BLT* of these TIMs. The *BLT* was modeled to depend on the yield stress of the particle-laden polymer and the applied pressure. The *BLT* model was then combined with a thermal conductivity model to estimate the total effective thermal resistance of the particle-laden polymer TIMs that includes factors, such as, base polymer (matrix) viscosity, particle volume fraction and shape, and particle boundary resistance, etc. The analysis showed that there exists an optimal filler (particle) volume fraction at which the total thermal resistance of the particle laden TIM becomes a minimum.

Recent studies indicating relatively high intrinsic thermal conductivities in single-walled and multi-walled carbon nanotubes as well as other graphite materials [3-11], suggests that these nano-structured materials and their combinations are promising candidate materials for the development of high-performance TIMs. The earliest attempts[12] for the use of randomly orientated SWCNTs as filler materials in oil suspensions reportedly increased the effective thermal conductivity of nanotube-in-oil suspensions by 2.5 times over that of the base fluid (matrix) with only 1% volume fraction of carbon nanotubes. Another study[13] involving randomly orientated SWCNT in an epoxy matrix reported enhancements in thermal conductivity of nearly 125%, while the vapor-grown carbon-fiber (VGCF)-epoxy composites exhibited an enhancement of 45% in thermal conductivity when compared to the neat epoxy for the same loading (1 wt%). However, the maximum thermal conductivity achieved by randomly orientated carbon nanotube composites was still less than 1 W/m-

K. This surprisingly low value has been attributed to the substantially weak thermal cross-linking between contacting nanotubes [14].

In recent years, vertically aligned multiwalled nanotube arrays have generated much interest since by placing CNTs perpendicular to and spanning the system components, there is a lesser number of CNT/epoxy interfaces in the through-thickness direction, thus minimizing the effective thermal interfacial resistance between the CNTs and the epoxy matrix. Assuming the epoxy matrix does not affect the heat transport through individual MWCNTs, it is expected that the overall thermal conductivity of the composite may be enhanced by the intrinsically higher thermal conductivity of the MWCNTs.

Thermal transport through vertically aligned multi-walled carbon nanotube (VA-MWCNT) arrays [15] has been observed to be highly anisotropic. The longitudinal diffusivity was reported to be 72 times that of the in-plane value, signifying their worth as 1-D heat pipes between two contacting surfaces. A similar study over a wider temperature range 180K - 300K [16, 17] have reported thermal diffusivity measurements along the alignment direction in a VA-MWCNT array (20-50 nm diameter, 1.64 mm long) to be 25 times higher than that across the transverse direction. Choi *et al.* (2003)[14] reported enhancement in thermal conductivity of SWCNT-epoxy composites by nearly 300% at 3 wt% loading of randomly dispersed SWCNTs, and an additional 10% enhancement in thermal conductivity after applying a magnetic field during processing to improve nanotube alignment. The maximum room temperature thermal conductivity obtained after magnetic alignment during processing was about 6.5 W/m-K, which was much higher those reported in

previous studies. These results indicate that vertically aligned CNTs which are in isolation from each other have a potential to serve as promising candidates as TIMs.

With regards to VAMWCNTs, Ivanov *et al.* (2006) [15] reported a thermal conductivity of 5.5 ± 0.7 W/m-K for an epoxy-infiltrated VA-MWCNT array (8 ± 1 vol %, 2mm long) and 6.4 ± 0.8 W/m-K of the same array in air. Borca-Tascuic *et al.* (2007) [17] reported a maximum thermal conductivity of 3.8 W/m-K in a MWCNT array-polymer composite along the alignment direction at room temperature with 2% volume fraction of aligned MWCNTs. Xuejiao *et al.* (2004) [18] and Tong *et al.* (2004) [19] proposed the use of CNTs along with other conventional TIM filler materials in a polymer matrix, and vertically oriented growth of CNTs on both contacting surfaces to form a CNT-CNT interface in between them. Hu *et al.* (2007) [20] characterized the thermal interface resistance of CNT-CNT interfaces using diffraction limited infrared microscopy. They reported a thermal interface resistance of the CNT-based interface structure to be much below expectations at 3.8×10^{-4} K-m²/W. Xu and Fisher (2005) [21] experimentally evaluated a minimum thermal resistance of 2×10^{-5} Km²/W for a dry joint of VA-CNT array in between Cu and Si, which is very close to that of TIM comprising indium and CNT. However, incorporating a phase change material (PCM) into a VA-MWCNT array yielded a lower thermal resistance of 5.2×10^{-6} Km²/W. More recently, Cola *et al.* (2007) [22] measured the thermal resistance across (a) one-sided (Si-MWCNTs-Ag), wherein carbon nanotubes are grown on one of the bounding surface; and (b) two-sided (Si-CNT-CNT-Cu) MWCNT arrays. For the one-sided interface the total interfacial thermal resistance was found to be dominated by the thermal resistance of the CNT-Ag interface and was measured to be 1.4×10^{-5} Km²/W, while the thermal resistance of the two-sided configuration was dominated by the interface resistance between the free tips of the mating CNT arrays, and was measured to be an

order of magnitude lower at $2 \times 10^{-6} \text{ Km}^2/\text{W}$. A potentially promising variation of the two-sided CNT interface was the introduction of a thin deformable foil in between the nanotube ends of the CNT-CNT arrays such that the foil could adjust to the deformation of CNTs with far field pressure. In this way, using a 10 μm thick Cu foil (with MWCNT on both sides) the thermal interfacial resistance of a rough Cu-Ag interface was observed to be greatly reduced [23].

Recent works by Shaikh (2007) [24] and Cola (2007) [22] have explored through-thickness thermal conductance in systems comprising CNTs on glass, copper and silicon substrates. In these systems it was hoped that the weld-contacts made via the catalyst during synthesis of vertical aligned MWCNT arrays would be better than simple Van der Waal type bonds. However, it was found that even in the best case scenario, the CNT-substrate contact resistance was still quite high. Tong *et al.* (2007) [25] and Sihn *et al.* (2008)[26] used a combination of MWCNT array with thin gold and indium capping layers to improve the thermal conductance between the MWCNT array and the bounding surfaces; the thermal conductivity of the joint (device) was observed to increase by more than 1-2 orders of magnitude compared to the absence of the TIM.

Encouraged by these findings, in this paper we report the development of vertically-aligned multi-wall carbon nanotube (VA-MWCNT) array composites for thermal management in load-bearing structural applications. Unlike previous studies on the use of VA-MWCNT-based thermal interface materials for essentially non-load bearing thermal management applications, the TIMs of interest here involve the use of VA-MWCNTs in an epoxy matrix. The epoxy matrix imparts mechanical strength to these systems while the VACNTs provide avenues for high through-thickness thermal conductivity across a typical material interface. It is assumed that the thermal

properties of the aligned MWCNTs in the epoxy matrix are similar to those of individual free standing MWCNTs. Furthermore, we introduce a transition zone (TZ) comprising of a tin thin film at the interface between the MWCNTs and the surrounding material (SiO_2) to minimize the thermal impedance mismatch and thermal resistance due to interfacial roughness. Figure 1 shows a schematic of our proposed Sn-VA-MWCNT/epoxy TIM system. The overall thermal resistance of the TIM is expected to be governed by the interfacial thermal contact resistance between the bounding solids and the mating surfaces of the Sn VA-MWCNT/epoxy layer. These interfaces are generally neither fully conforming nor smooth and thus, may lead to a significant increment in the total thermal contact resistance.

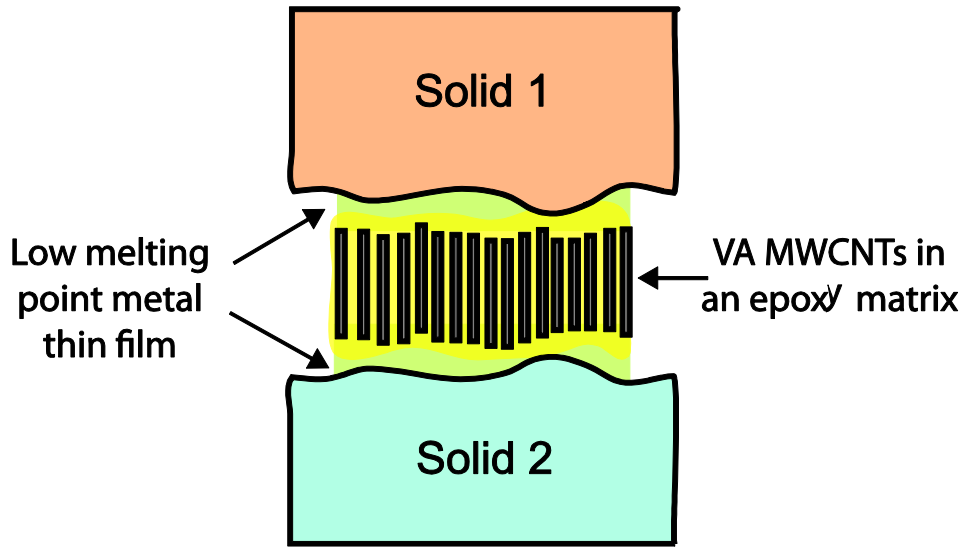


Figure 1: Schematic of VA-MWCNT TIM. The TIM facilitates heat transport between bounding solids (solid 1 and solid 2). A low melting point (Sn) thin film (green) fills the transition zones between the CNT-polymer/solid interfaces.

In particular, we obtain the thermal conductivity of the Sn-coated VA-MWCNT epoxy device over a temperature range of 240 K- 300 K using the three omega method. In order to estimate the

thermal conductivity of the VA MWCNT epoxy composite as well as the thermal interfacial resistance at the various layer interfaces, we characterize thermal conductivity in individual constituents of the VA-MWCNT composite, namely (1) individual free standing nanotubes selected from the same VA-MWCNT array as that used in the fabrication of the VA-MWCNT-epoxy composite; (2) the epoxy matrix; and (3) Sn thin films (capping layer) of 500 nm thickness. These measurements will be used in conjunction with a 1-D multilayer thermal model based on Feldman's notation [27] to estimate the thermal conductivity of the CNT-epoxy composite as well as the thermal interfacial resistance between the layers.

2. MATERIALS AND METHODS

2.1. Sample Processing

The VA-MWCNT arrays used (Figure 2a and Figure 2b) in the present investigation were procured from the laboratories of Prof Dai at Case Western Reserve University and Prof Shanov at the University of Cincinnati. In Prof Dai's laboratory, VA-MWCNT arrays (LD Samples) are grown via pyrolysis of iron (II) phthalocyanine (FePc) in Ar/H₂ at 900 °C on a silicon wafer. [28, 29] These MWCNTs are ~ 25-80 nm in diameter and have lengths varying from 2.25 mm in the middle of the turf to 2.9 mm at the edges. VA-MWCNT arrays procured from Prof. Shanov's laboratory (UC samples), were synthesized using water-assisted chemical vapor deposition (CVD) [30-32]. The nanotube diameter of the water-assisted CVD arrays varied from 15-45 nm.

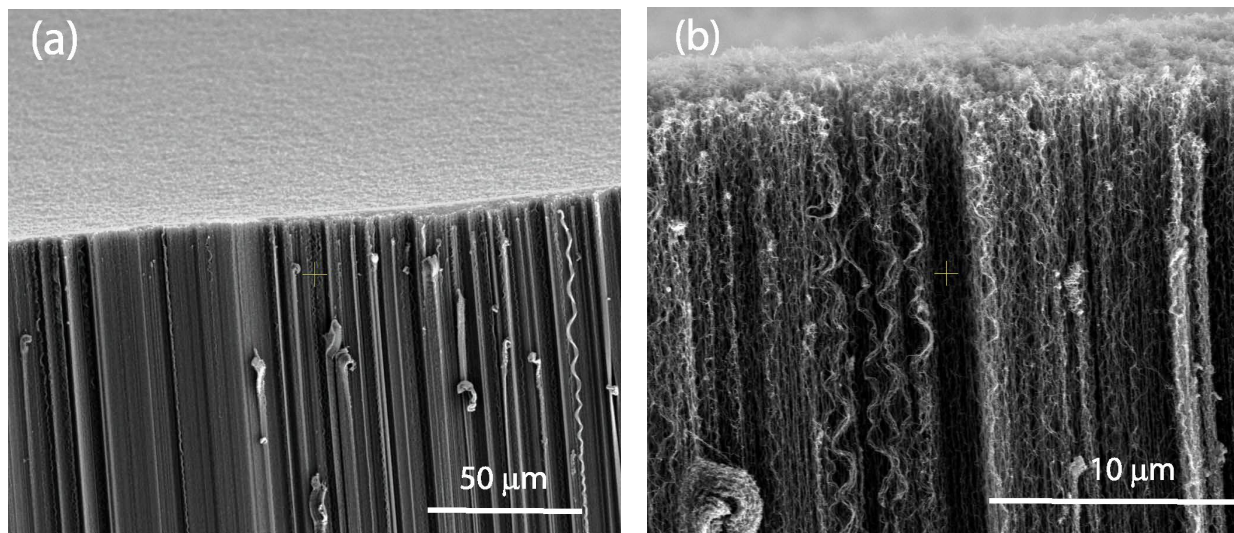


Figure 2: SEM micrographs of VA-MWCNT arrays prepared by thermal CVD taken at two different magnifications (a) 740X and (b) 6200X showing the region near CNT tips.

The epoxy-based carbon nanotube composites were fabricated in our laboratory by immersing the MWCNT array into a solution of Epon 862 epoxy, EPICURE curing agent W, and an acetone solvent. Prior to immersion of the VA-MWCNT array, the Epon 862 epoxy is ultrasonicated for approximately 8 minutes. The solution is poured onto the VA-MWCNT array and then spin-coated to allow the epoxy to infiltrate the array. The volume fraction of nanotubes in the composite is estimated to be 8%. Degassing is performed under high vacuum (30 in of Hg) to remove the bubbles generated during mixing. After casting the MWCNT/epoxy composite, both surfaces are cut and lapped. The surfaces are then sequentially polished at 100-150 rpm with 15, 6, 1 and 0.1 μm diamond abrasives while applying a 5 N constant force.

Atomic force microscopy (AFM) topology measurements (Figure 3d, 3e, and 3f) indicate that the polishing process reduces the roughness of the samples from nearly 1 μm to 100 nm or less. Following polishing, the sample is ethanol washed and air-dried. The MWCNT tips are

exposed from the epoxy by reactive ion etching (RIE) using O_2 plasma with 13.5 MHz 125 W RF power for 6-8 min. Once the tips are exposed, a thin layer of tin of thickness $\sim 500 \pm 50$ nm is deposited using RF sputtering at 2×10^{-7} Torr.

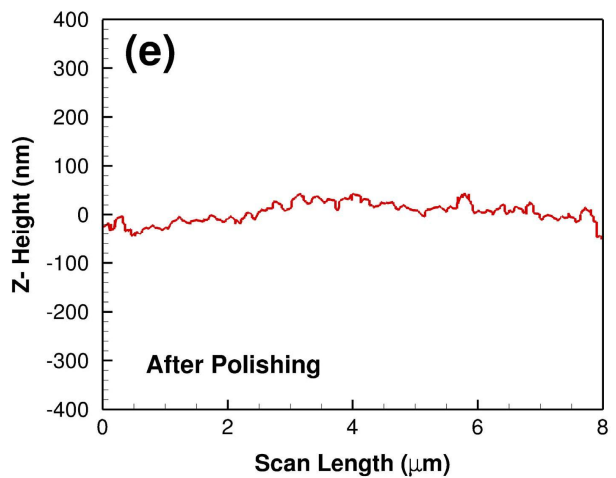
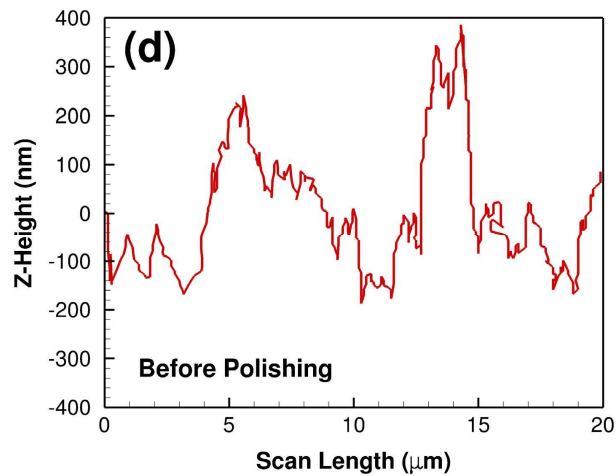
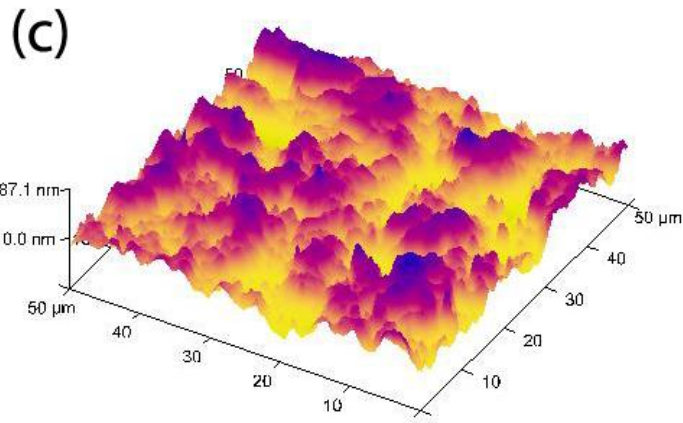
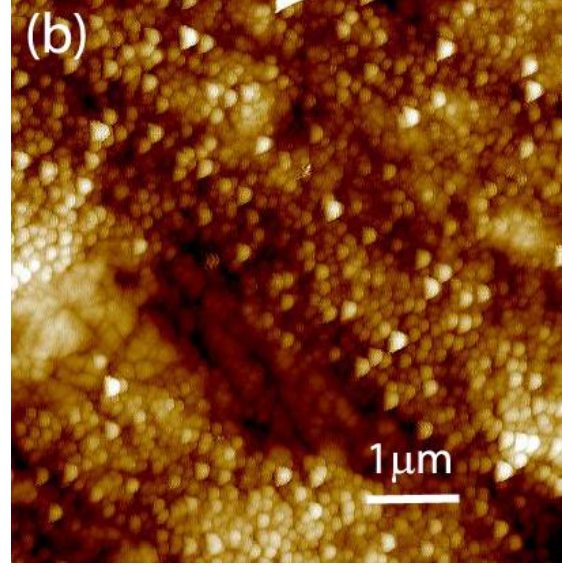
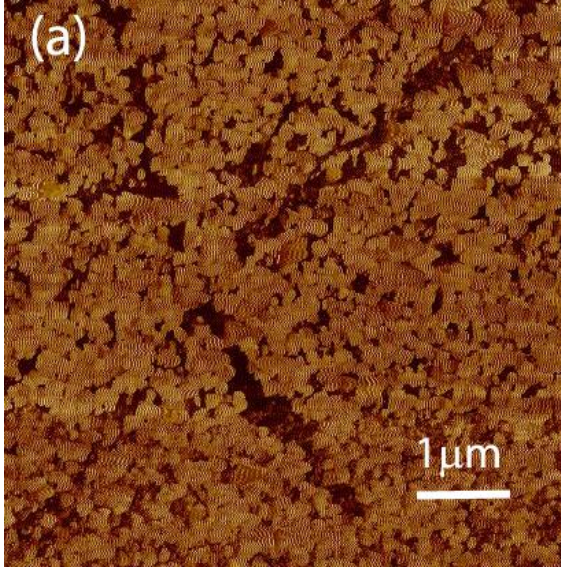


Figure 3: (a) AFM Phase imaging of MWCNT-Epoxy composite before plasma-etching; (b) Tapping mode AFM reveals CNT tips exposed after plasma-etching on composite; (c) 3D view of roughness characteristic on top surface of epoxy before polishing using AFM; (d) Surface topology of epoxy composite before polishing indicating roughness 600nm-1 μ m; (e) Surface topology traced by AFM tip on composite sample after polishing indicating roughness of the order \sim 100nm.

2.2. The ‘T’ Type Wollaston Probe Method for Individual Nanotubes

The thermal conductivity of an individual MWCNT is measured using a three-omega-based Wollaston T-Type probe inside a scanning electron microscope (SEM). Details regarding these measurements are presented in APPENDIX 1 of this report. Figure 4 depicts the Wollaston probe wire's temperature profile (a) before the specimen is placed in contact, and (b) following contact with the specimen. The drop in spatially averaged temperature causes a reduction in electrical resistance, and thus a measureable voltage decrease. The resistance response of the probe wire is determined from the voltage response since the heating current amplitude is known.

The probe wire's temperature response is first calibrated by measuring the electrical resistance versus power input in the absence of the sample. Subsequently, once a sample is attached, the change in the measured electrical resistance versus power input of the probe wire is correlated to a decrease in the probe wire's average temperature rise due to the heat flux into the sample. Since the opposing end of the sample is maintained at the base (ambient) temperature, in effect, the temperature drop and heat flux into the sample can be estimated, and the sample's thermal resistance is determined.

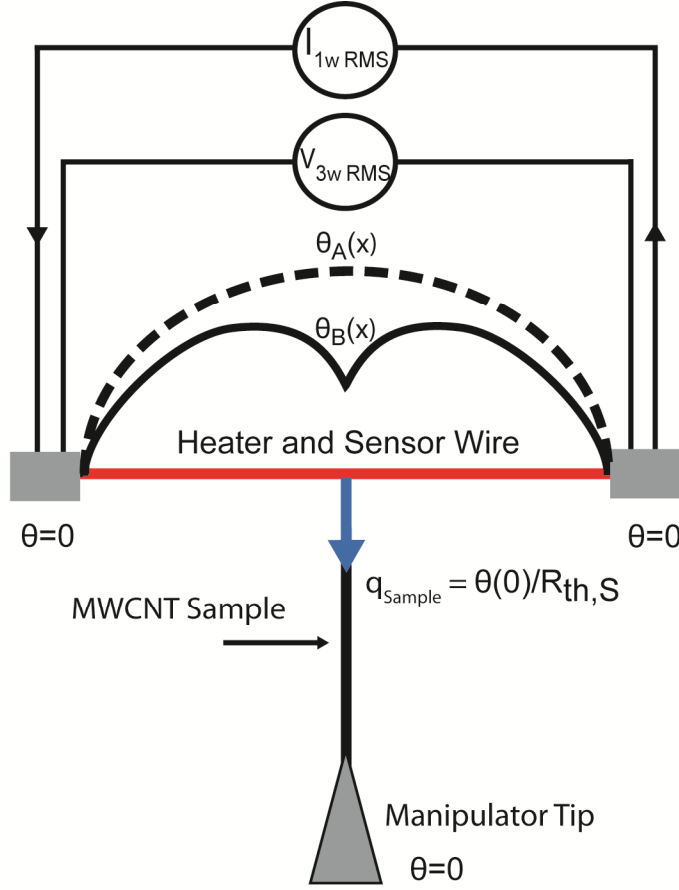


Figure 4: Schematic of the Wollaston probe wire. The probe wire is Joule heated with a power of Q_{RMS} , by the low frequency current, $I_{1\omega RMS}$. $\theta_A(x)$ is the temperature response of the probe wire prior to making contact with the sample of unknown thermal conductivity. Following contact with the sample, the temperature response of the probe wire is $\theta_B(x)$. The measured third harmonic voltage, $V_{3\omega RMS}$, is a function of the probe wire's thermal resistance, zero current electrical resistance R_{eo} , Q_{RMS} , and the thermal resistance of the sample. The sample's thermal conductivity is determined by measuring the sample's thermal resistance and dimensions.

Instead of DC Joule heating and voltage measurements, the probe wire is Joule heated with a low frequency sinusoidal AC current, $I(t) = I_{1\omega} \sin(\omega t)$, where $I_{1\omega}$ is the current amplitude. The initial electrical resistance of the probe wire is R_{eo} . Joule heating at 2ω , $Q(t)$, drives in phase temperature oscillations, $\bar{\theta}(t)$, which are proportional to $Q(t)$, by a thermal transfer function Z_o . The 2ω temperature oscillations create oscillations in electrical resistance by

$R_e(t) = R_{eo} [1 + \alpha \bar{\theta}(t)]$, where α is the measurable temperature coefficient of resistance of the probe wire. Since the heating current is $I(t) = I_{1\omega} \sin(\omega t)$, the voltage response of the probe wire is expected to be a combination of both the 1ω and 3ω frequency harmonics of the initial heating current and is given by,

$$\begin{aligned} V(t) &= I(t)R_e(t) \\ &= \left[I_{1\omega} R_{eo} + \frac{3}{4} \alpha Z_o R_{eo}^2 I_{1\omega}^3 \right] \sin \omega t - \left[\frac{1}{4} \alpha Z_o I_{1\omega}^3 R_{eo}^2 \right] \sin 3\omega t \end{aligned} \quad (2)$$

A Lock-in Amplifier is used to measure the specific RMS value of the three-omega component. The measurable 3ω RMS voltage response from Equation (2) may be re-written as

$$V_{3\omega, RMS} = \frac{1}{2} \alpha Z_o I_{1\omega, RMS} R_{eo} Q_{RMS}, \quad (3)$$

where $Q_{RMS} = I_{1\omega, RMS}^2 R_{eo}$.

If $R_{e3\omega, RMS} \equiv V_{3\omega, RMS} / I_{1\omega, RMS}$, Z_o is determined from the measured slope of $\delta R_{e3\omega, RMS} / \delta Q_{RMS}$. The thermal resistance ratio of probe to the sample, $R_{th,P} / R_{th,S}$, is embedded inside the thermal transfer function Z_o . By modeling the temperature response of the probe wire as a function of $R_{th,P} / R_{th,S}$, a theoretical value of Z_o is compared to the experimental value. Initial calibration in the absence of the sample is used to first determine $R_{th,P}$, and a subsequent measurement in the presence of the probe wire is used to determine $R_{th,S}$. The samples thermal conductivity is calculated by $k_S =$

$L_s/R_{th,s} A_s$, where the sample cross sectional area A_s and Length, L_s is measured using the SEM beam.

2.3. Three Omega Method for Thin Films and Composites

Similar to the measurements performed on individual MWCNTs, the 3ω method is performed by passing a current with angular frequency ω through a heater/sensor micro-fabricated on the sample. The heating current creates Joule heating and thus a temperature oscillation at a frequency 2ω . Subsequently, the metal heater/sensor's electrical resistance also oscillates at 2ω , causing a measureable 3ω voltage oscillation detected using a lock-in amplifier. The 3ω voltage oscillations are used to determine the sample's thermal properties [33, 34]. The frequency range for the experiment is chosen by examining the relationship between the film thickness, the thermal penetration depth of interest, and heater width. Large heater widths (when compared to sample or film thickness) produce a one-dimensional heating profile, thereby providing information about the cross-plane thermal conductivity.

For electrically conductive samples a thin insulating film must be deposited prior to the metal line deposition to provide electrical isolation. For this work, a thin film of 350 nm SiO_2 was deposited using low temperature plasma enhanced chemical vapor deposition (PECVD). The SiO_2 serves as an insulator for all thin films and composite samples evaluated in the present study. For conducting the experiments, an approach similar to the differential three omega [35-37] method was utilized to measure the thermal conductivity of a ~500 nm thin Sn film, bulk EPON-862 epoxy film, and VA-MWCNT-epoxy composite samples, with the same heater material (Aluminum) and width on them. Additionally, in order to restrict the error introduced

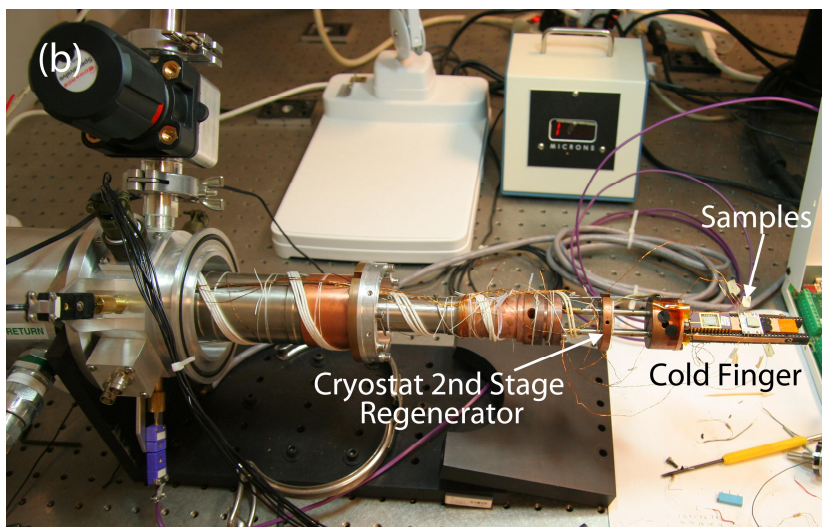
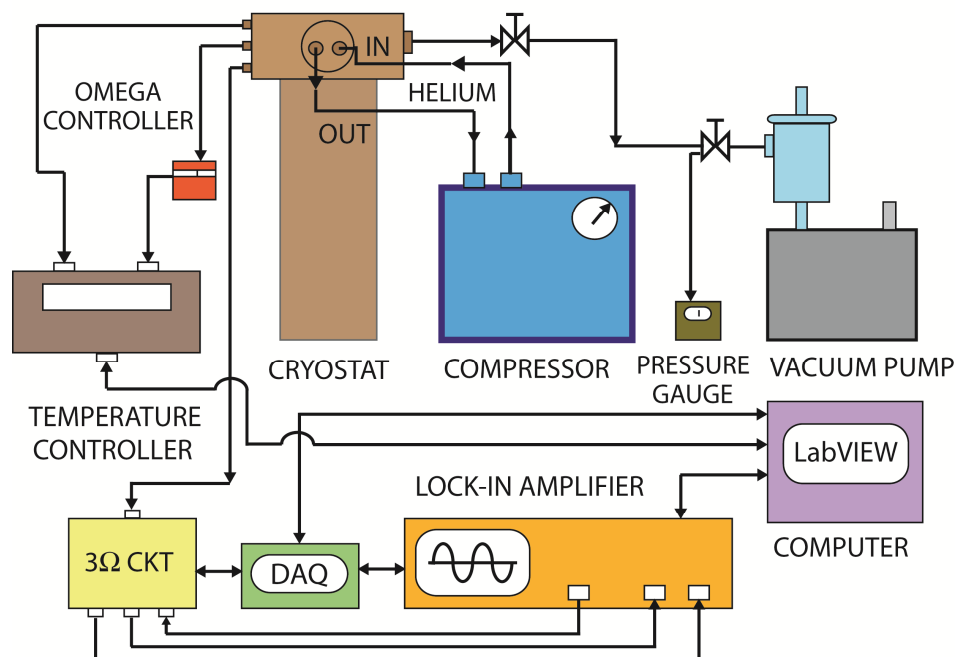
by various approximations, the numerically obtained exact solution of the film on substrate system, as described by Kim *et al.*[38] , Borca-Tascuic *et al.* [35] and more recently by Tong *et al.* [37], has been used.

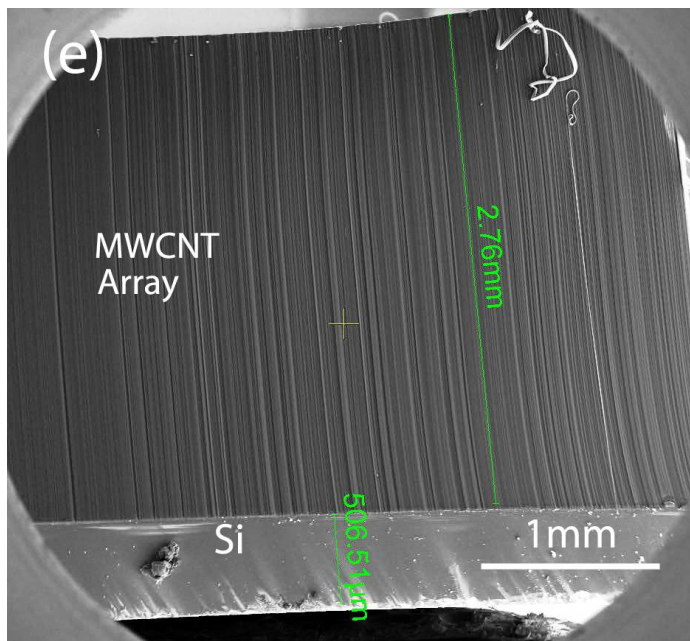
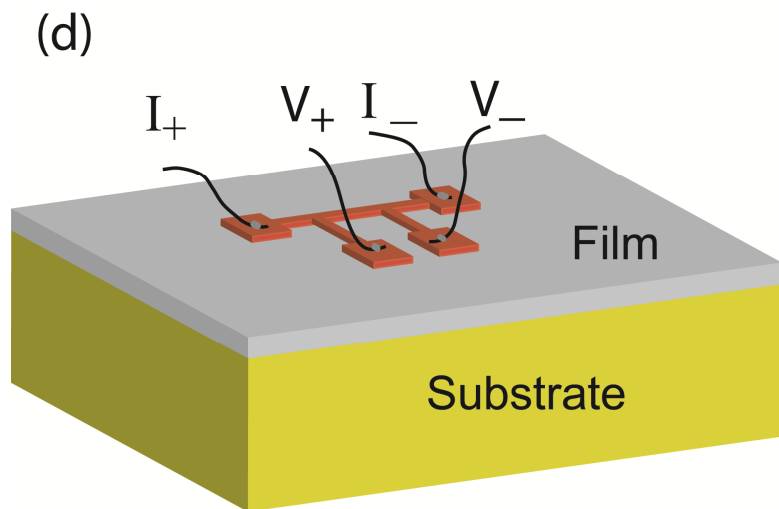
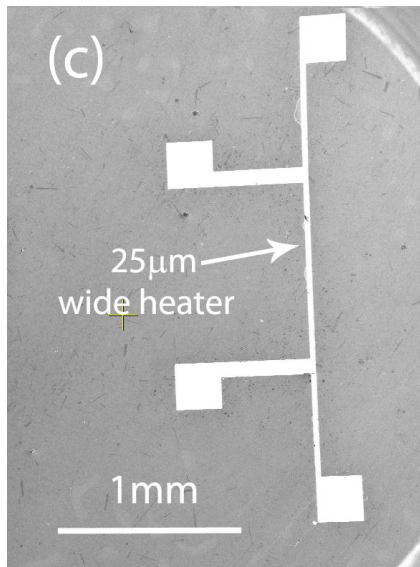
The analytical procedure for interpreting the three omega experiments is based on an earlier work by Cahill and Pohl [39], and requires the assumptions that the heater be considered of infinite length and that the sample be effectively semi-infinite. Additionally, the method requires the thermal waves to penetrate a depth greater than the heater width into the sample, satisfying the approximation of an infinite line source. The three-omega method is applied to a film on a substrate type configuration, by employing either the slope method or the differential- 3ω approach. For these methods, the thin film is assumed thin enough such that essentially one- dimensional Fourier conduction model can be applied for analysis and interpretation of the experimental data. Specific conditions that must hold to ensure accurate analysis are that $d_f > 2b \gg L_f$, i.e., the thermal penetration depth, d_f , must be greater than the heater width and be much larger than the film thickness, L_f . For the experimental investigation discussed herein, the thermal penetration depth and the heater width were greater by at least an order of magnitude than the film thickness to ensure the validity of these approximations. Additionally, the thickness of the underlying substrate L_s must be such that the condition $L_s \gg d_f \gg 2b$ is maintained to avoid back surface reflection and assure the validity of the line source and semi-infinite substrate approximations. The thermal conductivity of the 3 mm epoxy (EPON-862) sample is measured using the analytical solution mentioned in Cahill (1990) for a narrow line source on a semi-infinite substrate. The thermal conductivity of a 500 nm thin tin film is measured by comparing the total amplitude and phase signal of temperature oscillations with a

theoretically obtained solution in thin layer limit using Tong's (2006)[37] two layer model. However, for the experimental work on VA-MWCNT composites, a three-layer model based on Feldman's algorithm (Feldman, 1999) has been derived and is used to interpret the experimental results. Additional details about the three omega technique can be found from various references [33-39], and are therefore not discussed in detail here.

The main components of the 3ω set-up used for this work are, (i) a cryostat (Janis Research Model: CCS-400H/204); (ii) a temperature controller that serves to regulate the sample temperature; and (iii) a lock-in amplifier to detect the voltage response of the heater (Fig. 5). The cryostat is capable of operating between the temperatures 10K to 500K. An RV-8 rotary vane pump capable of developing a vacuum equal to 10^{-4} torr or less is utilized. A silicon shadow mask is batch fabricated using conventional lithography technique. The aluminum metal heater/sensor line is magnetron sputtered through this micro-fabricated shadow mask. The temperature coefficient of resistance of the heater/sensor line is measured prior to every experiment. The set-up has been automated using LabVIEW 8.5. The bits of the multiplying DAC (AD 7541 KN) are set 'on' and 'off' to balance the first harmonic signals from the sample and reference resistor. Moreover, the LabVIEW program helps in balancing the first harmonic voltage at the reference resistor and the sample resistor to a greater degree of precision and subsequently extract third harmonic voltage signals in order to determine the temperature rise in the heater/sensor.

(a)





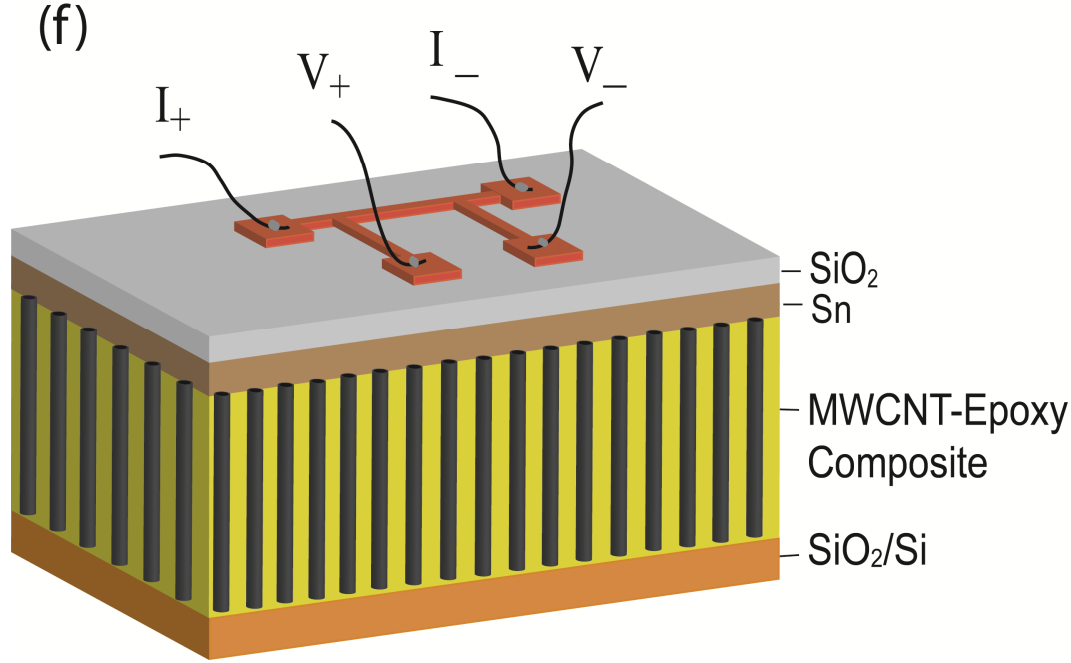


Figure 5: (a) Schematic of Cryostat Setup@ Nanomechanics Lab, Case Western; (b) Composite sample loaded on a cryostat after laying microfabricated heaters on top; (c) Microfabricated 25 μ m wide heater with 250 μ m x 250 μ m pads attached for wire-bonding; (d) Schematic of conventional 3-Omega measurement for film on substrate configuration used for measuring tin films (e) VA-MWCNT array on silicon wafer; and (f) Schematic of 3-Omega configuration utilized for measuring VA-MWCNT composite.

3. RESULTS AND DISCUSSION

An understanding of thermal transport in a VA MWCNT-epoxy based TIM in an adhesively jointed structure must involve thermal conductivity measurements in the individual components, including the epoxy matrix, the thin tin capping layer, and the VA-MWCNT-epoxy composite. Additionally, where-ever possible, the thermal measurements are performed at lower temperatures so as to investigate the effects of increased phonon mean free path lengths on thermal conductivity.

3.1. Thermal Conduction in individual Carbon-nanotube

In the present study, thermal conductivity of individual multiwalled carbon nanotubes taken from the same sample batch array UC01, are measured at room temperature. The average thermal conductivity of an individual nanotube from the UC01 batch is ~ 60 W/m-K. In a recent study [40], the authors have measured the thermal conductivity of individual multiwalled nanotubes from both heat-treated and non-heat-treated sample groups showing an approximate 5 fold increase in thermal conductivity with heat treatment. Heat-treatment was performed at 3000 °C for 20 hours in an argon gas atmosphere. Moreover, for one of the heat-treated samples thermal conductivity as high as 730 ± 153 W/m-K was obtained.

Qualitative assessments of residual amorphous carbon and defects were made by observing the Raman peak intensities of the *D* and *G*-bands. The *D* band (defect band) is known to be activated by both carbonaceous impurities with sp^3 bonding and fragmented sp^2 bonds [41, 42], both being features of MWCNT defects. The *G* band is activated by contiguous sp^2 bonding, *i.e.*, a high degree of crystallinity [41, 42]. Therefore, when comparing the two sample groups, a smaller *D/G* band ratio is representative of a sample with fewer defects and a higher degree of graphitization. The authors have shown that significant increase in thermal conductivity had a strong correlation to the reduced *D/G* Raman peaks. The average Raman *D/G* ratio for heat-treated samples was 0.21 ± 0.04 , while the non-heat-treated group had an average *D/G* ratio equal to 0.69 ± 0.15 . Note that the UC01 samples are not heat-treated and Raman scattering reveals a *D/G* ratio of 0.84 (Figure 6b). The reduced value of thermal conductivity

measured in the UC01 sample correlates well with the non-heat-treated sample group with higher D/G Raman ratios.

Thermal conductivity is undoubtedly expected to improve with increased crystallinity and a decreased density of phonon scattering sites. Andrews *et al.* (2001) [43] had observed marked structural and chemical improvements in MWCNT sample quality with heat-treatment. It was observed that annealing temperatures reduced the residual Fe catalyst (essential for CVD growth of MWCNTs) from 7.1% by wt. to 0.1%. Moreover, it was reported that the temperatures as high as 3000°C healed the sidewall defects evident from the reduced inter-layer spacing between grapheme shells confirmed by x-ray diffraction (XRD) and transmission electron microscope (TEM).

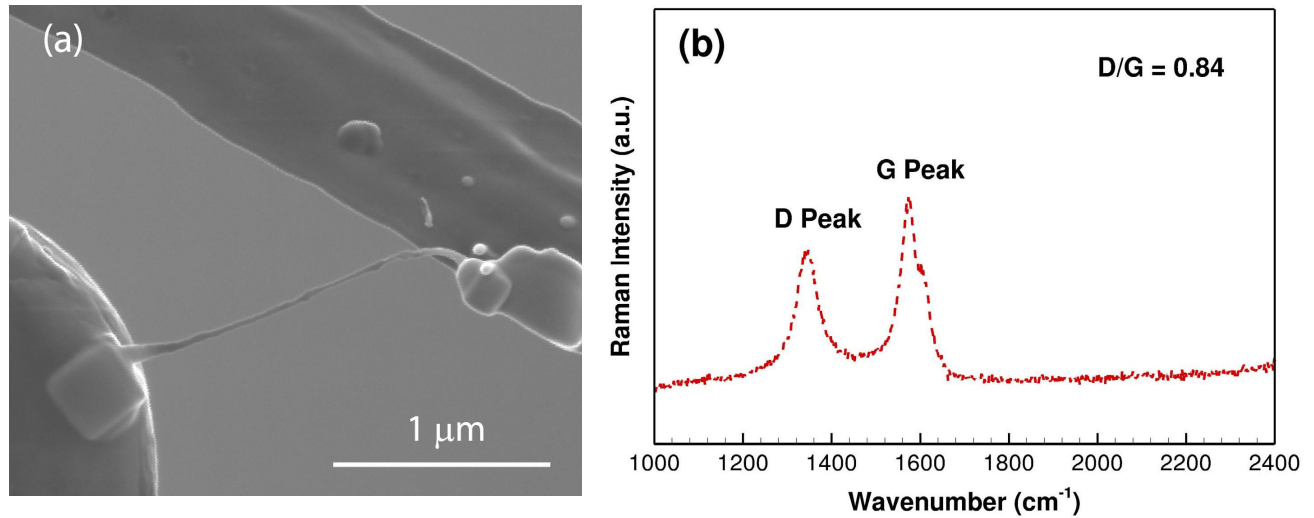


Figure 6: (a) SEM micrograph of thermal conductivity experiment on an individual MWCNT selected from the UC01 sample group. (b) Raman intensity with excitation wavenumber for D/G Raman ratio of the UC01 non-heat-treated sample.

3.2. Thermal transport in Sn thin film

In the present study, a transition zone comprising of a Sn thin film is introduced at the interface between the MWCNTs and the surrounding material (capping layer) to minimize thermal impedance mismatch including thermal resistance due to interfacial roughness. The capping layer, which is generally a metal with high thermal conductivity and low yield strength, aids in filling the surface asperities on both mating solids, thereby reducing the interface thermal resistance between the CNT-polymer composite and the bounding surfaces. Considering diffuse interfaces, even in the regions where the tin layer wets the CNT tips completely (no air gaps), phonons from the CNT tips are expected to be readily transferred to the Sn layer because of the relatively wide phonon spectrum available to the phonons in Sn when compared to the CNTs (phonon spectra in a material is proportional to the density of states, which is proportional to the inverse of the cube of the sound speed in the material). Additionally, the capping layer is kept relatively thin to help minimize its thermal resistance. For this purpose, a thin 500 ± 50 nm layer of tin (46 W/m-K and melting point of 230°C) is expected to serve as an effective capping layer material. As previously mentioned, the top surface of the composite is polished down to ~ 100 nm, as verified by AFM. Therefore, a 500 nm thick tin layer should be sufficient to fill the asperities. The thin layer of tin is deposited on the composite sample using sputtering -- the sample is then placed in a vacuum oven at near melting point of tin so that it forms a weld contact with the exposed CNT tips on the top surface.

Recently, Prasher *et al.* (2009) [44] confirmed that the weld contact formed by Sn-like soft (and compliant) metals tend to increase the thermal conductance by an order of magnitude compared to more common Van der Waal contacts at the interfaces. In a recent study by the

authors,[45] the thermal conductivity of a 500 ± 50 nm tin film was determined to be 46 ± 4 W/m-K at room temperature (see APPENDIX II for more details). The thermal conductivity was found to remain nearly constant in the temperature range of 240 K ó 300 K (Figure 7). This is understood to be due to the specific heat being constant in the temperature range with the Dulong-Petit limit being at 210 K. Moreover, the phonon and electron mean free paths at room temperature are relatively small, 50 nm and < 5 nm, respectively, compared to the boundary dimensions [45]. Therefore, boundary scattering is not expected to play a role in the thermal conductivity of the sample. Furthermore, even though the reduction in thermal conductivity in metals is known to occur at elevated temperatures due to the increased phonon-phonon inelastic scattering, the test temperatures in our present case are not high enough for inelastic phonon-phonon (Umklapp) interactions to occur, and thermal conduction continues to be dominated by the specific heat. The estimated thermal resistance of the Sn thin film over the measured temperature range is nearly constant at 1.09×10^{-8} K-m²/W.

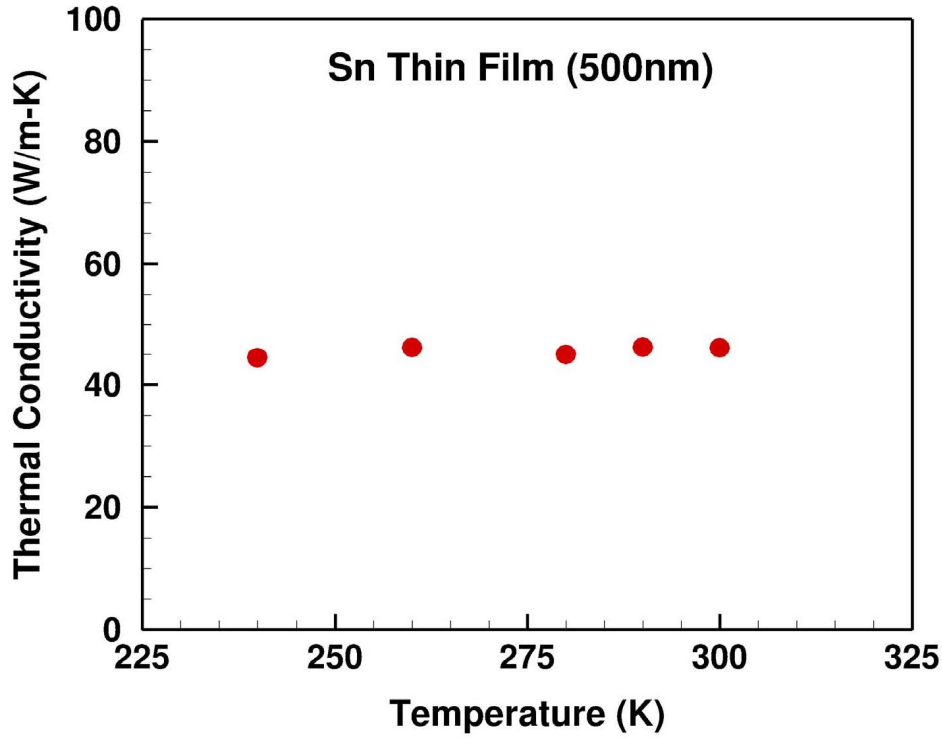


Figure 7: Thermal Conductivity of 500 nm Sn thin film (Replotted from [45], *Kaul and Prakash*, 2011).

3.3. Thermal Transport in Epoxy Polymer

The thermal conductivity of EPON-862 epoxy is measured from 100 K to 340 K (Fig. 8), using the three-omega technique. The measured thermal conductivity of EPON-862 at room temperature is 0.224 ± 0.02 W/m-K. The slight increase in thermal conductivity with temperature is understood to be a result of the increase in specific heat with test temperature. The thermal transport in amorphous polymers (Reese *et al.*) [46], is phonon-dominated with the mean free path of phonons remaining a constant due to scattering by the amorphous disordered regions. For the case of EPON-862, the phonon mean free path is estimated to be 0.32 nm based on the

sound velocity (dilatational wave velocity) of 1949 m/s (corresponding to the elastic modulus value of 2.58 GPa [47] and Poisson's ratio of 0.35) and specific heat equal to 1060 J/Kg-K [48]. The glass transition temperature of EPON-862 is 408 K [47], and the thermal conductivity of Epon-862 is expected to increase continuously until it reaches the transition point. A small jog in the temperature dependence of thermal conductivity is observed at around 225 K, which is consistent with the observation made earlier in many polymers for specific heat dependency with temperature, and can be attributed to the transition of the local amorphous regions within the polymer from glassy to the rubbery state. The rotational and vibrational motions of atomic groups associated with the polymer chains in the rubbery state require a lesser amount of energy for reorganization and mobility when compared to the glassy state.

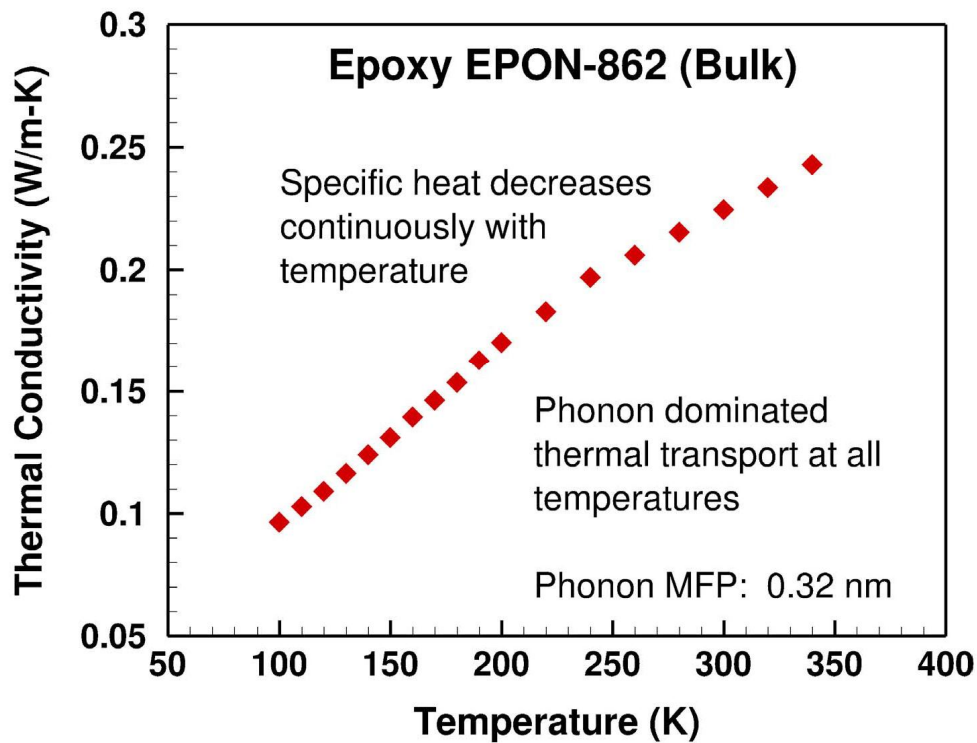


Figure 8: Thermal Conductivity vs Temperature of Epoxy EPON-862 from 100 K-340 K.

3.4. Thermal transport in VA-MWCNTA-Epoxy Composite

In order to characterize the thermal conductivity of the VA MWCNT-epoxy composite the three-omega method outlined in Section 2.3 is employed. A thin layer (~ 500 nm) of tin with a SiO_2 insulating layer on top is deposited on the composite substrate to prevent direct contact with the aluminum heater line and contact pads. The estimation of both thermal conductivity and thermal interface resistance between the layers is important to obtain the through-thickness thermal conductivity of the VA MWCNT-epoxy composite. Tong *et al.* in an earlier work [37] derived a two-layer model based on Feldman's notation. A three-layer 1-D model including the finite interface resistance between layers (based on Feldman's notation) has been derived for this work.

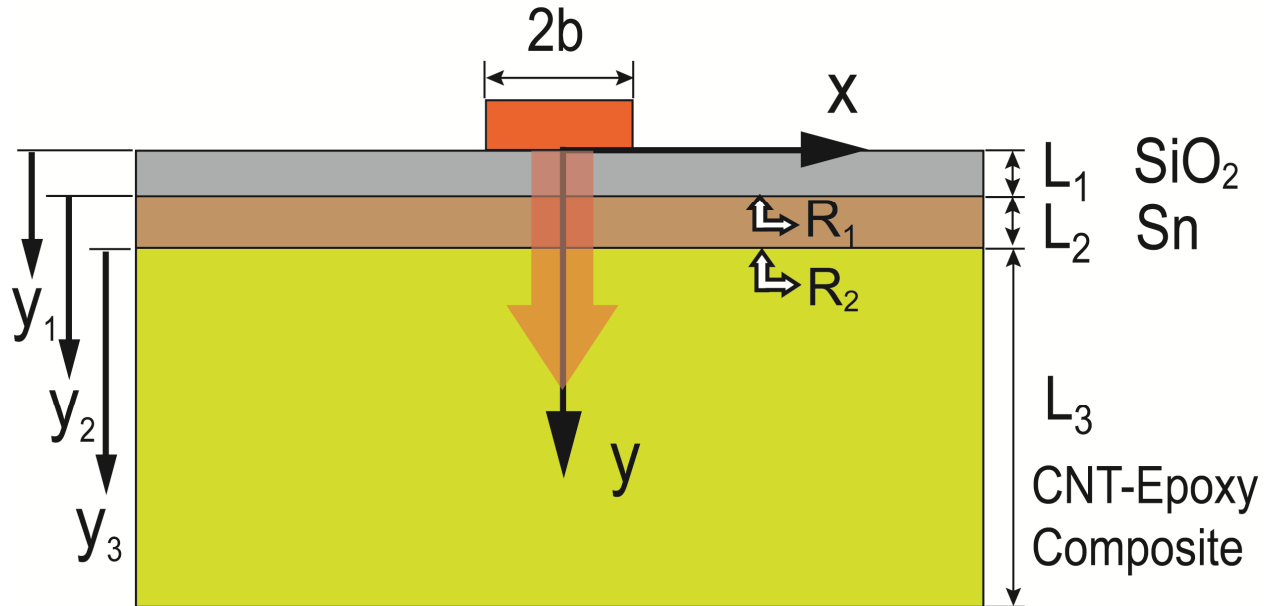


Figure 9: Schematic representation of 1-D thermal transport model for a three-layered structure with a heater on top.

The main steps of the 1D thermal model are provided below. The heat equation for a 1-D multilayer problem can be written as,

$$k_{y,j} \frac{\partial^2 T_j(y,t)}{\partial y^2} = \rho_j C_{p_j} \frac{\partial T_j(y,t)}{\partial t}, \quad (4)$$

where $j=1, 2$ and 3 represent the individual layers (1=SiO₂, 2=Sn, 3=CNT-epoxy composite); T_j is the temperature at a point y_j in an individual layer; and $k_{y,j}$, ρ_j and C_{p_j} represent the thru-thickness thermal conductivity, density, and the specific heat of the individual layers.

Under periodic excitation with angular time frequency, ω , the general solution to Eq. (4) can be expressed as

$$T_j(y_j, t) = A.e^{(\eta_j y_j - i\omega t)} + B.e^{(-\eta_j y_j - i\omega t)} \quad (5)$$

Where $\eta_j = \sqrt{-\frac{i\omega\rho_j C_{p_j}}{k_{y,j}}}$ is the inverse of the penetration depth. The two parts of the solution represent thermal waves propagating to the positive and negative -directions with two complex coefficients, A and B, to be determined by boundary conditions.

Let us assume for this 1D material, a periodic heat flux with amplitude q_o and frequency ω is injected at the surface $y_1 = 0$

$$q(y_1 = 0, t) = q_0 e^{-i\omega t}. \quad (5)$$

Following Feldman's notation,[27] we can express the temperature at any position y as a vector,

$$T_j(y_j, t) = \begin{bmatrix} A.e^{(\eta_j y_j - i\omega t)} \\ B.e^{(-\eta_j y_j - i\omega t)} \end{bmatrix}. \quad (6)$$

The matrix formulation aids in finding the correlation between the temperatures at two different locations within the medium as well as that across the interface between the layers. The boundary condition is based on the assumption that with no heat generated or absorbed at the interfaces, the heat flux is continuous across the interfaces, and there is discontinuity in temperature across a j and $j+1$ interface due to a finite interface thermal resistance $R_{j,j+1}$.

$$\begin{aligned} -k_{y,j} \frac{\partial T_j}{\partial y_j} \Big|_{y_j=L_j} &= -k_{y,j+1} \frac{\partial T_{j+1}}{\partial y_{j+1}} \Big|_{y_{j+1}=0} = R_{j,j+1} [T_{j+1}(y_{j+1}=0) - T_j(y_j=L_j)] \\ \frac{\partial T_1}{\partial y_1} \Big|_{y_1=0} &= 0; \frac{\partial T_3}{\partial y_3} \Big|_{y_3=L_3} = 0 \end{aligned} \quad (7)$$

where L_j is the thickness of the j^{th} layer.

The total thermal impedance Z of the three layered structure neglecting the interface thermal resistance can be obtained as

$$Z = \frac{T_1(0)}{q_o} = \frac{1}{\gamma_1} \left[\frac{\left(1 + \frac{\gamma_3}{\gamma_2} \eta_2 L_2\right) + \left(\frac{\gamma_3}{\gamma_1} + \frac{\gamma_2}{\gamma_1} \eta_2 L_2\right) \eta_1 L_1}{\left(1 + \frac{\gamma_3}{\gamma_2} \eta_2 L_2\right) \eta_1 L_1 + \left(\frac{\gamma_3}{\gamma_1} + \frac{\gamma_2}{\gamma_1} \eta_2 L_2\right)} \right] \quad (8)$$

where $\gamma_j = k_{y,j} \eta_j$ and q_o is the amplitude of the input heat flux. Note that the exponential terms in the solution above have been simplified using Taylor expansion assuming the films are very thin compared to the penetration depth. Since the SiO₂ and Sn films deposited on top of the composite are very thin (in nanometer scale) compared to the penetration depth of heat, i.e. $|\eta_1 L_1| \ll 1$, $|\eta_2 L_2| \ll 1$ and $|\eta_3 L_3| \sim 1$ for the range of frequencies used, makes this approximation valid.

Similarly, the total thermal impedance Z for the three-layered structure with interface resistances $R_1 = R_{1,2}$ (between SiO₂ and Sn) and $R_2 = R_{2,3}$ (between Sn and MWCNT), can be expressed as

$$Z = \frac{1}{\gamma_1} \left[\frac{\left[\left(1 + \gamma_3 R_1 + \gamma_3 R_2\right) + \left(\gamma_2 R_1 + \frac{\gamma_3}{\gamma_2} + \gamma_2 \gamma_3 R_1 R_2\right) \eta_2 L_2 \right] + \left[\frac{\gamma_3}{\gamma_1} + \left(\frac{\gamma_2}{\gamma_1} + \frac{\gamma_2 \gamma_3}{\gamma_1} R_2\right) \eta_2 L_2 \right] \eta_1 L_1}{\left[\left(1 + \gamma_3 R_1 + \gamma_3 R_2\right) + \left(\gamma_2 R_1 + \frac{\gamma_3}{\gamma_2} + \gamma_2 \gamma_3 R_1 R_2\right) \eta_2 L_2 \right] \eta_1 L_1 + \left[\frac{\gamma_3}{\gamma_1} + \left(\frac{\gamma_2}{\gamma_1} + \frac{\gamma_2 \gamma_3}{\gamma_1} R_2\right) \eta_2 L_2 \right]} \right] \quad (9)$$

The model is verified by comparing them with the results obtained for the two layer model as described by Tong *et al.* (2006) [37]. Moreover, using the condition, $\gamma_3 = 0$ in the

absence of a third layer, and $|\eta_2 L_2| \sim 1$ such that, the heat wave dies down within the second layer that now acts as a substrate. By substituting these conditions in the Equation (10), we get the same result as in Tong *et al.* (2006), i.e.

$$Z = \frac{1}{\gamma_2} + R_1 + \frac{L_1}{k_1} \left[1 - \frac{\gamma_1^2}{\gamma_2^2} - \frac{2\gamma_1^2}{\gamma_2} R_1 - \gamma_1^2 R_1^2 \right] \quad (10)$$

Table 1. Model Parameters that fit the experimental amplitude and phase of temperature oscillations

Sample	Thickness	Thermal Diffusivity (m ² /s)	Thermal Conductivity (W/m-K)	Interface Thermal Resistance (m ² K/W)
SiO ₂ Thin Film	350 nm	8.1x10 ⁻⁷	1.2	
Tin Thin Film	500 nm	3.5x10 ⁻⁵	46	
Epoxy (EPON-862)	3 mm	1.76x10 ⁻⁷	0.224	
VA-MWCNT-Epoxy Composite	2.1 mm		5.8	
Interface Resistance oxide-tin, R ₁				5x10 ⁻⁵
Interface Resistance tin-MWCNT array, R ₂				8x10 ⁻⁶ to 8.5x10 ⁻⁷

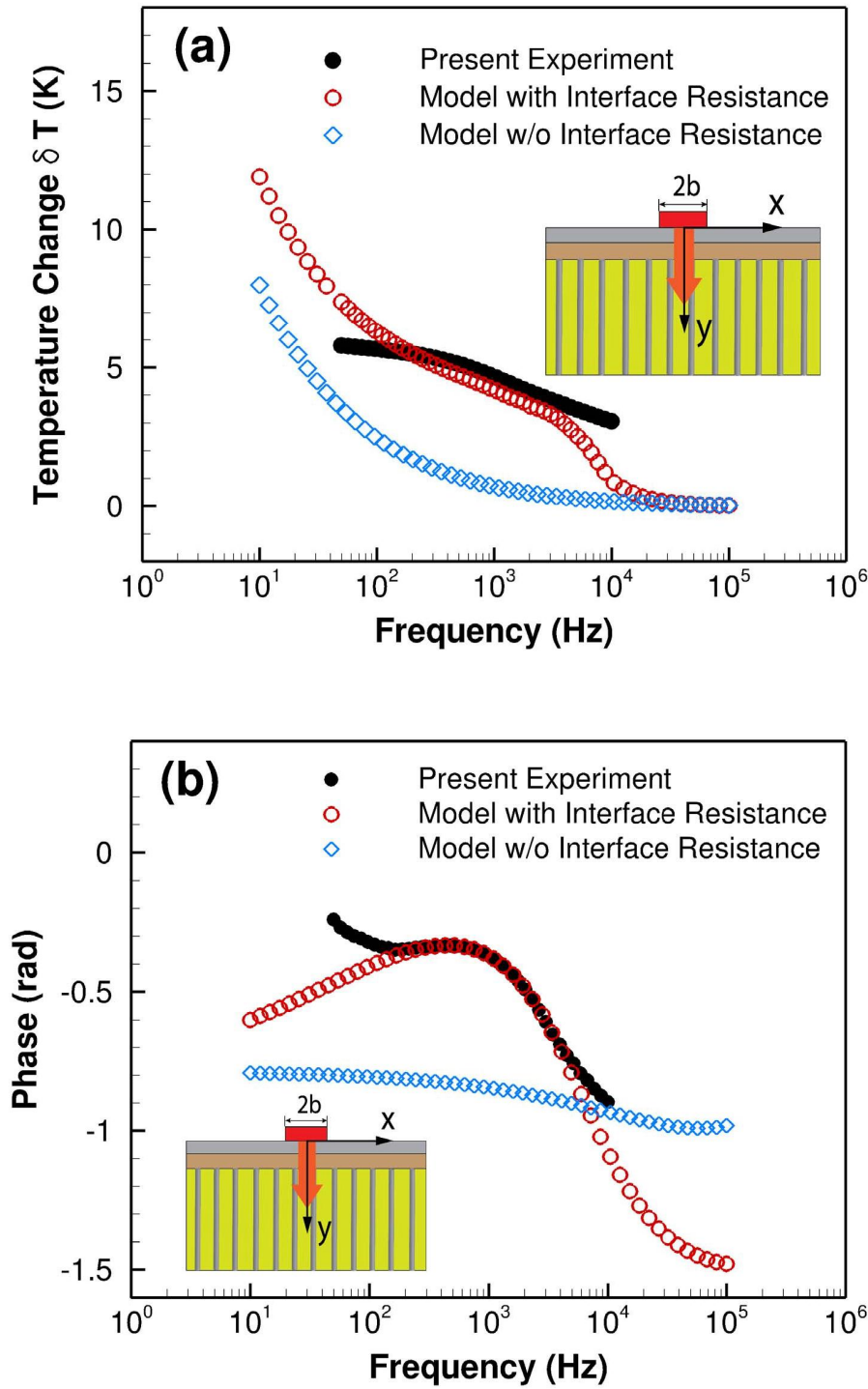


Figure 10: Comparison of Thermal Model with and without interface resistances with experimental data: (a) Temperature oscillations vs frequency; (b) Phase of oscillations vs frequency.

The experimental data on temperature oscillations and phase are compared with the predictions of the thermal model with and without thermal interface resistance between the layers. The thermal model is based on several parameters (shown in *Table 1*), *e.g.*, thermal properties of the various layers, and the unknown thermal interface resistances. An iterative algorithm, as described in Tong *et al.* (2007), [25] was employed to obtain the best fit values for the unknowns. The comparison of the experimental results and model predictions based on the best fit values for the unknown parameters is shown in Fig 10. From these comparisons the thermal conductivity of the CNT-Epoxy composite is estimated to be 5.8 ± 0.64 W/m-K at room temperature. The measured amplitude as well as the phase of the temperature oscillations are found to be sensitive to the thermal conductivities of tin, MWCNT-epoxy composite, and the thermal interface resistances. A $\pm 20\%$ uncertainty in thermal conductivity of either tin or the MWCNT-epoxy composite, results in a corresponding $\pm 5\text{-}10\%$ shift in the amplitude of the temperature oscillations from the measured values. The thermal conductivity of the composite exhibits a slight increase with temperature between 240 K and 300 K (Fig. 11), and is understood to be dominated by the specific heat dependence with temperature of the Epon-862 epoxy [9, 49].

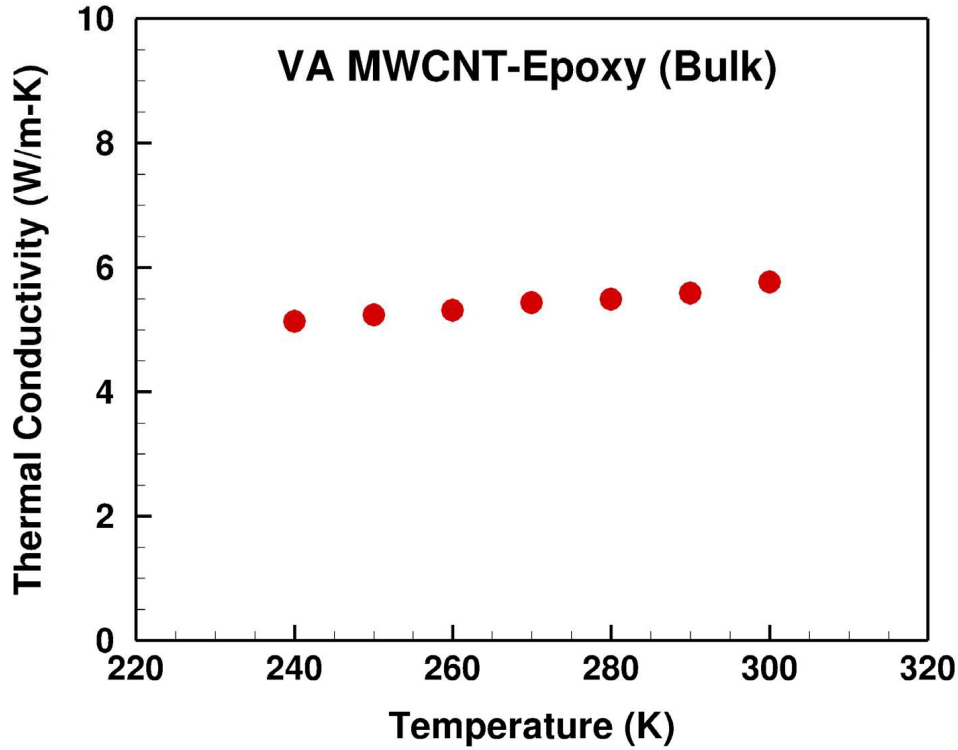


Figure 11: Thermal Conductivity Vs Temperature of VA-MWCNTA-Epoxy (EPON-862) Nanocomposite from 240K-300K.

The best fit estimates for the interface thermal resistances R_{1-2} (between SiO_2 and Sn) and R_{2-3} (between Sn and MWCNT) are $5 \times 10^{-5} \text{ m}^2\text{-K/W}$ and $8 \times 10^{-6} \text{ to } 8.5 \times 10^{-7} \text{ m}^2\text{-K/W}$, respectively. The amplitude or phase of temperature oscillations is especially sensitive to the thermal resistance of the rougher interface (i.e., the SiO_2 & Sn interface) in our case. However, it is relatively less sensitive to the interface thermal resistance of the relatively smooth Sn-MWCNT interface, and therefore by keeping all other parameters constant we can estimate the interface resistance of the smooth Sn-MWCNT interface to within an order of magnitude range. The interface resistance between the layers is a combination of Kapitza resistance based on diffuse mismatch model (DMM) and constriction resistance at the contacts of carbon nanotubes

with the Sn layer. Recently, Prasher *et al.* (2005, 2008) [50, 51], suggested that for nano-sized constrictions (which the vertically aligned MWCNTs make with the layer above it), the effects of mismatch in acoustic properties are more dominant than due to constriction of the heat flux lines. Therefore, vibrational spectra mismatch between Sn, a soft metal with relatively low sound speed, and VA MWCNTs is expected to restrict the thermal conductance through the MWCNT composite when bounded by surfaces on both sides. The Debye temperature of Sn is 170 K, while the Debye temperature for multi-walled carbon nanotubes is much higher, 960 K-2500 K, indicating a large mismatch in vibrational spectra of the two materials. Interface thermal resistance between two highly dissimilar materials with large differences in phonon spectra, e.g., interfaces involving metal and dielectric solids, as pointed out by Lyo and Cahill (2006) [52] is not only due to the coupling of electrons in a metal and phonons in a dielectric substrate, but also by anharmonic processes, namely three-phonon processes that can contribute a significant additional channel for the transport of heat by altering phonon frequency by inelastic scattering processes. For these reasons, carbon nanotubes may be particularly attractive for exchange of thermal energy with Sn across the CNT-Sn interfaces involving both phonons and electrons.

Interestingly, even after a spate of research on VA MWCNT composites, there are only few published works in the literature that reported thermal conductivities greater than 1 W/m-K (Figure 12). Sihn *et al.* (2008)[26] have reported the highest thermal conductivity so far for a 30 μ m VA MWCNT-epoxy composite. Using a simple 1-D thermal resistance network model to estimate the thermal conductivity of their MWCNT composite from their reported data, we estimate the room temperature thermal conductivity of their VA MWCNT-epoxy composite to be

137 W/m-K. Considering a 10 vol. % of MWCNTs in their composite, the thermal conductivity of individual MWCNTs is in excess of 1000 W/m-K.

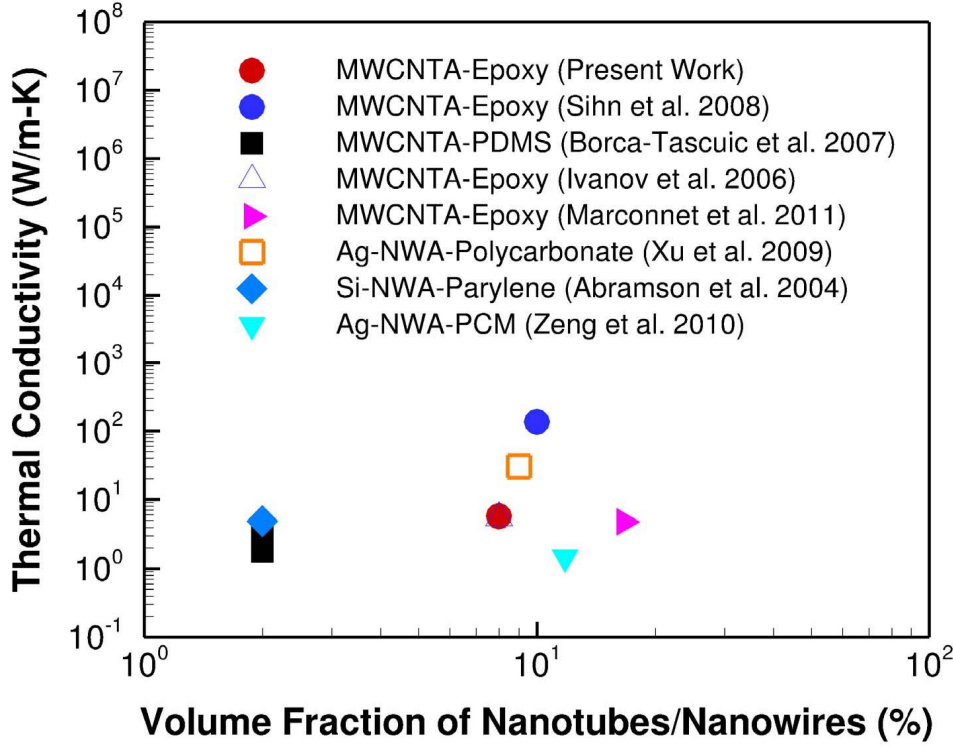


Figure 12: Thermal Conductivity vs Volume Fraction of Nanowires and Nanotubes.

The primary reasons for a less than 1 W/m-K thermal conductivity of the MWCNT composites reported in the literature may be due to the low volume fraction of CNTs used in the composites as well as their defect state and purity. Additionally, in order to improve their performance as TIM material, thermal conductance at CNT-capping layer interfaces need to be addressed. However, results of the present study suggest that the thermal interface resistance for relatively smooth and polished surfaces may contribute to only second order effects in the

thermal performance of the TIMs at room temperature. In a parallel study [40], the authors investigated thermal conductivity in annealed and as received thermal CVD grown individual multiwalled carbon nanotubes. They reported a five-fold increase in thermal conductivity of the MWCNTs from the annealed batch. Moreover, it was also noted that depending on the degree of inherent physical deformities/defects in the CNTs, thermal conductivity of even the annealed samples could be lower than those obtained for the as received batch (Figure 13). High resolution SEM micrographs of CNT arrays (Figure 14) from the same batch as the array that was used in the fabrication of the composite indicate physical deformities and defects, including entanglement of carbon nanotubes and fused contacts, that are understood to be the reason for reduced thermal conductivity of the composites in general. It is to be noted that most previous works reported in the literature on VA MWCNT-polymer composites [15, 17, 26, 53] show room-temperature thermal conductivity as high as metal nanowire array-polymer composites [54, 55] or the semiconductor nanowire array-polymer composites [56, 57] with nanowire volume fractions in the same range as the carbon nanotubes. Nevertheless, the five-fold increase in thermal conductivity in the post-annealed MWCNTs suggests that the thermal conductivity of VA MWCNT-epoxy composites can be designed to be as high as 25 W/m-K, which can potentially have a major impact in the design of multifunctional, load-bearing, high-thermal performance structural interfaces for a variety of thermal management applications.

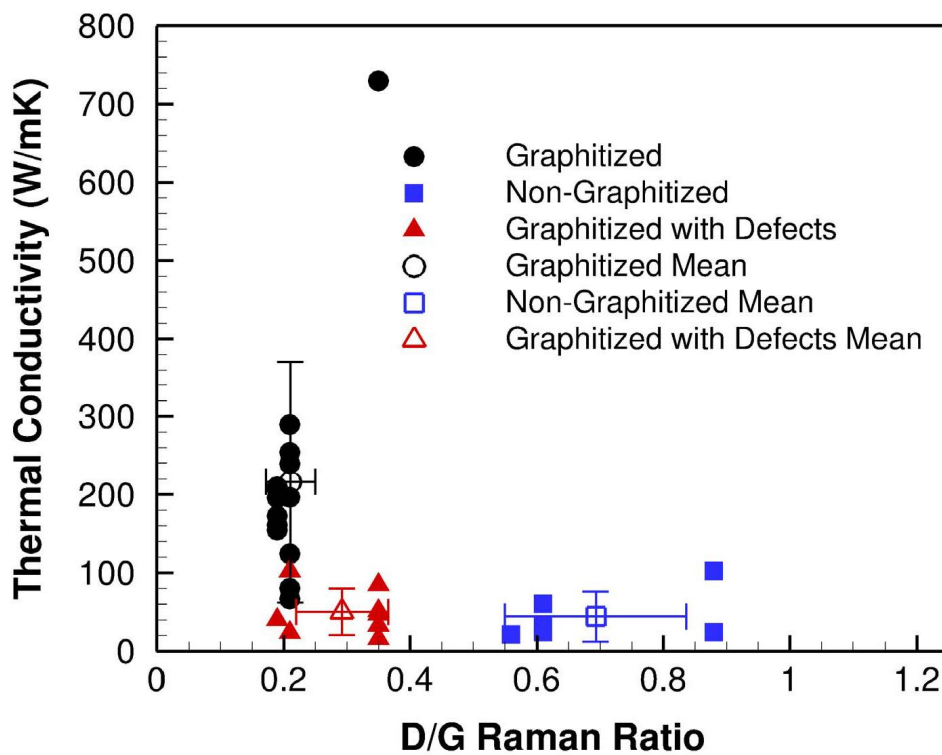


Figure 13: Thermal Conductivity vs Raman Ratio of individual multi-walled nanotubes. [Replotted from Ref [40], Bifano, Kaul and Prakash, 2011]

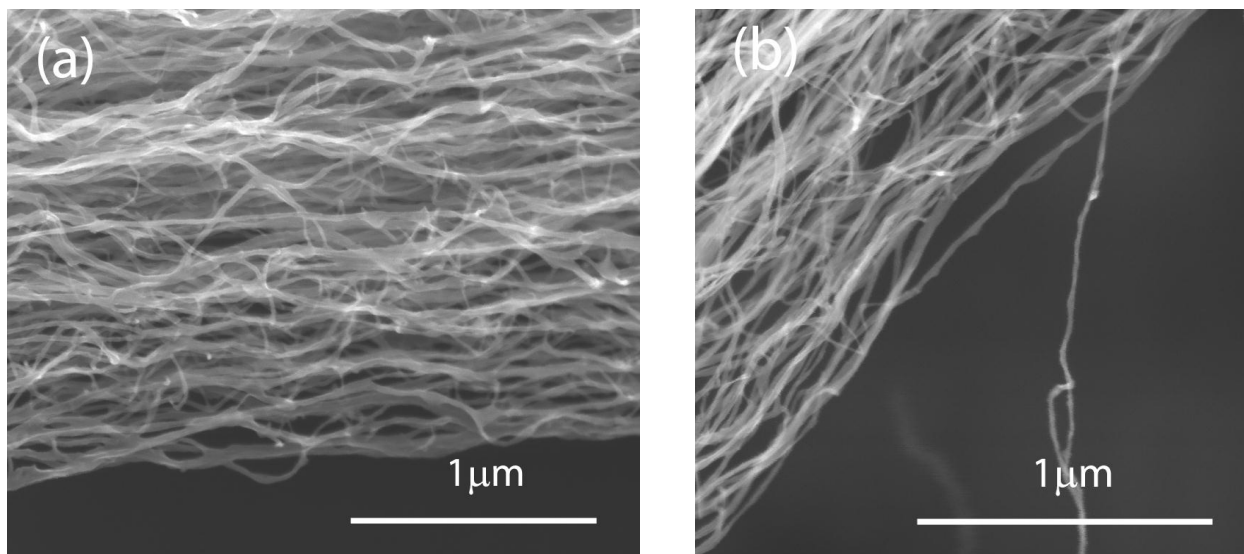


Figure 14: SEM micrographs (9 kV, 3.5 mm working distance, and spot size, 2.5) of MWCNT array batch of which the composite was made and tested: (a) Entanglements of Individual Nanotubes (87,000X) and (b) Individual samples are often attached as if they are fused together (100,000X).

SUMMARY

This paper reports development of vertically aligned multi-wall carbon nanotube (VA-MWCNT) array composites for thermal energy management in load-bearing structural applications. Unlike previous studies on the characterization of VA-MWCNT-based thermal interface materials (TIMs) for primarily non-load bearing applications, the material systems of interest here involve the use of VA MWCNTs in an epoxy matrix. The epoxy matrix imparts mechanical strength to these systems while the VACNTs provide avenues for high thru-thickness thermal conductivity across a typical material interface. In order to obtain the thermal characteristics of these multifunctional TIMs, we report measurements of thermal conductivity in the Sn-capped VA-MWCNT-epoxy composites as well as in its individual constituents, i.e., bulk EPON-862 (matrix material) and Sn thin film, in the temperature range 240 K \leq 300 K, and individual multi-wall carbon nanotubes at room temperature taken from the same VA-MWCNT batch as the one used to fabricate the CNT-epoxy TIM. The thermal conductivity of the epoxy and Sn thin film was obtained as a function of temperature by using a cryostat in conjunction with the three omega method. The thermal conductivity of individual free standing MWCNT samples was obtained by employing the Wollaston T-type three-omega probe method inside a high resolution scanning electron microscope equipped with nanomanipulators and a gas injection system for electron beam induced platinum deposition. The thermal conductivity of bulk EPON-862 epoxy was observed to increase gradually from 0.1 W/m-K at 100 K, to 0.24 W/m-K at 340 K, and is understood to be dominated by the heat capacity of the epoxy. The thermal conductivity of Sn capping layer (500 micron film thickness) was observed to remain nearly constant at about 46 W/m-K over the above mentioned temperature range. The thermal conductivity of individual freestanding carbon nanotubes was measured to be about 60 W/m-K at

room temperature. A 1-D multilayer thermal model that includes effects of thermal interface resistance and the thermal conductivity of the CNT-epoxy composite and its constituents was used to interpret the experimental results. The thermal conductivity of the carbon nanotube-epoxy composite was estimated to be about 5.8 W/m-K and exhibits a slight increase with temperature in the range of 240 K to 300K. The best fit estimates for the interface thermal resistances between SiO₂ and Sn and between Sn and MWCNT were $5 \times 10^{-5} \text{ m}^2\text{-K/W}$ and $8 \times 10^{-6} \text{ to } 8.5 \times 10^{-7} \text{ m}^2\text{-K/W}$, respectively. The results of this study suggests that the inclusion of a Sn thin layer on the VA-MWCNT array, as well as the morphological structure of the individual MWCNTs are dominating factors that control the overall thermal conductivity of the TIM. These results are encouraging in light of the fact that the thermal conductivity of a VA-MWCNT array can be increased by an order of magnitude by using a standard high-temperature post-annealing step. In this way, multifunctional (load bearing) TIMs with effective through thickness thermal conductivities as high as 25 W/m-K, can be potentially fabricated.

REFERENCES

1. Greenwood JA, Williamson JBP.(1966) Contact of Nominally Flat Surfaces. Proceedings of the Royal Society of London Series A Mathematical and Physical Sciences. December 6, 1966;295(1442):300-19.
2. Prasher R.(2006) Thermal Interface Materials: Historical Perspective, Status, and Future Directions. Proceedings of the IEEE.94(8):1571-86.
3. Berber S, Kwon Y-K, Tománek D.(2000) Unusually High Thermal Conductivity of Carbon Nanotubes. Physical Review Letters.84(20):4613.
4. Hone J, Whitney M, Piskoti C, Zettl A.(1999) Thermal conductivity of single-walled carbon nanotubes. Physical Review B.59(4):R2514.
5. Hone J.(2000) Electrical and thermal transport properties of magnetically aligned single wall carbon nanotube films. Appl Phys Lett. [10.1063/1.127079].77(5):666.

6. Kim P, Shi L, Majumdar A, McEuen PL.(2001) Thermal Transport Measurements of Individual Multiwalled Nanotubes. *Physical Review Letters*.87(21):215502.
7. Baughman RH.(2002) Carbon Nanotubes--the Route Toward Applications. *Science*.297(5582):787-92.
8. Hone J, Llaguno MC, Biercuk MJ, Johnson AT, Batlogg B, Benes Z, et al.(2002) Thermal properties of carbon nanotubes and nanotube-based materials. *Applied Physics A: Materials Science & Processing*.74(3):339-43.
9. Shi L, Li D, Yu C, Jang W, Kim D, Yao Z, et al.(2003) Measuring Thermal and Thermoelectric Properties of One-Dimensional Nanostructures Using a Microfabricated Device. *Journal of Heat Transfer*.125(5):881-8.
10. Yu C, Shi L, Yao Z, Li D, Majumdar A.(2005) Thermal Conductance and Thermopower of an Individual Single-Wall Carbon Nanotube. *Nano Letters*.5(9):1842-6.
11. Pop E, Mann D, Wang Q, Goodson K, Dai H.(2005) Thermal Conductance of an Individual Single-Wall Carbon Nanotube above Room Temperature. *Nano Letters*.6(1):96-100.
12. Choi SUS, Zhang ZG, Yu W, Lockwood FE, Grulke EA.(2001) Anomalous thermal conductivity enhancement in nanotube suspensions. *Applied Physics Letters*.79(14):2252.
13. Biercuk MJ, Llaguno MC, Radosavljevic M, Hyun JK, Johnson AT, Fischer JE.(2002) Carbon nanotube composites for thermal management. *Applied Physics Letters*.80(15):2767.
14. Choi ES, Brooks JS, Eaton DL, Al-Haik MS, Hussaini MY, Garmestani H, et al.(2003) Enhancement of thermal and electrical properties of carbon nanotube polymer composites by magnetic field processing. *Journal of Applied Physics*.94(9):6034.
15. Ivanov I, Puretzky A, Eres G, Wang H, Pan Z, Cui H, et al.(2006) Fast and highly anisotropic thermal transport through vertically aligned carbon nanotube arrays. *Applied Physics Letters*.89(22):223110.
16. Borca-Tasciuc T.(2005) Anisotropic thermal diffusivity of aligned multiwall carbon nanotube arrays. *J Appl Phys*. [10.1063/1.2034079].98(5):054309.
17. Borca-Tasciuc T, Mazumder M, Son Y, Pal SK, Schadler LS, Ajayan PM.(2007) Anisotropic Thermal Diffusivity Characterization of Aligned Carbon Nanotube-Polymer Composites. *Journal of Nanoscience and Nanotechnology*.7(4-5):1581-8.

18. Xuejiao H, Linan J, Goodson KE, editors. Thermal conductance enhancement of particle-filled thermal interface materials using carbon nanotube inclusions. Thermal and Thermomechanical Phenomena in Electronic Systems, 2004 ITherm '04 The Ninth Intersociety Conference on; 2004 1-4 June 2004.
19. Tong T, Zhao Y, Delzeit L, Kashani A, Majumdar A.(2004) Multiwalled Carbon Nanotube/Nanofiber Arrays as Conductive and Dry Adhesive Interface Materials. ASME Conference Proceedings.2004(41774):7-12.
20. Hu XJ, Panzer MA, Goodson KE.(2007) Infrared Microscopy Thermal Characterization of Opposing Carbon Nanotube Arrays. Journal of Heat Transfer.129(1):91.
21. Xu J, Fisher T.(2006) Enhancement of thermal interface materials with carbon nanotube arrays. International Journal of Heat and Mass Transfer.49(9-10):1658-66.
22. Cola BA, Xu J, Cheng C, Xu X, Fisher TS, Hu H.(2007) Photoacoustic characterization of carbon nanotube array thermal interfaces. Journal of Applied Physics.101(5):054313.
23. Cola BA, Xu X, Fisher TS.(2007) Increased real contact in thermal interfaces: A carbon nanotube/foil material. Applied Physics Letters.90(9):093513.
24. Shaikh S, Li L, Lafdi K, Huie J.(2007) Thermal conductivity of an aligned carbon nanotube array. Carbon.45(13):2608-13.
25. Tao T, Yang Z, Delzeit L, Kashani A, Meyyappan M, Majumdar A.(2007) Dense Vertically Aligned Multiwalled Carbon Nanotube Arrays as Thermal Interface Materials. Components and Packaging Technologies, IEEE Transactions on.30(1):92-100.
26. Sihn S, Ganguli S, Roy AK, Qu L, Dai L.(2008) Enhancement of through-thickness thermal conductivity in adhesively bonded joints using aligned carbon nanotubes. Composites Science and Technology.68(3-4):658-65.
27. Feldman A.(1999) Algorithm for solutions of the thermal diffusion equation in a stratified medium with a modulated heating source. High Temperatures - High Pressures. [Journal].31(3):293-8.
28. Yang YY, Huang SM, He HZ, Mau AWH, Dai LM.(1999) Patterned Growth of Well-Aligned Carbon Nanotubes: a Photolithographic Approach. Journal of the American Chemical Society.121(46):10832-3.
29. Chen W, Qu L, Chang D, Dai L, Ganguli S, Roy A.(2008) Vertically-aligned carbon nanotubes infiltrated with temperature-responsive polymers: Smart nanocomposite films for self-cleaning and controlled release. Chemical Communications.163-5.

30. Hata K, Futaba D, Mizuno K, Namai T, Yumura M, Iijima S.(2004) Water-assisted highly efficient synthesis of impurity-free single-walled carbon nanotubes. *Science*.306:1362-4.
31. Shanov V, Yun Y-H, Schulz MJ.(2006) Synthesis and characterization of carbon nanotube materials. *Journal of the U of Chem Tech and Metall*.41(4):377-90.
32. Yun Y-H, Shanov V, Tu Y, Subramaniam S, Schulz MJ.(2006) Growth mechanism of long aligned multi-wall carbon nanotube arrays by water-assisted chemical vapor deposition. *Journal of Phys Chem B*.110:23920-5.
33. Cahill DG.(1990) Thermal conductivity measurement from 30 to 750 K: the 3 omega method. *Review of Scientific Instruments*.61(2):802-8.
34. Lee SM, Cahill DG.(1997) Heat transport in thin dielectric films. *Journal of Applied Physics*.81(6):2590-5.
35. Borca-Tasciuc T.(2001) Data reduction in 3-omega method for thin-film thermal conductivity determination. *Rev Sci Instrum*. [10.1063/1.1353189].72(4):2139.
36. Olson BW.(2005) A practical extension of the 3-omega method to multilayer structures. *Rev Sci Instrum*. [10.1063/1.1896619].76(5):053901.
37. Tong T.(2006) Reexamining the 3-omega technique for thin film thermal characterization. *Rev Sci Instrum*. [10.1063/1.2349601].77(10):104902.
38. Kim J.(1999) Application of the three omega thermal conductivity measurement method to a film on a substrate of finite thickness. *J Appl Phys*. [10.1063/1.371314].86(7):3959.
39. Cahill DG, Pohl RO.(1987) Thermal conductivity of amorphous solids above the plateau. *Physical Review B*.35(8):4067.
40. Bifano MFP, Kaul, P. B., Prakash, V.(2011) Thermal Conductivity Measurements of Heat Treated and Non-Heat Treated Individual MWCNT Using a Wollaston T-Type Probe Method. *Journal of Applied Physics*. [Journal].Submitted.
41. DiLeo RA, Landi BJ, Raffaele RP.(2007) Purity assessment of multiwalled carbon nanotubes by Raman spectroscopy. *Journal of Applied Physics*.101(6):064307-5.
42. Dresselhaus MS, Jorio A, Hofmann M, Dresselhaus G, Saito R.(2010) Perspectives on Carbon Nanotubes and Graphene Raman Spectroscopy. *Nano Letters*.10(3):751-8.
43. Andrews R, Jacques D, Qian D, Dickey EC.(2001) Purification and structural annealing of multiwalled carbon nanotubes at graphitization temperatures. *Carbon*.39(11):1681-7.

44. Prasher R.(2009) Acoustic mismatch model for thermal contact resistance of van der Waals contacts. *Applied Physics Letters*.94(4):041905.
45. Kaul PB, Prakash, V.(2011) Grain-boundary and Twin-boundary Scattering Dependent Thermal Conduction in Nanoscale Tin Films. *Nano Letters*. [Journal Article].To be Submitted.
46. Reese W.(1966) Temperature Dependence of the Thermal Conductivity of Amorphous Polymers: Polymethyl Methacrylate. *J Appl Phys*. [10.1063/1.1703187].37(8):3227.
47. Rangari VK, Bhuyan MS, Jeelani S.(2011) Microwave curing of CNFs/EPON-862 nanocomposites and their thermal and mechanical properties. *Composites Part A: Applied Science and Manufacturing*.42(7):849-58.
48. Ganguli S, Roy AK, Anderson DP.(2008) Improved thermal conductivity for chemically functionalized exfoliated graphite/epoxy composites. *Carbon*.46(5):806-17.
49. Pradhan NR, Duan H, Liang J, Iannacchione GS.(2009) The specific heat and effective thermal conductivity of composites containing single-wall and multi-wall carbon nanotubes. *Nanotechnology*.20(24):245705-.
50. Prasher R.(2005) Predicting the Thermal Resistance of Nanosized Constrictions. *Nano Letters*.5(11):2155-9.
51. Prasher R.(2008) Thermal boundary resistance and thermal conductivity of multiwalled carbon nanotubes. *Physical Review B*.77(7):075424.
52. Lyeo H-K, Cahill DG.(2006) Thermal conductance of interfaces between highly dissimilar materials. *Physical Review B*.73(14):144301.
53. Marconnet AM, Yamamoto N, Panzer MA, Wardle BL, Goodson KE.(2011) Thermal Conduction in Aligned Carbon NanotubeóPolymer Nanocomposites with High Packing Density. *ACS Nano*.5(6):4818-25.
54. Xu J.(2009) Silver nanowire array-polymer composite as thermal interface material. *J Appl Phys*. [10.1063/1.3271149].106(12):124310.
55. Zeng J, Cao Z, Yang D, Sun L, Zhang L.(2010) Thermal conductivity enhancement of Ag nanowires on an organic phase change material. *Journal of Thermal Analysis and Calorimetry*.101(1):385-9.

56. Abramson AR, Woo Chul K, Huxtable ST, Haoquan Y, Yiyang W, Majumdar A, et al.(2004) Fabrication and characterization of a nanowire/polymer-based nanocomposite for a prototype thermoelectric device. *Microelectromechanical Systems, Journal of*.13(3):505-13.
57. Biswas KG.(2009) Thermal conductivity of bismuth telluride nanowire array-epoxy composite. *Appl Phys Lett*. [10.1063/1.3143221].94(22):223116.

APPENDIX I

Effect of Heat Treatment on Thermal Conductivity of Multi-walled Carbon Nanotube

ABSTRACT

Thermal conductivity measurements in commercially available chemical vapor deposition (CVD) grown heat-treated and non-heat treated multiwalled carbon nanotubes (MWCNTs) are reported. The thermal conductivity of individual samples is measured using a suspended platinum (Pt) wire as a thermal resistance probe in a “T-type” configuration. Changes in third harmonic voltage are measured across the heated suspended platinum wire as a specimen is attached to the Pt wire’s mid-point. An analytic model is used to correlate the reduction in the average temperature of the probe wire to the thermal resistance (and thermal conductivity) of the attached sample. Experiments are implemented inside a scanning electron microscope equipped with nanomanipulators and electron beam platinum deposition to improve thermal contact resistances. The results indicate a nearly 5 fold increase in the average thermal conductivity of MWCNT samples annealed with a 20 hour 3000°C annealing heat treatment compared to the as-grown samples. However, specimen specific morphological defects are found to negate, to a large degree, the advantage of the heat treatment process. The average thermal conductivity of the heat-treated MWCNT specimens was measured to be 216 W/m-K, with the highest measured thermal conductivity being 730 ± 153 W/m-K. The results highlight the importance of sample quality of MWCNTs for use in thermal management applications.

1. INTRODUCTION

There is little agreement amongst the few reported thermal conductivity measurements [1-5] in MWCNTs. This likely due to the vast structural and chemical differences between the samples measured. Room temperature thermal conductivity measurements in MWCNTs have been reported to be as high as 3000 W/m-K [1] and as low as 17 W/m-K [5]. The chemical vapor deposition (CVD) process commonly used in the synthesis of SWCNT and MWCNTs is known to produce a variety of CNT qualities depending on growth temperature, catalyst and carbon source gasses used [6].

A 2001 study [7] showed many structural and chemical improvements in CVD grown MWCNTs with high temperature annealing. Annealing temperatures that exceeded 2250°C were found to produce x-ray diffraction patterns similar to those of highly graphitic MWCNTs grown by arc-discharge methods. Smaller interlayer wall spacing, indicative of highly graphitic structure, were also possible with higher annealing temperatures up to 3000°C. Residual Fe, the primary chemical vapor deposition growth catalyst for MWCNTs, was also found to reduce from 7.1 % by wt. after CVD growth to less than 0.01 %. Major Fe reduction occurred both at the ends and in the core of the MWCNTs once the annealing temperature surpassed the vaporization temperature of Fe (>1800°C). While heat treatment improved the microstructural quality of the samples, larger defects that created bends and branching in the tubes were not removed in the heat-treatment process. More continuous crystalline planes and a reduction in residual catalyst particles are expected to increase phonon mean free path (MFP), and thus increase the lattice (phonon) thermal conductivity in MWCNTs.

More recently, Jin *et al.* [8] reported that annealing of macroscopic MWCNT bundles at 2800°C for 4 hours resulted in a 9 fold increase in thermal conductivity at 300 K (~2.5 to 23 W/m-K). However, from these measurements an improvement in intrinsic thermal conductivity of individual MWCNT could not be unambiguously ascertained due to the possibly dominating effects of thermally resistive junctions between tubes, which may have also been affected by the heat-treatment process. To the best of the authors' knowledge, heat-treatment effects on the thermal conductivity of individual MWCNTs have not been characterized.

Over the past 50 years, thermal properties of electrically conductive samples and their surroundings have been investigated by measuring the 3rd harmonic voltage signal produced when the sample experiences joule heating via an electric alternating current [9-11]. Comparison of the measured 3rd harmonic voltage across the sample with an analytic model permits the thermal properties of the sample to be determined. The most simplistic steady-state thermal conductivity measurement method is the “self-heating” technique [12]. In general, the self-heating method requires samples to be electrically conductive, transport heat diffusively, and the temperature coefficient of resistance of the sample to be known. The self-heating method was first applied to a bundle of CNTs [12], and subsequently to individual MWCNTs [3].

An extension of the self-heating technique is the “T-Type Probe method,” which replaces the sample with a pre-calibrated suspended wire of known electrical resistivity and temperature coefficient of resistance (Fig. 1). In this way, by attaching a free standing specimen to the probe wire and measuring the reduction in average temperature (inferred from the change in voltage) of the suspended probe wire, the thermal resistance, and thus, thermal conductivity of the specimen

is determined. To date, the T-type method has been used to measure a variety of microscale samples [13, 14]. In 2005 Fujii *et al.* [2] developed a micro-fabricated Pt thermal resistance T-type probe that used 3ω voltage detection to measure the thermal conductivity of individual MWNCTs.

In this study, a T-Type probe composed of Wollaston wire is implemented. The use of commercially available Wollaston wire was first introduced in 2007 in both 1ω and 3ω configurations for T-Type CNT thermal conductivity measurements of individual MWCNTs at room temperature [5]. However, only one measurement of 17 W/m-K was reported. The low value of the thermal conductivity was attributed to high thermal contact resistance at the probe-sample interface and/or the possibility of ballistic transport in the rather short length sample (380 nm) tested.

Many experimental techniques to measure thermal conductivity in individual nanoscale samples currently employ a micro-fabricated sensing device [1, 2, 15, 16]. Use of commercially available Wollaston wire has the advantage of being extremely cost effective compared to conventional microfabrication methods, and allows for a large volume of samples to be characterized in a short span of time. In the present investigation, all thermal property characterization studies are conducted inside a high-resolution scanning electron microscope equipped with nanomanipulators and gas injection system for high throughput analysis. Moreover, appropriate choice of materials and package design allows for multiple Wollaston T-Type probes to be prepared with varying thermal resistances, and thus measurement sensitivities.

2. METHODS

2.1. Three Omega Measurements for the T-Type Probe Method

In order to conduct the three omega measurements, the probe wire is heated by a low frequency alternating current $I(t)=I_{l\omega}\sin(\omega t)$, where $I_{l\omega}$ is the current amplitude. The electrical resistance of the probe wire at zero current is R_{eo} . For sufficiently low heating currents $I(t)$, Joule heating is assumed to be of the form,

$$Q(t) = I^2(t)R_{eo} = \frac{1}{2}I_{l\omega}^2 R_{eo} (1 - \cos(2\omega t)) \quad (1)$$

While conducting the experiments, attention must be paid to maintain the validity of Eq. (1). The temperature rise of the probe wire must be limited to only a few degrees above ambient temperature. If care is not taken, the average heat input would be better modeled using an iterative $Q(t) = I^2(t)R(t)$ instead of $Q(t) = I^2(t)R_{eo}$, resulting in a non-linear dependence of the change in probe wire electrical resistance to Joule heating. The non-linearity is carefully monitored through comparison of linear and quadratic regression models.

The spatially averaged temperature response of the wire $\bar{\theta}(t)$ is proportional to the joule heating by a thermal transfer function Z_o as,

$$\bar{\theta}(t) = Z_o Q(t) \quad (2)$$

As long as the heating current is driven at a sufficiently low frequency the thermal response of the probe wire remains in phase with the heating current and the thermal transfer function is largely frequency independent (See Appendix I). Since Z_o is a function of the thermal resistance of the

probe or the probe-sample combination, experimental determination of Z_o allows the sample's thermal resistance and thus thermal conductivity to be obtained.

Using Eq. (2) along with the electrical resistance response of the probe wire, $R_e(t) = R_{eo}[1 + \alpha \bar{\theta}(t)]$, where α is the temperature coefficient of resistance, the electrical resistance of the probe wire $R_e(t)$ will experience oscillations at 2ω given by

$$R_e(t) = R_{eo} + \frac{1}{2}\alpha Z_o I_{1\omega}^2 R_{eo}^2 - \frac{1}{2}\alpha Z_o I_{1\omega}^2 R_{eo}^2 \cos(2\omega t) . \quad (3)$$

Using Ohm's law along with Eq. (3), the voltage across the probe wire can be written as

$$\begin{aligned} V(t) &= I(t)R_e(t) \\ &= \left[I_o R_{eo} + \frac{3}{4}\alpha Z_o R_{eo}^2 I_{1\omega}^3 \right] \sin \omega t - \left[\frac{1}{4}\alpha Z_o I_{1\omega}^3 R_{eo}^2 \right] \sin 3\omega t . \end{aligned} \quad (4)$$

Equation 4 shows that the measured voltage is the combination of the 1ω and 3ω frequency harmonics of the initial heating current. A Lock-in Amplifier is used to selectively measure the RMS voltage corresponding to either component. The reported MWCNT data in this study utilizes the 3ω detection since the constant ohmic signal contained within the 1ω signal is expected to lead to a greater degree of scatter. In terms of the RMS voltage, the voltage at the third frequency harmonic, $V_{3\omega, RMS}$, can be written as

$$V_{3\omega, RMS} = \frac{1}{2} \alpha Z_o I_{1\omega, RMS} R_{eo} Q_{RMS} \quad (5)$$

where $Q_{RMS} \equiv I_{1\omega, RMS}^2 R_{eo}$. Dividing both sides of Eq. (5) by $I_{1\omega, RMS}$, the 3ω RMS electrical resistance, defined as $R_{e3\omega, RMS} \equiv V_{3\omega, RMS}/I_{1\omega, RMS}$, is written as,

$$R_{e3\omega, RMS} = \frac{1}{2} \alpha R_{eo} Z_o Q_{RMS} \quad (6)$$

Next, the thermal transfer function Z_o is experimentally determined by obtaining the slope of the $R_{e3\omega, RMS}$ vs. Q_{RMS} plot. Since Z_o is a function of the sample thermal resistance, $R_{th,S}$, and the probe-wire thermal resistance, $R_{th,P}$, comparing Z_o with model predictions (see Sec. 2.2) for joule heating in the probe wire with and without the sample allows both $R_{th,P}$ and $R_{th,S}$ to be determined.

2.2. Analytical Model for the Thermal Transfer Function Z_o

The steady state thermal response of the probe wire is modeled using

$$k_P \frac{d^2 \theta(x)}{dx^2} = -\frac{Q_{RMS}}{A_P L_P}, \quad (7)$$

where x is the coordinate along the length of the probe wire (Fig. 1), k_P is the thermal conductivity of the probe wire, L_P is the length of the probe wire, and $\theta(x)$ is the spatially dependent temperature rise. Convection and radiation heat losses are neglected by performing the measurement with very small heating amplitudes and under vacuum conditions within the SEM chamber [17].

The thermal resistance of the sample, $R_{th,S}$, is incorporated into the model by a flux boundary condition at the point of sample attachment, i.e.,

$$\frac{\theta(0)}{R_{th,S}} = k_P A_P \left(\left. \frac{\partial \theta(x)}{\partial x} \right|_{x=0^+} - \left. \frac{\partial \theta(x)}{\partial x} \right|_{x=0^-} \right). \quad (8)$$

The boundary conditions at the ends of the probe wire are

$$\theta(+L_P/2) = \theta(-L_P/2) = 0. \quad (9)$$

The piecewise parabolic solution for positive and negative x satisfying Eqs. (7), (8), and (9) is

$$\theta(x, \eta) = \frac{Q_{RMS} L_P}{8k_P S_P} \left[\left(1 - \left(\frac{x}{L/2} \right)^2 \right) + \left(\frac{\eta}{1+\eta} \right) \left(\left| \frac{x}{L/2} \right| - 1 \right) \right], \quad (10)$$

where the parameter η is the ratio of the thermal resistance of the probe wire to the thermal resistance of the sample $R_{th,S}$ and is defined by $\eta \equiv R_{th,P}/4R_{th,S}$ [5]. The thermal resistance of the probe wire and the sample is given by $R_{th,P} = L_P/k_P A_P$ and $R_{th,S} = L_S/k_S A_S$, respectively. In the absence of the sample $R_{th,S} = \infty$, $\eta = 0$, and therefore the well-known inverted parabolic solution for a Joule heated suspended wire is recovered.

Integrating over the length of the probe wire, the spatially averaged temperature rise $\bar{\theta}$ over the length of the sample can be written as

$$\bar{\theta} = \frac{1}{12} Q_{RMS} R_{th,P} \left(1 - \frac{3}{4} (1 + \eta^{-1})^{-1} \right). \quad (11)$$

Comparison of Eq. (11) and (2) reveals the theoretical thermal transfer function to be,

$$Z_o = \frac{1}{12} R_{th,P} \left(1 - \frac{3}{4} (1 + \eta^{-1})^{-1} \right). \quad (12)$$

2.3. Experimental Procedure

Inserting Eq. (12) into Eq. (6) and taking $\eta = 0$ (absence of sample), the thermal resistance of the probe wire is first estimated using

$$R_{th,P} = \frac{24}{\alpha R_{eo}} \left(\frac{\Delta R_{e3\omega,RMS}}{\Delta Q_{RMS}} \right)_{No Sample}. \quad (13)$$

As aside, replacing the probe wire with a sample of unknown thermal resistance permits the thermal resistance and therefore thermal conductivity of the sample to be determined using Eq. (13). The caveat is that the sample's resistance and temperature coefficient of resistance must be known. This method is termed as the "Self-Heating Method".

Next, the sample is attached and the new slope of $Re_{3\omega,RMS}$ vs. Q_{RMS} is measured. By comparison of the ratio of the slopes, ϕ , where ϕ is defined as [5],

$$\phi \equiv \frac{\left(\Delta R_{e3\omega,RMS} / \Delta Q_{RMS}\right)_{\text{With Sample}}}{\left(\Delta R_{e3\omega,RMS} / \Delta Q_{RMS}\right)_{\text{No Sample}}} \quad (14)$$

The thermal resistance of the sample is found using,

$$R_{th,S} = \frac{1}{4} R_{th,P} \left(\frac{1}{4} \varepsilon^{-1} - 1 \right) \quad (15)$$

where $\varepsilon \equiv 1 - \phi$.

The sample's thermal conductivity is determined from its thermal resistance by $k_s = L_s / R_{th,S} A_s$, where the sample's cross-sectional area is $A_s = \pi(R_o^2 - R_i^2)$. In the present study, the inner radius is approximated using the ratio of the average inner to outer diameter supplied per batch by both samples manufacturers.

2.4. Heater/Sensor Device for in-situ SEM testing

The heater/sensor probe wire device used in the study is fabricated from commercially available Wollaston wire (Sigmund-Cohn Corp., Mt. Vernon, NY); the wire is composed of a 75 μ m silver sheath surrounding an approximate 500-750 nm platinum core. A concentrated nitric acid solution is used to selectively etch the silver sheath exposing the Pt core (Fig. 2a).

To increase throughput, the entire measurement system is composed of four etched Wollaston wires, numbered 1 to 4 in Fig. 2a. While only one probe wire is utilized per experiment, due to the extreme delicacy of the fine platinum wires a custom switch-box is used to independently activate each wire (not shown). The device comprises four probe wires, with nearly the same average diameters but with varying lengths, and thus with different thermal resistances. Figure 2b shows the four probe wires mounted inside the SEM chamber (FEI FE NanoSEM 600). All 4 probe wires are reachable by nanomanipulators inside the SEM chamber.

2.5. Probe Wire Thermal Resistance and Sensitivity

The length of the exposed platinum core, and thus the thermal resistance of the probe is readily controlled by carefully maneuvering the droplet of nitric acid during the etch process. This permits the sensitivity of the probe to be maximized relative to the sample being tested.

If the relative uncertainty in the measured temperature is $\delta\bar{\theta}/\bar{\theta}$ (where $\delta\bar{\theta}$ is approximately 0.05K (as measured from the linear regression of $R_{e3\omega,RMS}$ vs. Q_{RMS} using the experimentally determined temperature coefficient of resistance of the probe wire $\alpha \approx 0.0033$, and maintaining the average temperature rise of the probe wire, $\bar{\theta} \approx 10$ K), then the ratio of $\delta\bar{\theta}/\bar{\theta}$ to

the maximum relative uncertainty in the sample resistance, $\delta R_{th,S}/R_{th,S}$, is a quantifiable sensitivity factor [5]

$$s = \frac{\delta \bar{\theta} / \bar{\theta}}{\delta R_{th,S} / R_{th,S}}, \quad (16)$$

If $\delta R_{th,S}/R_{th,S} = 0.10$, Eq. (16) is readily solvable for maximum and minimum values of η . While maximum probe sensitivity occurs when the probe and sample's thermal resistance is $\eta = 1$, the uncertainty in the measured thermal resistance of the sample will be within 10 % of its true value if the actual value of η is between 0.077 and 12.923. The average thermal resistance of the all prepared Wollaston wire probes used in this study is $4.02 \times 10^7 \pm 1.15 \times 10^7$ W/K. Therefore, samples having thermal resistances as high as 5.20×10^8 W/K and as low as 3.11×10^7 can be effectively measured.

2.6. Method Validation

The analysis of the experiment and equipment setup is verified by both a 1ω and 3ω self-heating experiment on 99.99% Au wire. The Au wire is chosen for its uniformity of diameter (3.4% variation) over the etched Wollaston probe wire that has an average of a 17% variation in diameter. The 1ω and 3ω Au self-heating validation experiments result in a 2.3% and 3.6% difference from literature value (306.6 W/m-K), respectively. Because the Wollaston T-type probe method measures thermal resistance, diameter variation leads to twice the uncertainty in cross-sectional area resulting in a variation in thermal conductivity of no less than 34%.

Therefore, comparison of the measured thermal conductivity of the Wollaston probe wire with that of bulk platinum is infeasible.

The use of the suspended Pt wire as a thermal resistance sensor is also validated (Fig. 3). A separate length of etched Wollaston wire is soldered to a nanomanipulator and treated as a sample of unknown thermal conductivity. To maximize the sensitivity of the experiment, the sample length is chosen such that $\eta \approx 1$.

Although the lengths of etched Wollaston wire are sequentially cut from the same batch, sample and probe diameters both exhibit variations in diameter. Instead of comparing thermal conductivity of the probe wire to the sample, the thermal resistance per unit length of the Pt probe wire is compared to that of the thermal resistance per unit length of the sample Pt wire. 1ω and 3ω experiments measure the Pt sample's thermal resistance per unit length to be within 5.7% and 4.1%, respectively, of the Pt probe. Pt-EBID is deposited at the contact point to increase the contact area by more than 75% and thus similarly reducing thermal contact resistance (Fig. 3a). Figure 3b depicts the change in slope of $Re_{3\omega,RMS}$ vs. Q_{RMS} caused by the reduction in the average temperature of the Wollaston probe wire due to contacting the sample, and the subsequent reduction in the probe wire's average temperature due to the reinforcement of the sample-probe interface with Pt-EBID. Prior to applying the Pt-EBID, the measured sample's thermal resistance is 2.9 times greater, which emphasizes the importance of improving the thermal contacts, especially as sample diameters decrease.

3. MWCNT Samples

Two sample groups are investigated in the present study: 1) MWCNT samples synthesized via thermal CVD; and 2) MWCNT samples synthesized via thermal CVD and subsequently heat-treated at 3000°C for 20 hours (thermal annealed). The heat-treated thermal CVD MWCNT samples are acquired from US Nanomaterials Research (US4400, US4406, US4412). The second set of samples, termed “non-heat treated”, are comprised of thermal CVD grown MWCNTs purchased from US Nanomaterials Research (US4309, US4315) and NanoLab (PD15L5-20). The NanoLab samples were synthesized at $600 \pm 15^\circ\text{C}$ and all US Nanomaterials Research samples were grown at $665 \pm 15^\circ\text{C}$.

The samples tested have a high degree of variation in diameters, shapes, lengths, and straightness. Comparison of Fig. 4a to 4c and/or 4e indicates that the high temperature graphitization process shortens the lengths of the MWCNT samples by more than 75%. Adjacent nanotubes appear to become ‘seared’ together (Fig. 4b). A greater majority of heat-treated samples have debris attached to the outside sample walls when compared to the non-heat treated MWCNTs (Fig. 4f). The non-heat treated batches (US4309, US4315) have a higher degree of abrupt changes in angle (Fig. 4c and d) compared to the PD15L5-20 batch (Fig. 4e and f). The source of these angle changes are likely due to defects in the lattice structure of the CNTs [7].

3.1. Raman Spectroscopy

Raman Spectroscopy (excitation wavelength of 514 nm) is used to validate the improvement in graphitization and purity for the heat-treated sample batches compared to the non-heat treated sample batches. An assessment of both residual amorphous carbon and defects

is made by examining the ratio of the *D* band peak ($\sim 1350\text{ cm}^{-1}$) intensity to the *G* band peak ($\sim 1580\text{ cm}^{-1}$) intensity [18]. The *D* band (defect band) is activated by both the carbonaceous impurities with sp^3 bonding and fragmented sp^2 bonds. These features are indicative of MWCNT defects [19]. The *G* band is activated by contiguous sp^2 bonding, i.e., a high degree of crystallinity. Therefore, when comparing two sample groups, a smaller *D/G* band ratio is representative of a sample with fewer defects and a higher degree of graphitization. To date, standards to quantify purities, diameters, wall numbers, and most importantly growth conditions of MWCNT samples are not well established. Lacking a standardized MWCNT sample set, Raman spectroscopy remains a qualitative, yet effective, assessment of purity. It is important to note that the Raman laser used to activate the phonon modes within the samples has a spot size of $\sim 1\mu\text{m}$. Therefore the Raman response is an average response of not one specific sample, but a representative group of samples exposed to the laser.

Figure 5 compares the Raman intensity of 3 non-heat treated sample batches (US4309, US4315, and PD15L5-20) to the Raman intensity obtained from 3 heat-treated sample batches (US4400, US4406, US4412). The Raman intensity is normalized with the maximum *G* band peak. Comparison of Fig. 5a to Fig 5b suggests that a significant amount of defect healing and graphitization has occurred in the heat-treated samples during to the 3000°C annealing process.

. RESULTS AND DISCUSSION

4.1. Thermal Conductivity vs. Sample Quality

On a sample specific level, SEM images (including Figs. 6 and 7) are used to qualitatively categorize both the non-heat treated and heat-treated samples into three main categories: samples

with 1) minor defects; 2) moderate defects; and 3) severe defects. CNT side growth (branching) at angles to the main CNT tube axis have been previously shown to be caused by wall defects [7]. Besides branching, the specimens in the present study also show abrupt changes in diameter as well as the presence of excessive surface debris. None of the selected specimens from either manufacturer are considered ‘flawless.’ Not surprising, the mean thermal conductivity in specimens from the severe defects category is statistically less than those of the specimens from the moderate and minor categories. Samples described by the minor and moderate category are subsequently divided into heat-treated (Fig. 6) and non-heat treated (Fig. 7) sample groups. The severe category comprises of rejected sample group. In this manner, a filtering process was performed to remove samples having gross morphological deformities from the study.

A total of 29 measurements of MWCNT conductivity are performed. 6 non-heat treated and 15 heat-treated MWCNTs are measured to determine the effect of high temperature graphitization on thermal conductivity. 8 samples comprised the rejected group. The mean thermal conductivities and Raman D/G ratios of the non-heat treated MWCNT samples provided by US Nanomaterials Research and the non-heat treated MWCNT samples provided by NanoLab are found not to have a statistically significant difference. For this reason, both sample sets are placed into the same non-heat treated group.

The non-heat treated sample batches produce D/G ratios that are approximately 3.3 fold greater than the heat-treated batches indicating a significant presence of average defects and amorphous carbon content. Figure 8 suggests that samples selected from the heat-treated batches produce a mean thermal conductivity nearly 5 fold times (4.88x) that of the non-heat treated

group, 216 ± 149 W/m-K and 44 ± 29 W/m-K, respectively. Note the large standard deviations are due to the variations in thermal conductivity within the group and do not reflect measurement uncertainty. Comparison of the non-heat treated and heat-treated samples using a one-way analysis of variance (ANOVA) resulted in a *p-value* of 0.015 indicating that the graphitization process has a statistically significant effect on the thermal conductivity of the samples.

Due to the unique morphology of each sample tested, MWCNT thermal conductivity may be better evaluated on a more sample specific level. However, the mean thermal conductivity of all non-heat-treated samples is found to be similar to other CVD grown MWCNTs measured via the ‘Self-Heating’ of 1-2 mm long MWCNT bundles with estimated phonon mean free paths of a few nanometers [20] and vapor grown carbon fibers having diameters greater than 10 microns [21].

In the present study, the highest measured thermal conductivity is 730 ± 153 W/m-K for a heat-treated sample having a measured *OD* of 35 ± 4 nm, estimated *ID/OD* ratio of 0.29, and a length of 10.77 ± 0.04 μ m. Not surprising, this sample is the straightest of all samples measured and has the least number of visible physical defects (Fig. 6a). A small amount of surface debris is present on the sample and seems fused to the samples outer wall. When considering its straightness, the sample does not represent the majority of tested specimens.

The greater number of ‘kinks’ in the rejected sample group likely reduce phonon mean free path accounting for the reduced thermal conductivity. Interestingly, all 8 rejected samples came from the heat-treated sample group. The rejected sample group is found to have a thermal conductivity of 50 ± 28 W/m-K, where the standard deviation is due to the large variation of

thermal conductivities within the group and do not reflect the measurement uncertainty. Since the rejected group consists of all heat-treated samples and has a mean conductivity similar to that of the non-heat treated group, the reduction in thermal conductivity of these rejected samples suggest that the gross physical deformities negate the effect of graphitization. As described by Ref. [7], heat treatment even at high temperatures of 3000°C is unable to heal major defects. Therefore it is likely these specific samples contained severe defects prior to heat-treatment, but were not representative of the majority of heat-treated MWCNTs as shown by their decreased *D/G* Raman peak ratio.

The measured thermal conductivities do not correlate to the sample outer diameter (Fig. 9a). Outer diameter measurements may correlate to thermal conductivity, since smaller diameter tubes generally have fewer wall numbers permitting less inter-wall phonon scattering [2]. Following this reasoning, a single wall carbon nanotube has the highest theoretical thermal conductivity. If a correlation of thermal conductivity to diameter of the samples tested in the present study exists, the correlation is likely to be unnoticeable due to the variations in the structural quality.

It has been proposed that shorter sample lengths may be responsible for a reduction in phonon mean free paths and thus apparent thermal conductivities [22]. Similar to diameter, the measurement of these effects places a strict demand on sample quality.

The magnitude of the thermal conductivities reported in the present study are below the highest measured MWCNT of approximately 3000 W/m-K [1]. However, the variation of

specimen quality makes comparison to other literature values especially difficult. Very little information is available on the quality and processing techniques of the tested MWCNTs reported in the literature. The heat-treated sample group measured a mean thermal conductivity in agreement with the individual MWCNT measurement measured via self-heating [4]. The variation in an individual MWCNT's crystallinity and amount of residual catalyst material between samples is likely to account for the wide variations in the reported literature values of an isolated CNTs thermal conductivity (Fig 9b).

Comparing the average 20 % relative uncertainty in the thermal conductivity of each sample tested to the 71% variation about the mean of the heat-treated sample group and the 180% variation about the mean of the non-heat treated sample group suggests that variations in sample quality within each sample group are significant. The large variations are likely due to wall defects in the heat-treated group and both wall defects and residual Fe catalyst in the non-heat treated group.

4.2. Contact Resistance and Other Sources of Uncertainty

Thermal contact resistance at the sample-probe and sample-manipulator interfaces is said to stem from two possible sources, heat flow restriction due to surface roughness of the contacting surfaces and mismatch in the phonon density of states at the interface between the MWCNT sample and Pt-EBID. Since the probe wire is composed of Pt, the contact thermal resistance is expected to be minimized by the use of Pt-EBID. This is assuming that vaporized residual carbon is not excessively deposited on the interface with the SEM electron beam prior to the Pt-EBID deposition. Deposition of residual carbons is avoided by limiting unnecessary imaging at the EBID site prior to deposition. Also, increasing the length of the Pt-EBID pads on

the specimen should improve thermal contact resistance by increasing the contact area. If thermal contact resistance were explicitly known, the magnitudes of the reported thermal conductivities would increase. Currently the probe-sample thermal contact resistance is attempting to be measured by changing the length of the sample while maintaining the original probe-sample contact. Regardless of the thermal contact resistance values, comparisons between sample groups using the Wollaston T-type probe method are highly effective.

Excluding the effect of thermal contact resistance, the largest source of experimental error lies in the measurement of sample diameter and the definition of an effective sample diameter if the diameter lacks uniformity along the sample length. The SEM is capable of making repeatable diameter measurements with a conservative uncertainty of ± 4 nm. Any variation in sample diameter will add to this uncertainty. Since thermal conductivity is a function of the sample cross-section area, the relative uncertainty in sample diameter, $\delta D_o/D_o$, is doubled. The average relative uncertainty in sample diameter for all measured samples in this study is 9 %, and is dominated mostly by non-uniformity of sample diameter. Other uncertainties include sample lengths, $\delta L/L$ (~ 1 %) [23], room temperature probe electrical resistance, $\delta R_{eo}/R_{eo}$ (< 0.1 %), and temperature coefficient of resistance of the probe, $\delta \alpha/\alpha$ (2.2 %). These uncertainties in conjunction with the error in neglecting radiation heat loss (~ 0.5 %) and the aforementioned sensitivity of the Wollaston T-Type probe results in a relative uncertainty of all measurements to be approximately 20 %.

5. CONCLUSION

This study highlights the beneficial effects of high temperature heat treatment ($\sim 3000^\circ\text{C}$) on the thermal conductivity of CVD grown MWCNTs when compared to non-heat treated CVD grown MWCNTs. A 4.9 fold increase in thermal conductivity is obtained for MWCNT samples which undergo a 20-hour 3000°C post annealing heat treatment. However, in most samples defects are found to negate any advantage of the heat treatment process. Of the 29 samples tested, the highest measured thermal conductivity is $730 \pm 153 \text{ W/m-K}$. Variations in the physical structures of the sample are seen within each sample group, and between each sample group with the highest values of thermal conductivity being measured in the straightest heat-treated samples.

ACKNOWLEDGEMENTS

The authors would like to thank Chris Dames for his extremely useful discussions on the preparation and execution of the hot wire probe method. The authors would also like to acknowledge the support of the Air Force Office of Scientific Research (AFOSR) grant FA9550-08-1-0372 and NSF MRI grant CMMI-0922968 for conducting the research reported in this paper.

APPENDIX I

The heating current used to Joule heat the Pt probe is driven at a sufficiently low frequency to prevent a phase shift between the heating frequency and the temperature response. This is achieved by choosing a heating frequency whose period is less than or equivalent to the thermal diffusion time τ of a suspended wire, where $\tau = L^2/\alpha$. To verify the operational

frequency range of the experiment, the Pt probe wire is modeled as a 1D wire having constant cross-section Area, A , Length L , density ρ , and heat capacity C . Homogeneous temperature boundary conditions $\theta(0,t) = \theta(L,t) = 0$, and initial condition $\theta(x,0) = 0$, along with Joule heating (current $I_{1\omega}e^{i\omega t}$) is solved together with the time dependent governing equation

$$\frac{\partial \theta(x,t)}{\partial t} = \alpha \frac{d^2 \theta(x)}{dx^2} + \frac{I_{1\omega}^2 R_{eo} e^{i2\omega t}}{\rho C L A} \quad (17)$$

Using the method of eigenfunction expansion, the spatially average series solution of Eq. (17) is written as

$$\begin{aligned} \bar{\theta}(\omega) &= \frac{1}{L} \int_0^L \theta(x, \omega) dx \\ &= \sum_{n=1}^{\infty} \frac{4 I_{1\omega}^2 R_{eo}}{\rho C L A} \frac{(1 - (-1)^n)}{(n\pi)^2} \frac{e^{i2\omega t} - e^{-\tau(n\pi)^2 t}}{(i2\omega + (n\pi)^2 / \tau)} \end{aligned} \quad (18)$$

The frequency dependent thermal transfer function is then

$$Z(\omega) = \frac{\bar{\theta}}{Q(t)} = \sum_{n=1}^{\infty} \frac{4}{\rho C L A} \frac{((-1)^n - 1)}{(n\pi)^2} \frac{(e^{i2\omega t - \tau(n\pi)^2 t} - 1)}{i2\omega + (n\pi)^2 / \tau} \quad (19)$$

Eq. (19) highlights the importance of minimizing the frequency to maintain the real part of the thermal transfer function and thus the measured 3rd harmonic voltage signal. The denominator of the last term of Eq. (19) validates that longer Wollaston probe wires (larger $\tau = L^2/\alpha$) require

lower frequencies to minimize the phase difference between the heating current and the thermal response. As frequency approaches zero, the steady state result utilized in Eq. (2) is recovered.

$$Z(\omega \rightarrow 0) = 4R_{th,P} \sum_{n=1}^{\infty} \frac{(1 + (-1)^{n+1})}{(n\pi)^4} = \frac{R_{th,P}}{12} = Z_o \quad (20)$$

REFERENCES

1. Kim, P., L. Shi, A. Majumdar, and P. McEuen, Phys. Rev. Lett. **87**, (2001).
2. Fujii, M., X. Zhang, H. Xie, H. Ago, K. Takahashi, T. Ikuta, H. Abe, and T. Shimizu, Phys. Rev. Lett. **95**, 065502 (2005).
3. Choi, T.Y., D. Poulikakos, J. Tharian, and U. Sennhauser, Appl. Phys. Lett. **87**, 013108 (2005).
4. Choi, T.-Y., D. Poulikakos, J. Tharian, and U. Sennhauser, Nano Lett. **6**, 1589 (2006).
5. Dames, C., S. Chen, C.T. Harris, J.Y. Huang, Z.F. Ren, M.S. Dresselhaus, and G. Chen, Rev. Sci. Instrum. **78**, (2007).
6. Porro, S., S. Musso, M. Giorcelli, A. Chiodoni, and A. Tagliaferro, Physica E **37**, 16 (2007).
7. Andrews, R., D. Jacques, D. Qian, and E.C. Dickey, Carbon **39**, 1681 (2001).
8. Jin, R., Z.X. Zhou, D. Mandrus, I.N. Ivanov, G. Eres, J.Y. Howe, A.A. Puretzky, and D.B. Geohegan, Physica B **388**, 326 (2007).
9. Holland, L.R., *Physical Properties of Titanium. III. The Specific Heat*. Vol. 34. 1963: AIP. 2350.
10. Birge, N.O. and S.R. Nagel, Rev. Sci. Instrum. **58**, 1464 (1987).
11. Dames, C. and G. Chen, Rev. Sci. Instrum. **76**, 124902 (2005).
12. Lu, L., W. Yi, and D.L. Zhang, Rev. Sci. Instrum. **72**, 2996 (2001).
13. Zhang, X., S. Fujiwara, and M. Fujii, Int. J. Thermophys. **21**, 965 (2000).
14. Wang, J.L. and et al., J. Phys. D Appl. Phys. **42**, 105502 (2009).
15. Mahanta, N.K. and A.R. Abramson. *ASME/JSME 2011 8th Thermal Engineering Joint Conference*. 2011. Honolulu, Hawaii, USA: ASME.
16. Shi, L., D. Li, C. Yu, W. Jang, D. Kim, Z. Yao, P. Kim, and A. Majumdar, J. Heat Transf. **125**, 881 (2003).
17. Using an analytic 1D steady state model to represent a 1 mm Pt probe wire having a 750 nm diameter, omission of a radiation term in Eq. (7) is found to contribute approximately 0.5% error in the measured electrical resistance of the probe wire.
18. DiLeo, R.A., B.J. Landi, and R.P. Raffaele, J. Appl. Phys. **101**, 064307 (2007).
19. Dresselhaus, M.S., A. Jorio, M. Hofmann, G. Dresselhaus, and R. Saito, Nano Lett. **10**, 751 (2010).
20. Yi, W., L. Lu, Z. Dian-lin, Z.W. Pan, and S.S. Xie, Phys. Rev. B **59**, R9015 (1999).
21. Heremans, J. and C.P. Beetz, Phys. Rev. B **32**, 1981 (1985).
22. Mingo, N. and D.A. Broido, Nano Lett. **5**, 1221 (2005).
23. The reported relative uncertainty in sample length excludes the rejected sample group.

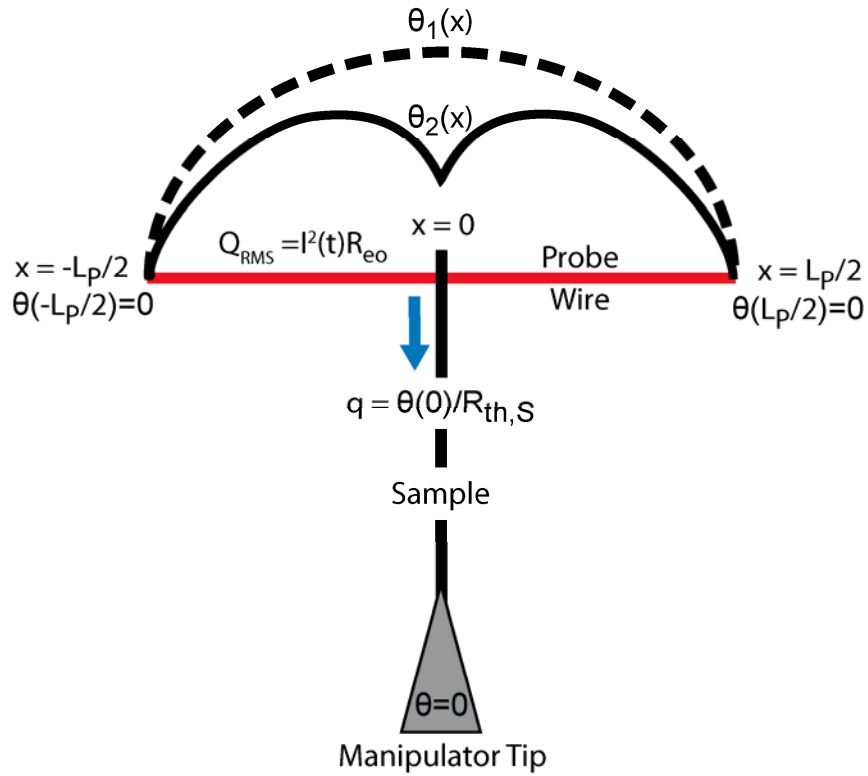


Figure 1. Schematic of Pt probe wire (*red line*), and attached sample (*horizontal black line*). The thermal resistance of the sample is incorporated into the analytical model using a flux boundary condition at $x = 0$. The parabolic dashed line, $\theta_1(x)$, represents the increase in temperature of the probe prior to coming into contact with the sample. The solid line, $\theta_2(x)$, represents the increase in temperature of the probe wire following the contact with the sample. The manipulator tip and each end of the probe wire are assumed to remain at ambient temperature conditions, $\theta = 0$.

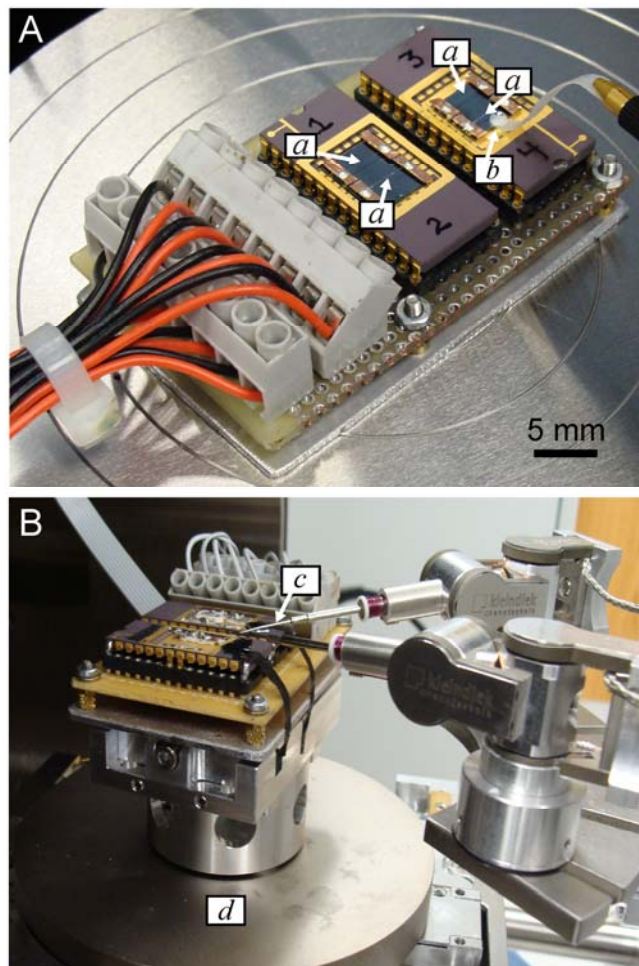


Figure 2. Images of sensor package (A) during the Wollaston etching process. The package contains two removable chipsets. Each chipset has two Wollaston probe wires marked 1-4. Each Wollaston wire is labeled (a). The Wollaston wires are shown connected to copper contact pads using an electrically conductive silver epoxy. Label (b) marks the droplet of nitric acid on the Teflon spoon used to etch the Ag clad from the Wollaston to reveal the Pt core. (B) The sensor package mounted inside the SEM chamber with micromanipulators marked (c) and SEM stage marked (d).

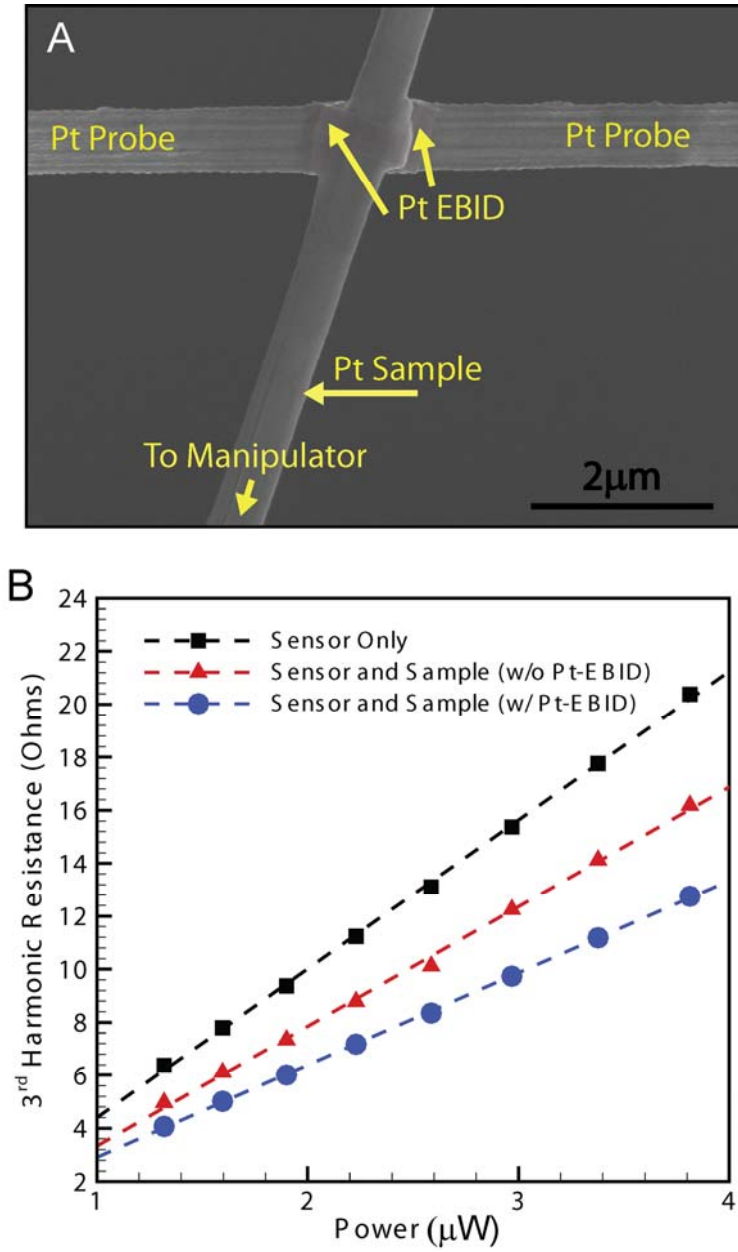


Figure 3. (A) SEM image of the validation experiment where a similar length of etched Wollaston Pt wire is used as both the T-type probe and the unknown sample. Image shows the use of Pt-EBID deposition to decrease thermal contact resistance. (B) $Re_{3\omega, RMS}$ vs. Q_{RMS} plot prior to sample connection, following sample connection, and with the sample connection improved using Pt-EBID.

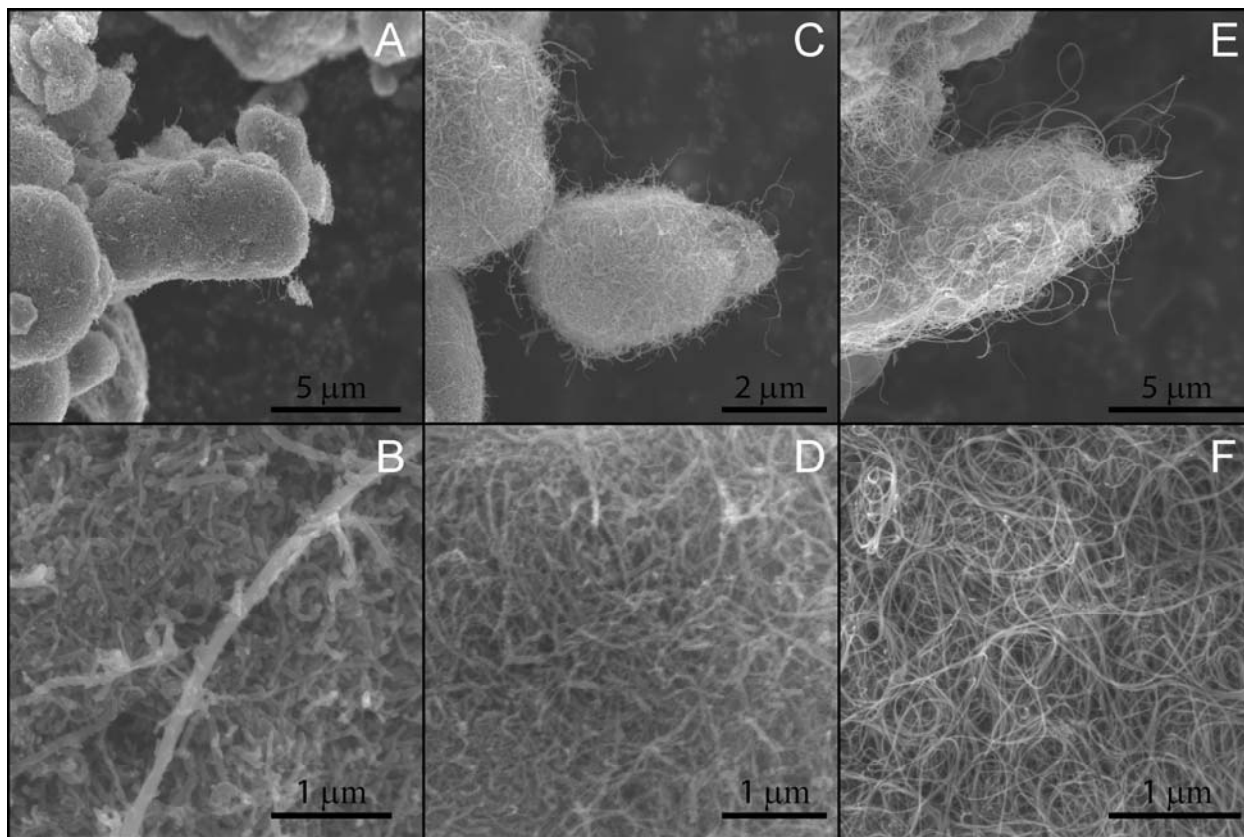


Figure 4. Scanning electron microscope (SEM) images of MWCNTs batches from which samples are selected. (a) and (b) US Nanomaterials Research: heat-treated batch representative of all batches US4400, US4406, and US4412; (c) and (d) US Nanomaterials Research: non-heat treated batch representative of batches US4309 and US4315; (e) and (f) Nanolab: non-heat treated batch (PD15L5-20).

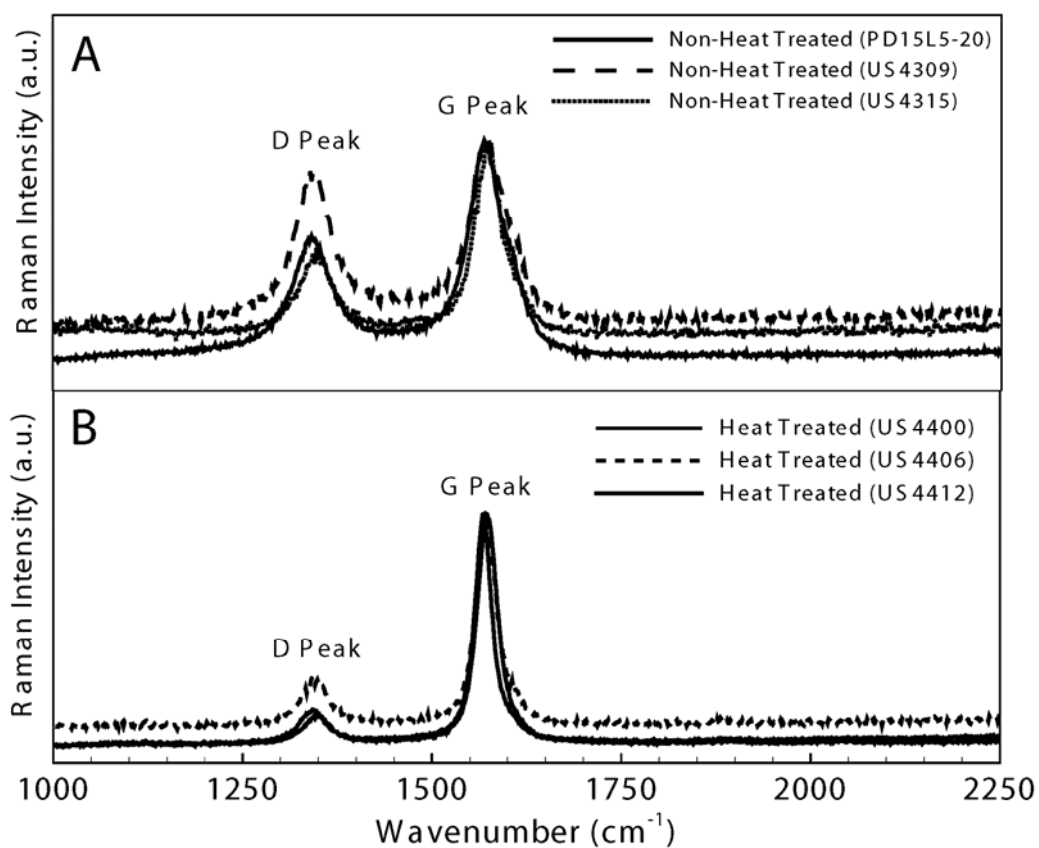


Figure 5. Raman intensity versus wavenumber (514 nm excitation) of (a) sample batches PD15L5-20, US4309, US4315 of which non-heat treated specimens are selected; (b) sample batches US4400, US4406, US4412 of which heat-treated specimens are selected. The Raman intensity is normalized by the maximum value of the *G* peak for clarity.

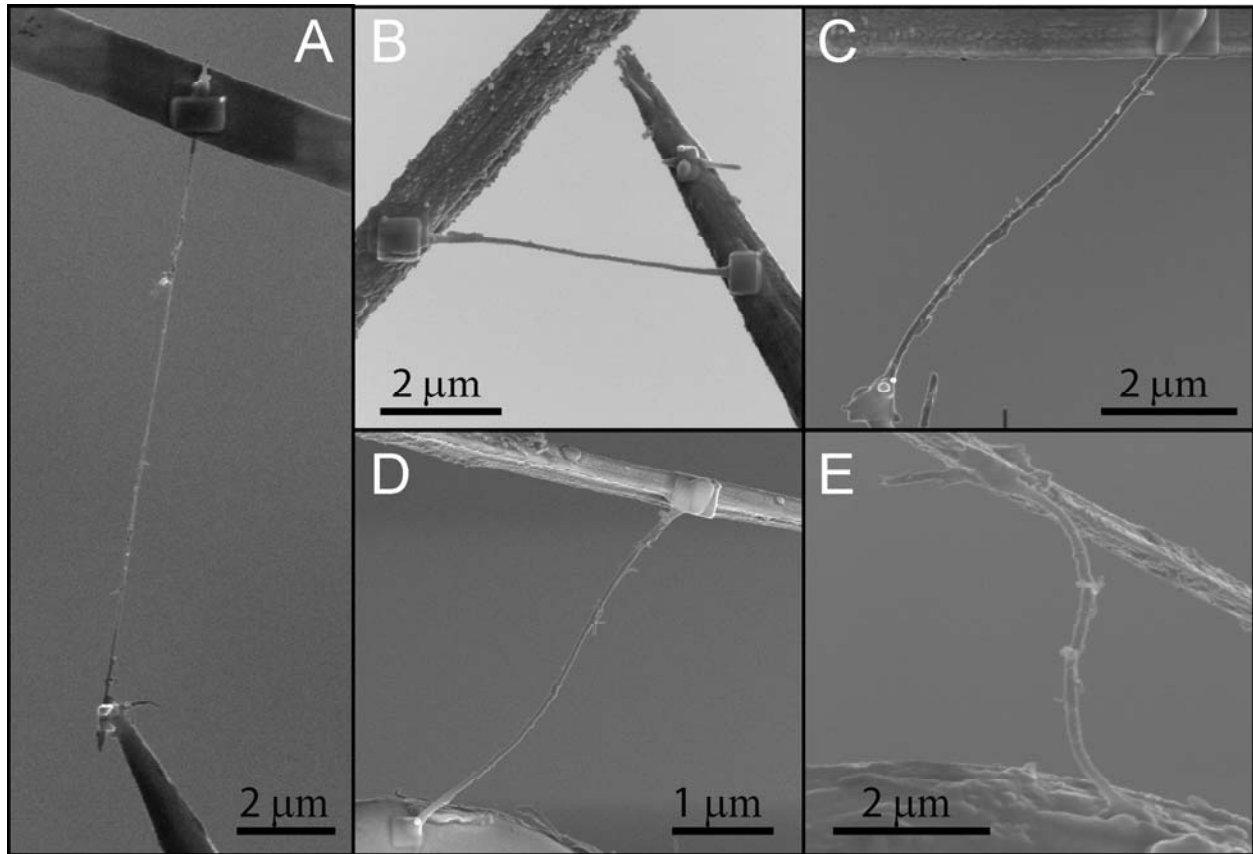


Figure 6. SEM micrographs of experiments from the heat-treated sample set. In each case the Pt probe wire is pictured above the manipulator tip with sample joining the probe wire to the manipulator. (A) Highest measured thermal conductivity (730 ± 152 W/m-K), statistically an outlier; (B) and (C) the two highest measured values of the heat-treated samples that are within the 20% confidence interval about the groups mean, 290 ± 28 W/m-K and 254 ± 42 W/m-K, respectively; (D) and (E) the two lowest measured values of the heat-treated samples, 80 ± 16 W/m-K and 67 ± 11 W/m-K, respectively.

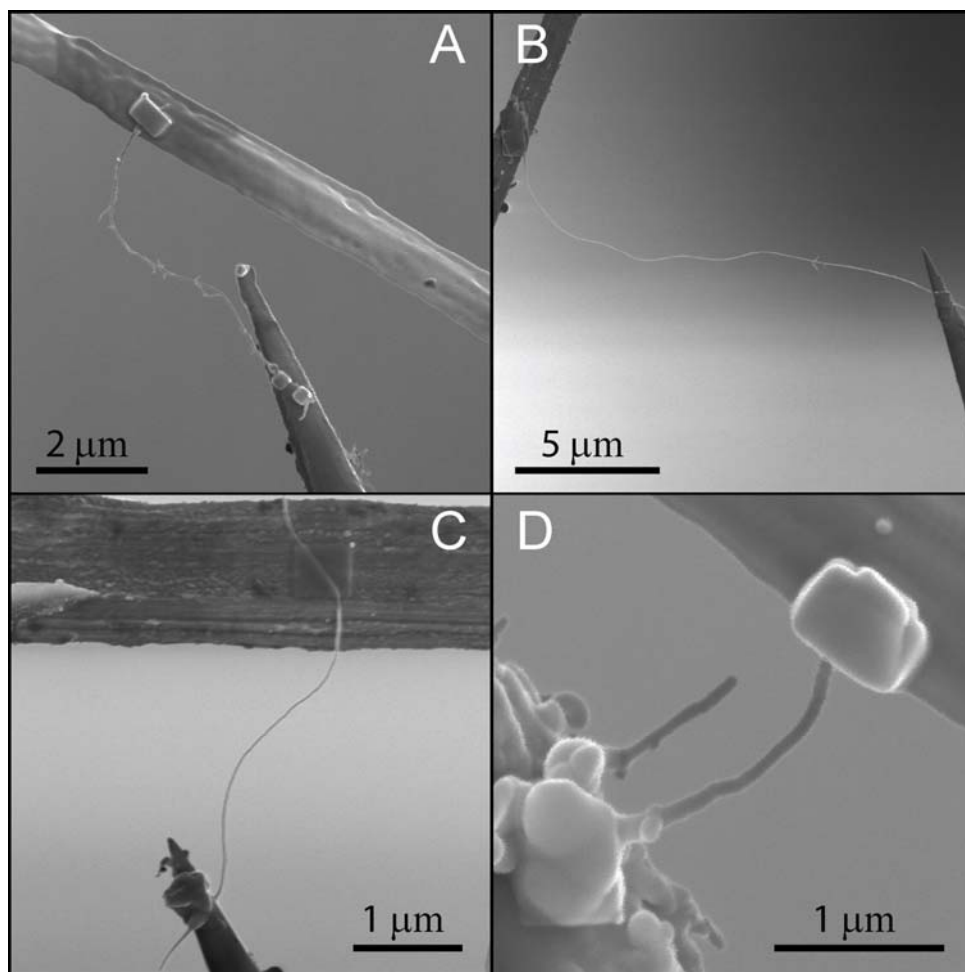


Figure 7. SEM micrographs of experiments resulting in the two highest (A and B) and two lowest (C and D) measured thermal conductivity values of the non-heat treated sample group. (A) 102 ± 17 W/m-K; (B) 61 ± 6 W/m-K; (C) 24 ± 4 W/m-K; (D) 21 ± 9 W/m-K. In each case the Pt probe wire is pictured above the manipulator tip with sample joining the probe wire to the manipulator.

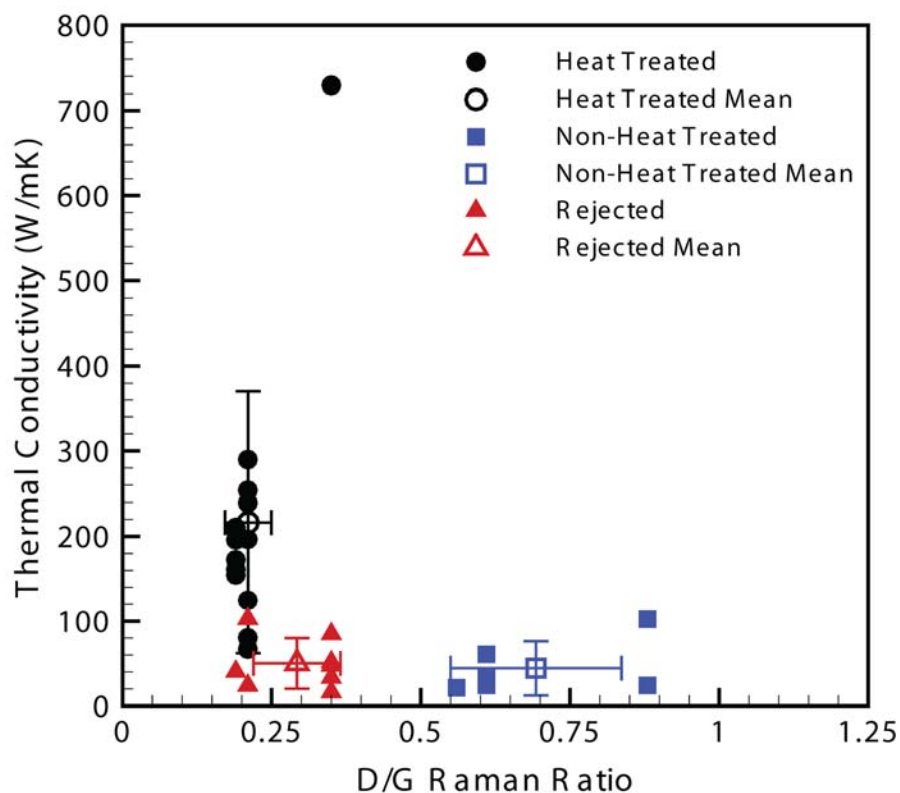


Figure 8. Mean thermal conductivity of the three measured sample groups plotted versus the ratio of the *D* to *G* Raman spectroscopy peaks as measured on each respective sample batch using a 514 nm excitation source. Error bars correspond to the standard deviation calculated from the variance of all samples within each sample group and do not reflect the measurement uncertainty.

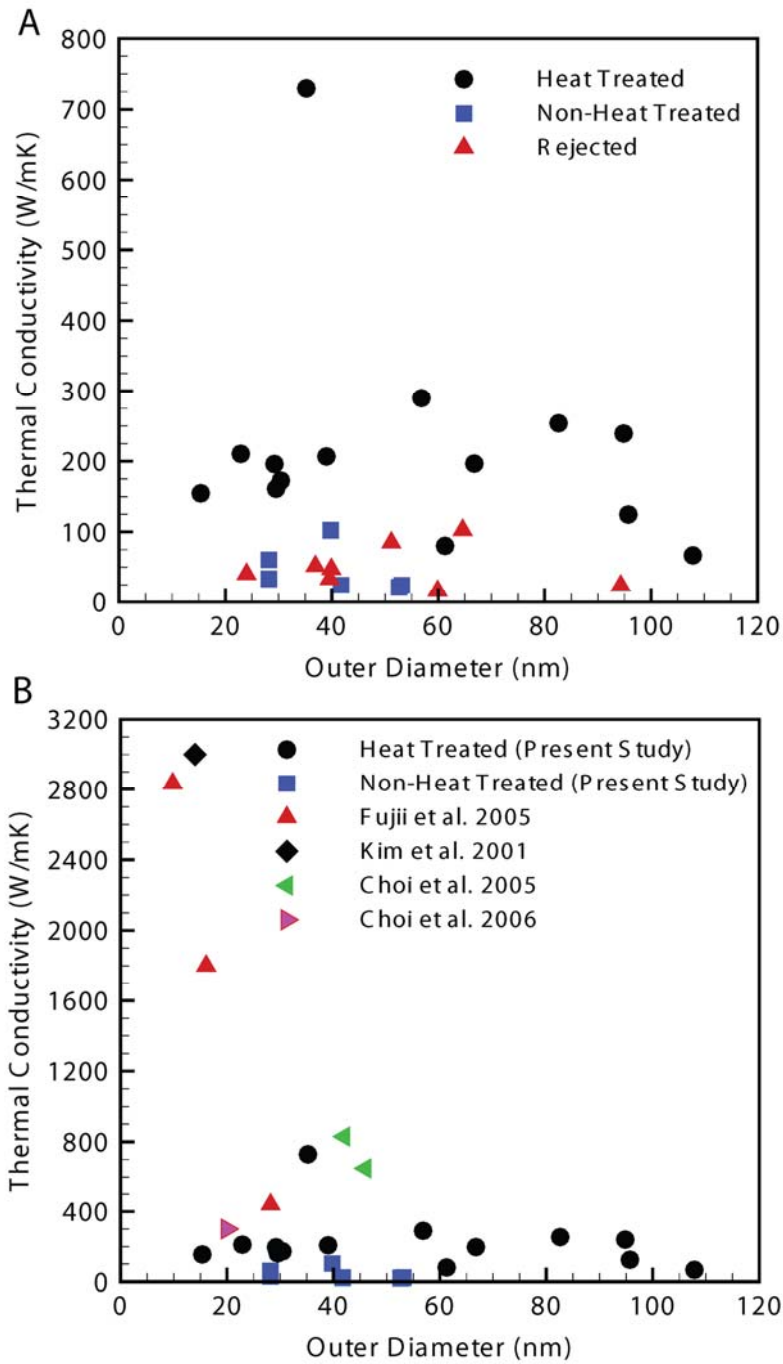


Figure 9. (A) Measured thermal conductivities of the heat-treated, non-heat treated, and rejected sample groups; (B) Thermal conductivity measurements of both heat-treated and non-heat treated sample groups plotted against references [1-4].

APPENDIX II

THICKNESS AND TEMPERATURE DEPENDENT THERMAL CONDUCTIVITY OF NANOSCALE TIN FILMS

ABSTRACT

Thin films in general exhibit different thermal properties compared to bulk due to size effect [1-3]. In this study, the thermal conductivity of sputtered Sn films of thickness $500 \text{ nm} \pm 50 \text{ nm}$ and $100 \text{ nm} \pm 20 \text{ nm}$ are obtained from 55K to 300K and from 40K to 310K, respectively, using the three omega method. The thermal conductivity of 500 nm thin film at room temperature is $46.2 \pm 4.2 \text{ W/m-K}$, which is lower when compared to its bulk value of 63 W/m-K , and increases gradually as the temperature is lowered to 55K. In contrast, the thermal conductivity of the 100 nm thin film exhibits even reduced thermal conductivity, $36 \pm 2.88 \text{ W/m-K}$ at 300K, when compared to the 500 nm film, and decreases as the temperature is lowered. The reduction in thermal conductivity of Sn thin film may be due to the pronounced effects of electron scattering at the grain boundaries as well as the twin boundaries in addition to the scattering from the boundary surface at lower temperatures. These experimentally determined thermal conductivities are compared to models that take into account size effects on thermal conductivity of metallic films based on electronic scattering as proposed by Fuchs-Sondheimer (FS), Mayadas-Shatzkes (MS) and Qiu and Tien (QT). The experimentally measured thermal conductivity of Sn films is in good agreement with the MS model indicating the importance of the grain boundary scattering. Thickness measurements are obtained by ellipsometry and profilometer. The estimation of the mean grain size in both films and the evidence of twin boundaries are obtained by Atomic Force Microscopy.

INTRODUCTION

Thin films (metal or dielectric) are essential constituents in current functional devices having myriad of applications relevant to energy transport and energy conversion technologies such as thermoelectrics, Nano-Electro-Mechanical Systems (NEMS), optoelectronics, solar, photovoltaics *etc.* Understanding the thermal transport and more fundamentally the behavior of heat carriers (electron, photon and phonon) in these materials is critical to their reliable and robust performance, thus accommodating denser circuits

and higher switching speeds. Nanoscale thin films of tin (Sn), are important as a solder material in microelectronics applications and as a thermal interface material to improve thermal conductance between two non-conforming surfaces. This is due to its properties of reasonably good thermal conductivity (64 W/m-K at room temperature) [4], lower melting point (505 K) [5] and its ability to conform well to surface irregularities. The total thermal resistance of a thermal interface material (TIM) depends on its thermal conductivity, bond line thickness (BLT) and the contact resistances of the TIM with the two bounding surfaces. In this regards, a high thermal conductivity material and lower bond line thickness sufficient to fill the interfacial gap between the asperities is desirable to improve the thermal contact conductance.

Reduced thermal conductivity at nanoscale due to size effects was initially reported [6] in the resistivity measurements of metallic thin films specifically when the film thickness was comparable to the mean free path of electrons. This anomaly was first explained by Fuchs-Sondheimer theory [7], attributing it to the scattering of electrons at the surface. However, the Mayadas-Shatzkes theory [8], proposed much later, was in better agreement with the experimental results that showed increase in resistivity with decreasing film thickness. Even though both theories are fundamentally derived from the well-known Boltzmann transport equations, the MS theory also accounts for the grain boundary scattering in addition to the surface boundary scattering of electrons. Recent experimental [9-10] and modeling [11-12] studies on nanoscale polycrystalline metallic thin films reported reduced thermal conductivities compared to their bulk value and additionally in some cases, the violation of Wiedemann-Franz law. The most widely studied metallic films at nanoscale are aluminum, copper and gold. With regards to Sn, the electrical resistivity of tin films from 2 mm down to 3 μ m thickness have been investigated thoroughly up to very low temperatures [6]. The electrical resistivity has been observed to be increasing with decreasing tin-foil thickness and with increasing temperature. The shortening of the mean free path due to inelastic collision of the conduction electrons with the boundary (lateral) surfaces of the metal have been understood to increase the resistivity at thicknesses comparable to the electron mean free path. However, there has been limited investigation into the thermal properties of tin particularly as a function of temperature. Previous studies have reported the measurements of thermal conductivity of pure tin (99.999%, bulk) either at very low temperatures, 3.5K – 25K [13], or at very high temperatures 373K-873K [14]. Recently, Choi et al [15], have reported the thermal diffusivity measurement of 2 μ m Sn film.

Transient methods for the measurement of thermal transport properties are widely accepted and can be divided into frequency-domain and time-domain techniques. The most popular methods under these domains are: (1) three omega method that employs an electrically heating source, a metal line

heater/sensor, and a moderate frequency modulation range (0.1Hz-200KHz); and (2) thermoreflectance methods (TDTR and FDTR) that use ultra-fast laser pulses with modulating frequency up to 80 MHz. The high frequency range is advantageous for the measurement of heat diffusion in very thin (angstrom scale) films and across interfaces. The three omega method, developed by Cahill *et al* [16], is the most reliable and versatile technique for the measurement of thin films and bulk materials. The method circumvents errors due to radiation and convection and its implementation is relatively inexpensive. Recent modifications to Cahill's original three omega method [16] has extended its applicability to electrically conducting and semiconducting films [17-20], multi-layer structures including composites [2, 21-23, 24-25] in addition to estimating the anisotropic thermal conductivities of a thin film [21,23] and the interfacial thermal resistance [2, 21-23].

In this work, the differential three omega method [21-23] is employed for the measurement of thermal conductivity of soft nanoscale tin (Sn) films of thickness, 500nm, from 55K to 300K and 100nm, from 40K to 310K respectively. The thermal conductivity of these films is compared to a previous study to highlight the influence of thickness on thermal transport. The experimental data is then compared to previously proposed models based on the electron mean free path comparable to thickness or average grain size. The temperature dependent thermal conductivity of these films is discussed by examining the electron and phonon contribution separately. Additionally, a brief overview of three omega method, the sample preparation including the shadow mask microfabrication and the calibration of deposited metal line is presented.

THREE OMEGA TECHNIQUE: A BRIEF OVERVIEW

In this section, a brief overview of the general three omega technique is presented to better illustrate the required changes for accommodating soft metallic films. The three omega method generally proceeds by applying an alternating current of frequency ω through a metal heater line (see Fig.1) that has been directly deposited on an electrically insulating sample. This current heats the sample at a frequency of 2ω due to Joule heating, producing temperature oscillations also at a frequency of 2ω with an amplitude, say, $\Delta T_{2\omega}$, and phase difference ϕ . Since the resistance of pure metals increases linearly with temperature, the temperature oscillations introduce resistance oscillations in the metal line at a frequency of 2ω . The resistance oscillations at 2ω , with the source current at frequency ω , generate a small oscillating voltage signal across the metal line at 3ω . The amplitude of the 3ω voltage $V_{3\omega}$ is given in terms of the voltage amplitude at the first harmonic, V_{ω} , by

$$V_{3\omega} = \frac{1}{2} I_{1\omega} R_{e_0} \alpha \Delta \bar{\theta} = \frac{1}{2} V_{\omega} \alpha \Delta T_{2\omega} \quad (0)$$

Here, $I_{1\omega}$ is the current sent to the metal line, R_{e_0} is the average resistance and $\Delta T_{2\omega}$ represents the temperature oscillations of the metal line at frequency 2ω . The temperature coefficient of resistance α needs to be calibrated for every sensor microfabricated on the sample at the start of experiment.

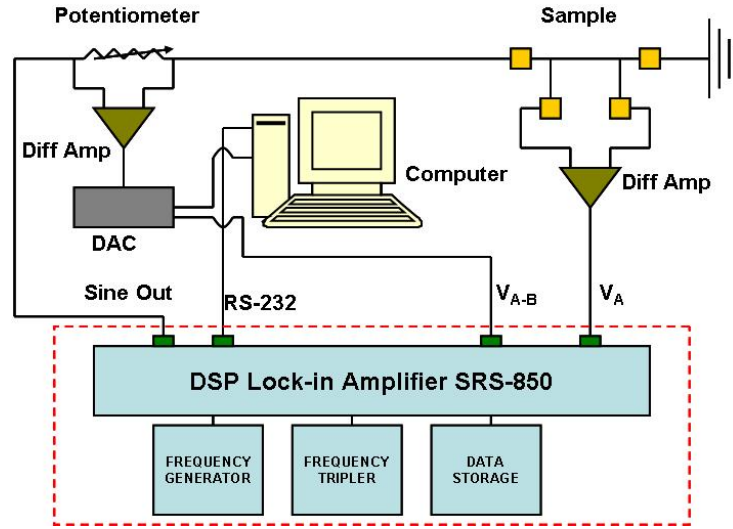


Fig.1 Block-diagram representing the three omega electrical circuit.

In the present work, in order to determine the temperature rise in the deposited metal line the third harmonic voltages were isolated using a lock-in amplifier (Stanford Research Systems SR850) which operates over a wide range of frequencies (1 mHz–102 kHz) in conjunction with a custom designed circuitry based on Fig.1. Unity gain differential amplifiers were employed to acquire the voltage signal across the potentiometer and the metal line (that acts as a heater/ sensor) on the sample and a 12 bit multiplying digital-to-analog converter, DAC (Analog Devices No. 7541KN) in conjunction with an operational amplifier (Analog Devices No. 549KH) so that the first harmonic differential signal could be balanced out. The set-up has been automated using LabVIEW 8.5. The LabVIEW program also helps in balancing the first harmonic voltage at the reference resistor and the sample resistor to a greater degree of precision. The bits of the multiplying DAC are set ‘on’ and ‘off’ to balance the first harmonic signal from the sample. This step is equivalent to making adjustment on the potentiometer manually. However, when

automated, the digital signal precision is close to 4 decimal places, reading V_{A-B} on the lock-in equal to $\pm 0.0001V$. A multi-DAQ card (NI-6025E) is used for communicating with the multiplying DAC through LabVIEW. The third harmonic voltages at a specified temperature were measured by performing a logarithmic frequency sweep typically from 50 Hz to 10 kHz. Finally, the thermal conductivity of the sample was evaluated by measuring the frequency dependence of the temperature oscillations in the metal line. By correlating the experimentally determined voltage to the analytically derived temperature changes, the thermal conductivity of the sample was determined without the knowledge of the film's density and specific heat.

The analytical derivation based on an earlier work by Cahill and Pohl [26] requires the assumptions that the heater be considered of infinite length and that the sample be effectively semi-infinite. Additionally, the method requires the thermal waves to penetrate a depth greater than the heater width into the sample, satisfying the approximation of an infinite line source. The three omega method can also be applied to a film on a substrate type configuration, by employing either the slope method or the differential-3 ω approach. For these methods, the thin film is assumed thin enough such that essentially one dimensional Fourier conduction model can be applied for analysis and interpretation of experimental data. Specific conditions that must hold to ensure accurate analysis are that $d_f > 2w \gg t_f$, i.e., the thermal penetration depth, d_f , must be greater than the heater width and be much larger than the film thickness, t_f . For the experimental investigation discussed herein, the thermal penetration depth and the heater width were greater by at least an order of magnitude than the film thickness to ensure the validity of these approximations. Additionally, the thickness of the underlying substrate t_s must be such that the condition $t_s \gg d_f \gg w$ is maintained to avoid back surface reflection and assure the validity of the line source and semi-infinite substrate approximations. Additional details about the three omega technique can be found from various references [1-3, 16-18, 21-23, 26] and are therefore not discussed in detail.

EXPERIMENT

For the experimental procedure, the differential three omega technique [21-23] was utilized to measure the thermal conductivity of a (~500 nm) thick Sn film and a (~100 nm) relatively thin Sn film, each deposited on a silicon substrate. The assumptions described above were validated by selecting an appropriate frequency range to ensure sufficient penetration depth and a suitable heater dimension to satisfy the inequality conditions. Additionally, in order to restrict the error introduced by various

approximations, the numerically obtained exact solution of the film on substrate system, as described by Kim et al [2], Borca-Tascuic et al [21] and more recently by Tong et al [23], has been utilized.

A. SAMPLE PREPARATION

Thin films of Sn (99.999% pure, Target from Kurt Lesker) of required thickness was deposited on a silicon substrate by sputtering (Denton Vacuum, Discovery 18) at a base pressure of 2×10^{-7} Torr. Since tin has lower melting point, the target was procured with a copper back plate for dissipating heat during the deposition process. The thickness of the films was measured using a Dektak stylus profilometer. Tin being electrically conducting, an insulating layer was needed so that heater/ sensor metal line does not come in direct contact with the underlying tin layer for measurement. In order to prevent heating of the tin thin film, low temperature deposition of ~ 300 nm SiO_2 was achieved using a Plasma Enhanced Chemical Vapor Deposition (PECVD) process. A typical PECVD process operates at 300°C or higher, but tin melts at a temperature of 230°C , lower than this. Therefore, a procedure described elsewhere (for polymer samples) [20] to deposit the SiO_2 using a tetraethylorthosilicate (TEOS) precursor was employed at a processing temperature of 150°C . Before every deposition an autoclean procedure and outgassing steps were executed to remove any source of contamination in the machine. The final condition of the sample was confirmed after the metal line deposition revealed no continuity between heaters located on the same sample surface. A resistance value of the order 10^6 indicated that the oxide layer provided sufficient insulating capacity to run the experiment.

The aluminum metal heater line deposition was achieved by magnetron sputtering using a microfabricated shadow mask as shown in Fig.2. The shadow mask is used in order to avoid the conventional photolithography procedure every time in addition to making it available for a wide variety of materials that cannot survive the wet etching process. Aluminum heaters of widths $25\mu\text{m}$, $50\mu\text{m}$ and $100\mu\text{m}$ were deposited using these shadow masks. After heater line deposition, the diced samples were placed in a 24-pin side braze package so that wires could be bonded to the heater pads using either ultrasonic bonding or epoxy bonding. The heater width and length were verified by the non-contact Nanovea optical profilometer (Fig.3).

(a)

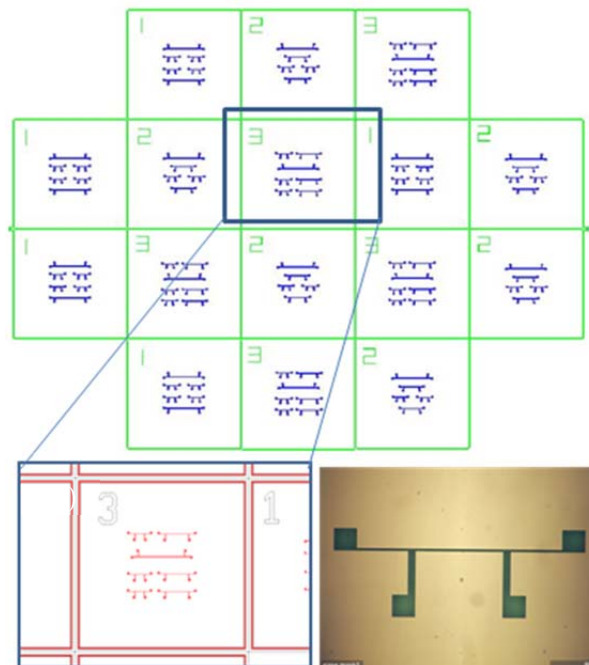


Fig. 2:(a)A Schematic representation of the footprint of stencil mask on a 4" Si wafer. The design accommodates 16 individual re-usable Si shadow masks with heaters of widths $25\mu\text{m}$ to $100\mu\text{m}$ etched on it using Deep Reactive Ion Etching (DRIE) process. (b) Optical microscopy image of an etched $25\mu\text{m}$ heater on the shadow mask.

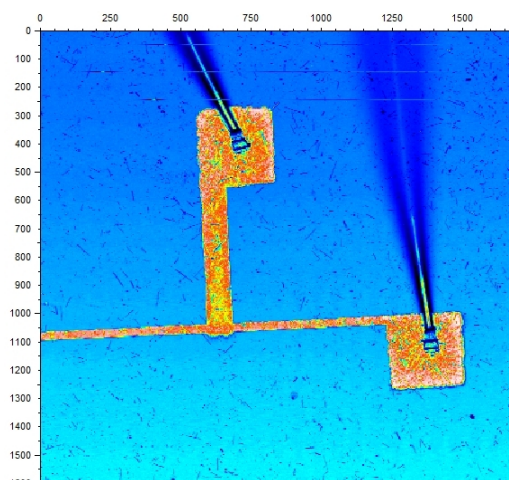


Fig.3: The intensity scan image (from Nanovea profilometer) showing a $25\mu\text{m}$ wide heater wire-bonded on the Sn-thin film (500 nm) sample..

B. SENSOR CALIBRATION

At the start of each experiment, the deposited heater/sensor wire lines on the S thin film samples were calibrated (as shown in Fig. 4). In the experiments, liquid helium low temperatures are preferred because of the longer mean free path of the heat carriers, i.e. the electrons and phonons, and hence a lucid explanation to phenomena impeding the thermal transport. At higher temperatures, these effects may be masked by Umklapp scattering. Low temperatures for this set-up are achieved by means of a cryostat (Janis Research Model: CCS-400H/204). The cryostat is capable of operating between the temperature range 10K–500K, and with special thermometry can go up to 800K. It is critical to reduce the heat load to achieve greater cooling in less time especially when working at temperatures below 100 K. The heat load is reduced by keeping the vacuum pressure on the order 10^{-3} - 10^{-5} torr while the He circulates through the cryostat. This also helps in analysis by minimizing the convection effects that would possibly introduce errors during measurement. An RV-8 rotary vane pump is used, which is capable of developing vacuum equal to 10^{-4} torr or less.

The variability in temperature at the sample mount is accomplished by a control heater at the cold finger by means of a calibrated silicon diode DT-670B sensor and a Lakeshore 332S temperature controller. The silicon diode sensor is used for both controlling and monitoring the temperature at the sample mount. The temperature controller is operated in a closed control loop mode with PID (Proportional Integral Derivative) tuning of the heater power based on the feedback signal from the silicon diode sensor.

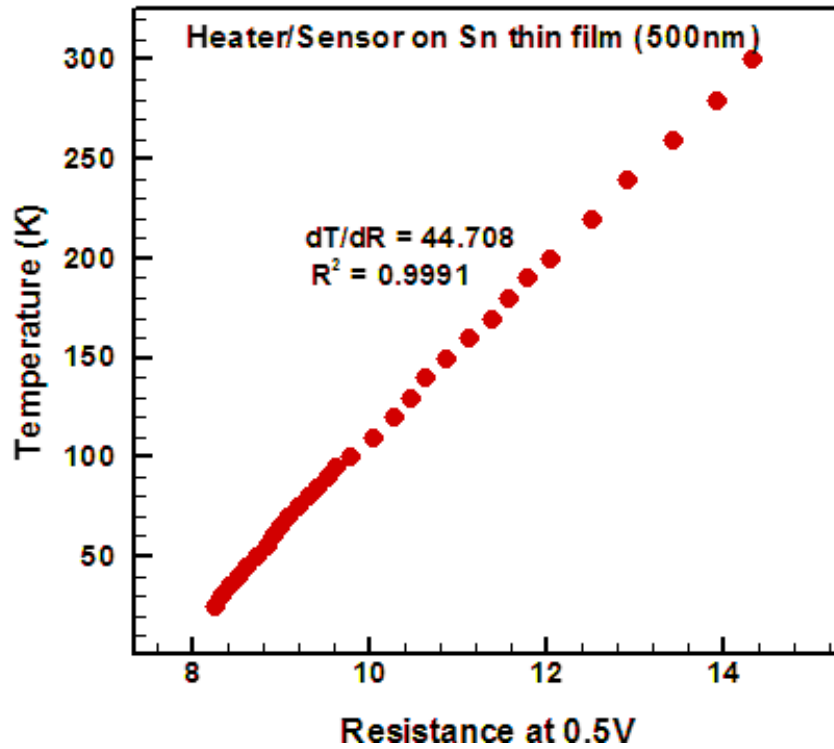


Fig.4. Resistance Vs Temperature calibration curve of a 25 μ m wide heater on 500nm Sn thin film.

For the sensor calibration, the samples were placed in the cryostat and a probe signal from the lock-in amplifier, at a relatively small amplitude voltage, is sent to avoid significant heating of the sample. At each temperature excursion, the resistance of the metal line is measured and finally plotted against the measured temperature. The slope of the measurement yields the temperature coefficient of resistance (TCR) of the deposited metal line sensor. The repeatability of the sensor was assured by the fact that the change in resistance for a unit temperature change varied within $\sim 0.1\%$ between the cooling and heating excursions for a heater with 25 μ m heater width and length 2.5mm. Following the procedure described above, the TCR of a 25 μ m width aluminum metal line on a (~ 500 nm) Sn thin film is $1/44.708$ or 0.02237 K^{-1} , with slight deviation from linearity at $\sim 60 \text{ K}$.

RESULTS AND DISCUSSION

Thermal conductivity as a function of temperature of (~ 500 nm) thick and (~ 100 nm) thin Sn films was measured using the three omega method. An insulating layer of ~ 300 nm SiO_2 was deposited using a low

temperature PECVD process. Metal heaters of aluminum were deposited on both samples through shadow mask using magnetron sputtering. The samples were finally packaged and wire bonded using ultrasonic bonder or epoxy bonding. The resistance value in mega-ohms between any two deposited heaters ensured the avoidance of pin holes and therefore reliable measurement. Metal line deposition was calibrated as a function of temperature after placing the samples in the cryostat.

The thermal conductivity in a polycrystalline metallic film has contribution from both electrons and phonons. At very low temperatures, electrons are the dominant heat carriers. A finite mean free path of the carriers is caused by the thermal vibrations of the lattice of the order of the wavelength of the sound waves in the metals. The mean free path, larger than the interatomic distances, is increased by lowering the temperature. However, the mean free path does not increase indefinitely as the electrons experience inelastic scattering by the lattice imperfections, impurities and the boundary surface. Phonon and electron mean free paths are therefore estimated for bulk tin in order to understand the thermal conductivity of (~500nm) thick and (~100nm) thin Sn films.

A. PHONON AND ELECTRON MEAN FREE PATHS IN TIN FILMS

The average phonon mean free path (Table 1) based on the kinetic theory and using the available literature values for bulk thermal conductivity, density and specific heat is ~ 65 nm. The average random velocity of phonons is taken to be the dilatation wave speed in Sn. The electron mean free path in bulk tin (Table 2), is estimated as a product of Fermi velocity and the relaxation time – the average time a heat carrier travels before it is scattered and changes its direction, since electrons at the Fermi level are generally responsible for conduction. The relaxation time in bulk tin is estimated by an empirical relation that uses experimentally determined resistivity values at 77 K, 273 K and 373 K. Additionally, Andrews [4] reported the experimentally observed electron mean free path in bulk tin as 100 nm at 79 K and 70 μm near 4 K. However, at 77 K, the electron mean free path is relatively lower ~21 nm and this is mostly due to the fact that the value of radius ratio r_s / a_0 and Fermi velocity for bulk tin is available in literature only at 298K.

Table 1. Phonon mean free path in bulk tin (at 298K)

Bulk thermal conductivity	Density	Wave Velocity	Specific heat	mean free path
y	Kg/m ³	(m/s)	(J/Kg-K)	(nm)
W/m-K				
64 ^a	7365 ^b	2261	202 ^d	55-
		2064	210 ^e	65
	5760 ^c	2557	202	60-
		2334	210	71

Elastic Modulus, $E = 32 \text{ GPa}^f$ and $\nu = 0.25$

^{a,c,d}[4] ^b[5] ^e[27] ^f[28].

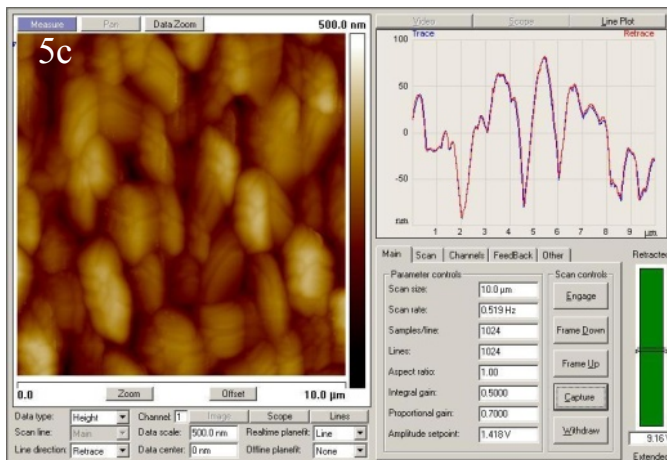
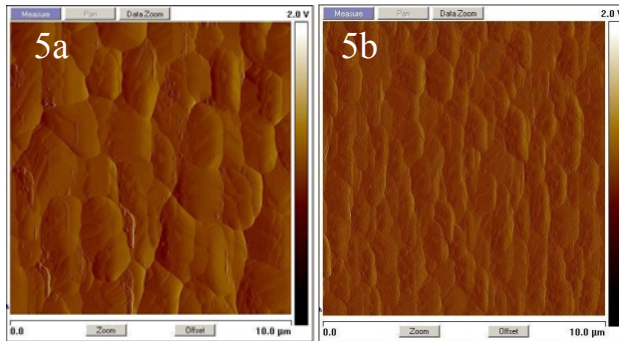
Table 2. Electron mean free path in bulk tin (at 4K, 77K, 273K, 373K)

	Temperature			373K ^b
	4K ^a	77K ^b	273K ^b	
ρ_μ		2.1	10.6	15.8
($\mu\Omega\text{-cm}$)				
τ ($\times 10^{-14}$ sec)		1.1	0.23	0.15
mean free path	70 μm	20.68	4.3	2.82
l nm		100 nm ^c		

$\tau = \left(\frac{0.22}{\rho_\mu} \right) \left(\frac{r_s}{a_0} \right)^3 10^{-14}$; $l = V_F \tau$; $r_s / a_0 = 2.22$ at 300K (for tin); $V_F = 1.9 \times 10^6 \text{ m/s}$; ^a[6] ^b[4] ^c[6] and at 79K.

B. ATOMIC FORCE MICROSCOPY OF TIN FILMS

The 500 nm and the 100 nm thick polycrystalline Sn-thin films were analyzed using atomic force microscope to estimate the grain size. A rough estimate of the size scale can also be made from the height scan of films with trace-retrace profiles of the AFM probe, as shown in Figs 5c and 5d for the 500 nm and 100 nm tin films, respectively. For the same scan area $10\mu\text{m} \times 10\mu\text{m}$ and resolution (Fig.5c, d), the grain density is higher in 100 nm Sn films compared to 500 nm Sn films. The grain size range for the 500 nm thick Sn film is 450 to 2000 nm, while the average grain size for the 100 nm thick Sn film is relatively lower, and is in the 150 – 600 nm range. Interestingly, a careful examination of AFM images (Fig.5a,b and Fig.5c,d) also reveal the presence of twin boundaries in both Sn films more often than grain boundaries. Moreover, the density of twin boundaries in 100 nm thin film is much greater than those in 500 nm. The twin boundaries are estimated to be of the order lower than 75 nm. The presence of twin boundaries has been reported more commonly for the group IV elements like silicon having fcc/diamond structure.



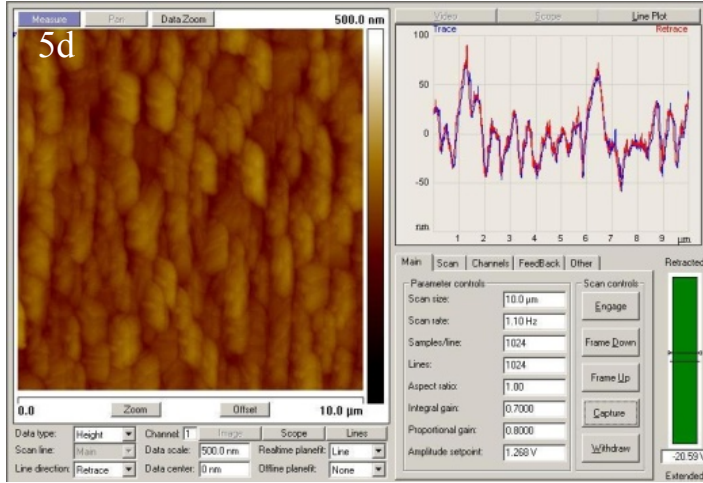


Fig. 5: AFM scan images of nanoscale Sn films: (a) Amplitude scan of 500nm Sn film; (b) Amplitude scan of 100nm Sn film; (c) Height scan of 500nm Sn film and (d) Height scan of 100nm Sn film. It is evident that 100nm Sn film has significantly higher density of grain boundaries and twin boundaries than the 500nm Sn film.

C. TEMPERATURE DEPENDENT THERMAL CONDUCTIVITY OF TIN FILMS

For the work presented in here, the thermal conductivity of the $500 \text{ nm} \pm 50 \text{ nm}$ thick films was measured from 55 K to 300 K while the thermal conductivity of $100 \text{ nm} \pm 20 \text{ nm}$ thin films was measured from 40K to 310K (Fig.6).

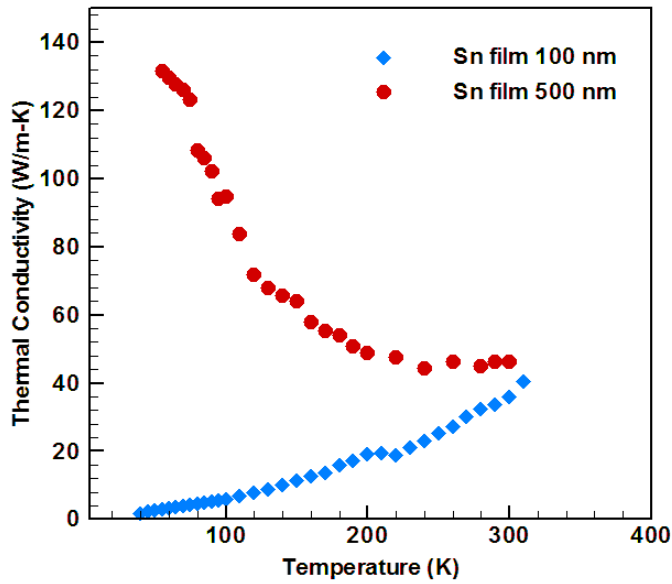


Fig.6. Thermal conductivity of a 500nm Sn film (55K-300K) and a 100nm Sn film (40 K-310 K)

The thermal conductivity of 500 nm Sn film is 46 ± 4.2 W/m-K at 300K and increases gradually as the temperature is lowered down to 100 K. As the temperature is lowered further, the thermal conductivity exhibits a sharp increase and gradually rolls off around 50 K at which the thermal conductivity is 131 ± 17 W/m-K. The electron mean free path in bulk tin at room temperature is very low (less than 20 nm) as explained earlier so it may not contribute to the heat conduction markedly. The Debye temperature of Sn is around 170 K, beyond which the specific heat reaches its Dulong-Petit limit at ~ 210 K. This indicates that the gradual increase in thermal conductivity may be solely due to the gradual increase in the mean free path of the phonons and/or electrons as the temperature is lowered while the specific heat does not change (decrease) much up to 120 K (The specific heat decreases by less than 8% of its value at 170 K). In order to understand the relative contribution of the phonons and electrons to the thermal conductivity, of Sn, the temperature at which the phonon contribution begins to exceed the electronic contribution can be estimated using the relation [4],

$$T = 0.145 \left(\frac{z\theta_D}{T_F} \right)^{1/2} \theta_D, \quad (0)$$

where θ_D is the Debye temperature, T_F is the Fermi temperature, and z is the nominal valence. This temperature for Sn can be estimated as 188.7 K. Lower than 170K, even though the specific heat decreases gradually, the electron mean free path increases at a high enough rate to contribute to heat conduction. As described previously, the electron mean free path is 100 nm around 80K and increases sharply to 70 μ m at 4 K. Therefore, the sharp increase in thermal conductivity can be attributed to the jump in electron mean free path, and gradually rolls off around 50 K at which point the electronic heat carriers experience inelastic scattering from the lateral boundary surface ($500\text{nm} \pm 50\text{nm}$), and consequently the electron mean free path decreases.

In a sharp contrast to the 500 nm thick Sn film, the thermal conductivity of the 100 nm Sn thin film is determined to decrease gradually as the temperature is lowered. The thermal conductivity of the 100 nm thin film is 36 ± 2.88 W/m-K at room temperature and decreases with temperature up to 200 K, near the Debye temperature of Sn, where it plateaus and then decreases all the way down to 40 K. The gradual decrease in thermal conductivity from room temperature can be attributed to the to the scattering of phonons by the grain boundaries and the twin boundaries as well as the inelastic scattering at the boundary surface ($100\text{nm} \pm 20\text{nm}$) since the phonon mean free path ~ 65 nm is comparable to the twin boundaries more than the grain boundaries in addition to the thin film thickness. It is to be noted that density of the twin boundaries is significantly lower and the grain size is noticeably higher in the 500 nm

thick Sn film (as evidenced by the AFM images described earlier), and therefore their presence does not markedly affect the phonon mean free path as in the case of 100 nm thin film. Moreover, the scattering effect of boundary (lateral) surface compounds the effect of scattering from the twin boundaries and grain boundaries in the case of the Sn 100 nm thin film. Consequently, as the temperature is lowered from the Debye temperature, the thermal conductivity decreases both due to lower specific heat and the effect of mean free path. At around 80 K, the electron mean free path is also long enough to experience the scattering effects due to twin boundaries and the boundary surface. In this way, the thermal conductivity in the case of the 100 nm Sn film decreases continuously due to the combined effects of scattering of majority carriers i.e. electrons, and the lower lattice specific heat as not many phonon modes are excited at temperatures very low from the Debye temperature limit .

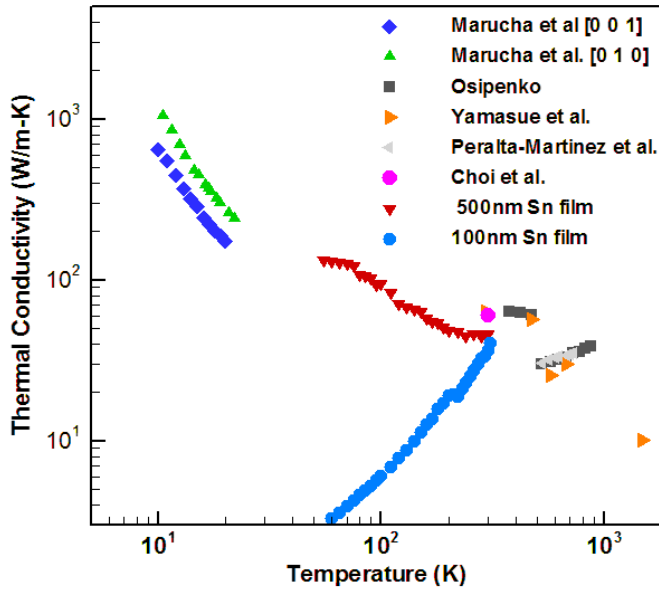


Fig.7. Complete thermal conductivity profile of Sn including thin film and bulk from 10K to 1473K. Note the phase change from solid Sn to liquid Sn occurs at 505K.

Most of the previous thermal conductivity studies [13, 14, 29, 30] performed on tin have been on bulk tin and have been conducted either at temperatures near the liquid helium temperature or at very high temperatures near its molten state i.e. phase transition from solid tin to liquid tin. To our knowledge, Choi et al (2006) [15] was first to measure thermal properties of deposited Sn thin film of thickness ~ 2000 nm. This film was deposited using the dc magnetron sputtering method at 150 W. The thermal diffusivity was measured at room temperature using a.c. calorimetry and mirage method. The measured thermal diffusivity of 2000 nm Sn film was $39 \times 10^{-6} \text{ m}^2/\text{s}$, which is equivalent to the thermal conductivity of 60.3

W/m-K, which is closer to the bulk value of 64 W/m-K at room temperature. In the present study, we report the first measurements of thermal conductivity in nanoscale Sn thin films 500nm and 100nm as a function of temperature. The current work is compared to the previous studies done on bulk tin and a complete thermal conductivity profile of Sn as a function of temperature is presented from 10 K to 1473 K for Sn thin film and bulk (Fig.7). We did not find any thermal conductivity measurements of bulk tin at intermediate temperatures from 22 K to 293 K. Note that the thermal conductivity of 500 nm thin film is lower than the expected bulk values if continued from lower to higher temperatures. The thermal conductivity of bulk tin is 1050 W/m-K in [0 1 0] direction and 650 W/m-K in [0 0 1] direction at 10 K and supposedly decreases gradually from 22 K to room temperature, after which as the temperature is increased the thermal conductivity experiences a plateau and drops precipitously around 500 K, at which it changes from solid tin to liquid tin, following which it rises a little with the increase in temperature and then again drops down to its lowest value of 10.1 W/m-K at 1473 K. The increase of the total thermal conductivity in the liquid state is explained by the fact that the increase of the kinetic energy of the electrons with increasing temperature is not upset by an increase in the scattering of the electrons by the thermal vibrations of the atoms which apparently in the liquid state is little dependent on the temperature.

D. THICKNESS DEPENDENT THERMAL CONDUCTIVITY OF TIN FILMS

The measured thermal conductivity of 500 nm Sn film at room temperature is 46 ± 4.2 W/m-K, higher than the measured thermal conductivity of 36 ± 2.88 W/m-K in 100 nm Sn film. Moreover, Choi et al.[15] reported thermal diffusivity equivalent to thermal conductivity of 60.3 W/m-K for 2000 nm thick Sn film at room temperature. This indicates that similar to other thin films, size effect is observed in the thermal conductivity of Sn at room temperature, and the thermal conductivity decreases with thickness.

The size reduction factor in metallic thin films was first explained by Fuchs-Sondheimer (FS) model [7] by solving the rigorous Boltzmann transport equation. In this model, only surface boundary scattering is considered through boundary conditions for solving the BTE. The size effect is modeled by a factor which accounts for the observed property in thin films normalized to the value in bulk as follows,

$$F_{FS} = \left[1 - \frac{3}{2k_0} (1-p) \int_1^\infty \left(\frac{1}{t^3} - \frac{1}{t^5} \right) \frac{1 - e^{-tk_0}}{1 - pe^{-tk_0}} dt \right] \quad (0)$$

where p is the specularity parameter that represents electron diffuse scattering at the boundary surface with a probability of $(1-p)$ ($p=0.5$ means partially diffuse scattering and is generally used); k_0 is the ratio of film thickness to the mean free path, and is the inverse of the Knudsen number.

A more elaborate model derived from BTE was proposed by Mayadas and Shatzkes (MS) [8], which includes the grain boundary scattering along with the surface boundary scattering in a polycrystalline metallic film. The size reduction factor based on MS theory can be expressed as follows:

$$F_{MS} = 1 - \frac{3}{2}\alpha + 3\alpha^2 - 3\alpha^3 \ln\left(1 + \frac{1}{\alpha}\right) - \frac{6(1-p)}{\pi k_0} \cdot \int_0^{\pi/2} d\phi \int_1^{\infty} \frac{\cos^2\phi}{H^2} \left(\frac{1}{t^3} - \frac{1}{t^5}\right) \frac{1 - e^{-tHk_0}}{1 - pe^{-tHk_0}} dt \quad (0)$$

where in $H(t, \phi) = 1 + d / \cos\phi \sqrt{1 - 1/t^2}$, $k_0 = d/\lambda$ and $\alpha = \lambda R / D(1-R)$, d is the film thickness and d is the average grain size, p is the specular reflection coefficient and r is the electron reflection coefficient at the grain and twin boundaries combined in this work.

Based on the above model, Qiu and Tien (QT) [31] proposed an approximate solution when the film thickness and the grain size are not too small compared with the electron mean free path, as follows

$$F_{QT} = \left[1 + \frac{3(1-p)}{8k_0} + \frac{7}{5}\alpha \right]^{-1}; \alpha < 10 \text{ and } k_0 > 0.1 \quad (0)$$

The measured thermal conductivity of 500nm and 100nm Sn films in this work at room temperature and the measured thermal conductivity of 2000nm in an earlier work by Choi et al. [15] are compared with the predictions of the Fuchs-Sonheimer (FS) model, Mayadas and Shatzkes (MS) model and the Qiu and Tien (QT) model. While the FS model is not in agreement with the measured thermal conductivity, the QT model is in agreement within 15% error, while the MS model, which includes both the grain boundary scattering of electrons as well as the inelastic scattering at the boundary surface, is in excellent agreement with the measured thermal conductivity of Sn films of thickness 100 nm, 500 nm and 2000 nm at room temperature. This indicates that indeed both the scattering phenomena are responsible for the size reduced thermal conductivity in the polycrystalline tin (Sn) thin films.

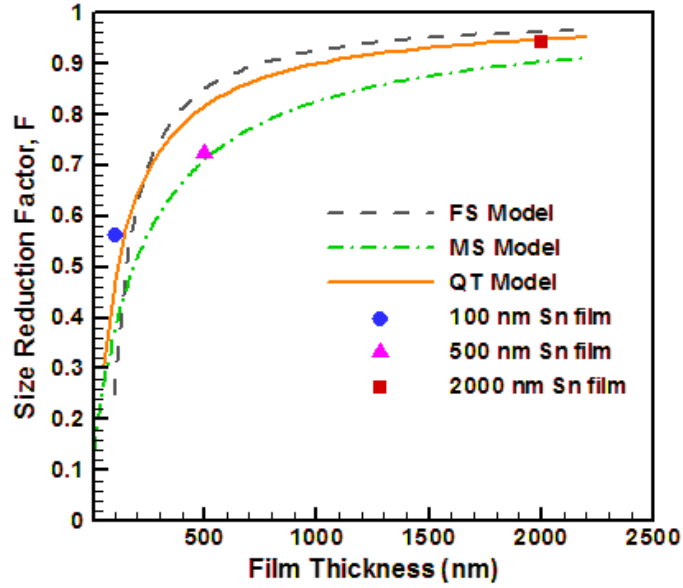


Fig. 8 Comparison of experimental thermal conductivity values of Sn films of thickness 100nm, 500nm and 2000nm with FS model, MS model and QT model. The values are normalized in the form of a size reduction factor.

SUMMARY

We report the thermal conductivity of 500nm Sn film from 55K to 300K and a 100nm Sn film from 40K to 310K. While the thermal conductivity of 500nm thick film increases as the temperature is lowered due to increase in the mean free path of the heat carriers, the thermal conductivity of 100nm decreases gradually as the temperature is lowered. The decrease in thermal conductivity is attributed to the scattering of electrons by the grain boundaries and twin boundaries as evidenced by the AFM images and further confirmed by the excellent agreement with the Mayadas-Shatzkes model and Qiu-Tien model.

REFERENCES

- [1] Cahill D.G. et al., Thermal conductivity of thin films: measurements and understanding, J. Vac. Sci. Tech A, Vol 7(3), 1989, pp1259-1266.
- [2] Kim J.H., Feldman A and Novotny D., Application of the three omega thermal conductivity measurement method to a film on a substrate of finite thickness, J. Appl. Phys., Vol 86(7), 1999, pp3959-3963.
- [3] Lee S. M. and Cahill D.G., Heat transport in thin dielectric films, J. Appl. Phys., Vol81(6), 1997, pp2590-2595.
- [4] Ashcroft N. W. and Mermin N. D., Solid State Physics, 1976, Thomson Learning Inc., USA.
- [5] Kittel C., Introduction to Solid State Physics, Seventh Edition, 1996, John Wiley & Sons, Hoboken, NJ, USA.
- [6] Andrew E R, The size variation of resistivity for mercury and tin, The Proceedgs of Phys. Soc., Vol 62(2), 1949, pp77-88.
- [7] Sonheimer E.H., Adv. Phys.1, The mean free path of electrons in metals, Vol1 (1),1952,pp1-42.
- [8] Mayadas A.F. and Shatzkes M., Phys. Rev.B., Vol 1, 1970,pp 1382
- [9] Zhang Q.G.,Cao B. Y. and Zhang X., Influence of grain-boundary scattering on the electrical and thermal conductivities of polycrystalline gold nanofilms, Phys. Rev. B., Vol.74, 2006, pp134109-1 to 5.
- [10] Sun T et. al., Dominant role of grain boundary scattering in the resistivity of nanometric Cu films, Phys. Rev. B, Vol 79, 2009, pp 041402-1 to 4.
- [11] Feng B., Li Z.and Zhang X, Effect of grain-boundary scattering on the thermal conductivity of nanocrystalline metallic films, J. Phys. D.:Appl Phys., Vol 42, 2009, pp1-5.

- [12] Feng B., Li Z. and Zhang X., Prediction of size effect on thermal conductivity of nanoscale metallic films, *Thin Solid Films*, Vol 517, 2009, pp2803-2807.
- [13] Marucha Cz., Misiorek H and Rafalowicz J, Low temperature anisotropy of thermal conductivity of tin single crystal doped with zinc, *Int. J. of Thermophysics*, Vol. 12(5), 1991, pp911-917.
- [14] Osipenko V.P., Thermal conductivity of alloys of the systems Sn-Pb and Sn-In in the solid and liquid states, Plenum Publishing, 1973, pp1570-1573.
- [15] Choi S. R., Kim D., Sung-Hoon C., Thermal diffusivity of metallic thin films: Au, Sn, Mo and Al/Ti alloy, *Inter. J. of Thermophys.*, Vol. 27(5), 2006, pp1551-1563.
- [16] Cahill D.G., Thermal conductivity measurement from 30 to 750K: the 3ω method, *Rev. Sci. Instrum.*, Vol 61(2), 1990, pp802-808.
- [17] Ahmed S., Liske R., Wunderer T, Leonhart M, Zeirvogel R, Fansler C, Grotjohn T, Asmussen J and Schuelke T, Extending the 3ω -method to the MHz range for thermal conductivity measurements of diamond thin films, *Diamond & Related Matls.*, Vol 15, 2006, pp389-393.
- [18] Hu X.J., Padilla A. A., Xu J., Fisher T.S., Goodson K.E., 3-Omega measurements of vertically oriented carbon nanotubes on silicon, *Journal of Heat Transfer*, Vol. 128, 2006, pp1109-1113.
- [19] Kihara T., Harada T. and Koshida N., Precise thermal characterization of confined nanocrystalline silicon by a 3ω -method, *Jpn. J. Appl. Phys.*, Vol.44, 2005, pp4084-4087.
- [20] Kaul P.B., Day K.A. and Abramson A R, Application of the three omega method for the thermal conductivity measurement of polyaniline, *J. Appl. Phys.* Vol 101, 2007, pp083507-1 to 7.
- [21] Borca-Tascuic T., Kumar A. R. and Chen G., Data reduction in 3-omega method for thin film thermal conductivity determination, *Rev. Sci. Instrum.*, Vol 72(4), 2001, pp2139-2147.
- [22] Olson B.W., Graham S. and Chen K., A practical extension of the 3ω method to multilayer structures, *Rev. Sci. Instrum.*, Vol.76, 2006, pp053901-1-7.

- [23] Tong T and Majumdar A, Re-examining the 3-omega technique for thin film thermal characterization, Rev. Sci. Instrum., Vol 77, 2006, pp104902-1-9.
- [24] Borca-Tascuic T., Mazumder M., Son Y., Pal S.K., Schadler L.S., Ajayan P.M., Anisotropic thermal diffusivity characterization of aligned carbon nanotube-polymer composites, J. Nanosci. Nanotechnol., Vol 7(4-5), 2007, pp1581-1588.
- [25] Abramson A.R., Kim W.C., Huxtable S.T., Yan H., Wu Y. Majumdar A., Tien C-L and Yang P., Fabrication and characterization of a nanowire/polymer-based nanocomposite for a prototype thermoelectric device, J.MEMS, Vol.13(3), 2004, pp505-511.
- [26] Cahill D.G. and Pohl R.O., Thermal conductivity of amorphous solids above the plateau, Phs. Rev.B, Vol 35(8), 1987, pp4067-4073.
- [27] Wolfram T, Lehman, G W and DeWames R E, Lattice dynamics of white tin, Phys. Rev., Vol 129(6), 1963, pp2483-2489.
- [28] Dunn B.D., Mechanical and electrical characteristics of tin whiskers with special reference to spacecraft systems, ESA Journal 1987 Vol 11/1988 Vol 12, pp1-17.
- [29] Wakeham W.A. and Peralta-Martinez M.V., Thermal conductivity of liquid tin and indium, Int. J. of Thermophysics, Vol 22 (2), 2001, pp 395-402.
- [30] Yamasue E, Susa M, Fukuyama H and Nagata K, Deviation from Weidmann-Franz law for the thermal conductivity of liquid tin and lead at elevated temperature, Int. J. of Thermophysics, Vol. 24 (3), 2003, pp.713.
- [31] Qiu T.Q. and Tien C.L., Journal of Heat Transfer, Vol 115, 1993, pp842.

Application of elastic wave dispersion relations to estimate thermal properties of nanoscale wires and tubes of varying wall thickness and diameter

Michael F P Bifano, Pankaj B Kaul and Vikas Prakash¹

Department of Mechanical and Aerospace Engineering, Case Western Reserve University, Cleveland, OH 44106, USA

E-mail: vikas.prakash@case.edu

Received 23 March 2010, in final form 23 April 2010

Published 17 May 2010

Online at stacks.iop.org/Nano/21/235704

Abstract

This paper reports dependency of specific heat and ballistic thermal conductance on cross-sectional geometry (tube versus rod) and size (i.e., diameter and wall thickness), in free-standing isotropic non-metallic crystalline nanostructures. The analysis is performed using dispersion relations found by numerically solving the Pochhammer-Chree frequency equation for a tube. Estimates for the allowable phonon dispersion relations within the crystal lattice are obtained by modifying the elastic acoustic dispersion relations so as to account for the discrete nature of the material's crystal lattice. These phonon dispersion relations are then used to evaluate the specific heat and ballistic thermal conductance in the nanostructures as a function of the nanostructure geometry and size. Two major results are revealed in the analysis: increasing the outer diameter of a nanotube while keeping the ratio of the inner to outer tube radius (γ) fixed increases the total number of available phonon modes capable of thermal population. Secondly, decreasing the wall thickness of a nanotube (i.e., increasing γ) while keeping its outer diameter fixed, results in a drastic decrease in the available phonon mode density and a reduction in the frequency of the longitudinal and flexural acoustic phonon modes in the nanostructure. The dependency of the nanostructure's specific heat on temperature indicates 1D, 2D, and 3D geometric phonon confinement regimes. Transition temperatures for each phonon confinement regime are shown to depend on both the nanostructure's wall thickness and outer radius. Compared to nanowires ($\gamma = 0$), the frequency reduction of acoustic phonon modes in thinner walled nanotubes ($\gamma = 0.96$) is shown to elevate the ballistic thermal conductance of the thin-walled nanotube between 0.2 and 150 K. At 20 K, the ballistic thermal conductance of the thin-walled nanotube ($\gamma = 0.96$) becomes 300% greater than that of a solid nanowire. For temperatures above 150 K, the trend in ballistic thermal conductance inverts. The greater number of phonon modes in nanostructures with increased outer diameter and wall thickness is shown to have a larger contribution to ballistic thermal conductance when compared to the increased contribution from the frequency reduction of acoustic phonon modes in thinner walled nanotubes.

(Some figures in this article are in colour only in the electronic version)

1. Introduction

Specific heat and thermal conductivity in bulk crystalline solids are intrinsic properties, which are independent of the

crystal dimensions. This is understood to be true even at low temperatures when phonon wavelengths are large. Specific heat and thermal conductivity, however, become dependent on the geometry of the structure when the size of the structure interferes with the existence and propagation of energy

¹ Author to whom any correspondence should be addressed.

carriers, predominantly the dominant phonon wavelength in non-metallic materials [1–4].

The mechanisms governing the thermal transport in cylindrical structures are of particular interest in the design and development of more efficient thermal management/heat dissipation technologies [2, 3] and in the design and development of next-generation thermoelectric materials requiring low thermal conductivities combined with high electrical conductance [5]. Undoubtedly, both applications are expected to benefit from further mechanistic studies of thermal transport through cylindrical nanostructures.

Literature is ripe with various methods of thermal conductivity estimates in individual nanowires [3, 4, 6–8], as well as carbon nanotubes [1, 9–12]. However, to date, a direct comprehensive comparison of the specific heat capacity and ballistic thermal conductance in nanowires with those in nanotubes of varying geometry (and dimensions) does not exist. For example, in the past, the thermal properties of carbon nanotubes (CNTs) have been estimated from phonon dispersion relations calculated from spring constant and bond angle models [13]. While such atomistic studies have adequately accounted for diameter dependencies of the CNTs, these models become increasingly complex with the addition of atoms to the wall thickness; the use of 3D cylindrical continuum wave models to represent phonon dispersion is an attractive alternative to investigating the effects of geometry and size on specific heat and ballistic thermal conductance in nanowires and nanotubes. These phonon dispersion relationships provide insights into the allowable phonon frequencies capable of thermal population for a given nanostructure, and are an invaluable comparative tool for understanding the intrinsic differences between the thermal properties of nanoscale wires and tubes.

In the present study, variations in available phonon mode densities as a function of the nanostructure geometry and size are explored using acoustic dispersion relations derived from a continuum-level 3D elastic wave model. Estimates for the allowable phonon dispersion relations are obtained by modifying the elastic dispersion relations so as to account for the discrete nature of the material's crystal lattice [14]. These phonon dispersion relations are then used to estimate the specific heat and ballistic thermal conductance of the nanostructures. Geometric effects on wave dispersion in cylindrical [15] and rectangular nanowires [16] have previously been studied using continuum-level elastic models. The consequences of these models on phonon dispersion and, therefore, specific heat and ballistic thermal conductance has only been explored in the case of cylindrical nanowires [14]. But, to date, the effects of phonon dispersion modification on specific heat and thermal conductance due to nanotube wall thickness and outer diameter have not been investigated.

2. Modeling

2.1. Elastic dispersion relations as a function of the nanostructure geometry

Dispersion relations are found by numerically solving the Pochhammer-Chree frequency equation for an infinitely long

tube. To derive the Pochhammer-Chree frequency equation from the complete 3D cylindrical elastic wave model, we apply the method outlined by Graff [17]. The frequency equation is derived for the nanotube using the assumption of stress-free boundary conditions on both inner and outer free surfaces. However, it must be noted that the stress-free boundary conditions are chosen as a first approximation to analyze the effects of nanoscale geometry on phonon confinement and its effects on specific heat and ballistic thermal conductance. In some recent research [18–20], it has been reported that phonon dispersion is altered by the presence of surface stress and/or residual stress fields within the nanostructures. In this regard, the existence of a positive hoop stress due to bond order loss of surface atoms in solid nanowires is likely to decrease the frequency of the acoustic phonon modes and increase the average phonon group velocity [19]. As will be later shown, these effects are likely to elevate the specific heat as well as the ballistic thermal conductance of the nanostructures. Nonetheless, the role of cross-sectional geometry alone on specific heat and ballistic thermal conductance has not been investigated for nanotubes of varying wall thickness and diameters, and warrants a systematic investigation. For this reason, in the present study, stress-free boundary conditions are chosen to simplify the analysis and at the same time isolate the variables in question.

Due to the complexity of the applied method, it is advantageous to summarize the key points of the derivation. Using a Helmholtz decomposition, the wave displacement field of a cylindrical structure can be described using a scalar potential, ϕ , and a vector potential, \mathbf{H} , such that

$$\mathbf{u} = \nabla\phi + \nabla \times \mathbf{H}. \quad (1)$$

The potentials ϕ and \mathbf{H} satisfy the scalar and vector wave equations,

$$\nabla^2\phi = \frac{1}{c_1^2} \frac{\partial^2\phi}{\partial t^2} \quad (2)$$

$$\nabla^2\mathbf{H} = \frac{1}{c_2^2} \frac{\partial^2\mathbf{H}}{\partial t^2} \quad (3)$$

where c_1 is the longitudinal (compressive) wave velocity and c_2 is the transverse (shear) wave velocity, both dependent on the elastic properties of the material

$$c_1 = \sqrt{\frac{E(1-\nu)}{\rho(1+\nu)(1-2\nu)}} \quad (4)$$

$$c_2 = \sqrt{\frac{E}{2\rho(1+\nu)}}. \quad (5)$$

Equations (4) and (5) are formulated in terms the density ρ , Young's modulus E , and Poisson's ratio, ν . For the purpose of this study, $E = 1.3$ TPa (reflecting the value of Young's modulus reported for a single-walled CNT in [21]), $\nu = 0.27$ and $\rho = 2260$ kg m⁻³, are used in all calculations.

The scalar components of the displacement vector \mathbf{u} , are described in the cylindrical coordinate system r , θ , and z , and are given by

$$u_r = \frac{\partial\phi}{\partial r} + \frac{1}{r} \frac{\partial H_z}{\partial \theta} - \frac{\partial H_\theta}{\partial z} \quad (6)$$

$$u_\theta = \frac{1}{r} \frac{\partial \Phi}{\partial \theta} + \frac{\partial H_r}{\partial z} - \frac{\partial H_z}{\partial r} \quad (7)$$

$$u_z = \frac{\partial \Phi}{\partial z} + \frac{1}{r} \frac{\partial}{\partial r} (r H_\theta) - \frac{1}{r} \frac{\partial H_r}{\partial \theta}. \quad (8)$$

The potentials given in equation (1) have general solutions,

$$\Phi = f(r) \cos n\theta \cos(\omega t + kz) \quad (9)$$

$$H_r = h_r(r) \sin n\theta \sin(\omega t + kz) \quad (10)$$

$$H_\theta = h_\theta(r) \cos n\theta \sin(\omega t + kz) \quad (11)$$

$$H_z = h_z(r) \cos n\theta \cos(\omega t + kz) \quad (12)$$

where the functions $f(r)$, $h_r(r)$, $h_\theta(r)$, and $h_z(r)$ involve solutions to the Bessel equation, such that

$$f = A Z_n(|\alpha|r) + B W_n(|\alpha|r) \quad (13)$$

$$h_z = A_3 Z_n(|\beta|r) + B_3 W_n(|\beta|r) \quad (14)$$

$$2h_1 = h_r - h_\theta = 2A_1 Z_{n+1}(|\beta|r) + 2B_1 W_{n+1}(|\beta|r) \quad (15)$$

$$2h_2 = h_r + h_\theta = 2A_2 Z_{n-1}(|\beta|r) + 2B_2 W_{n-1}(|\beta|r). \quad (16)$$

In equations (13)–(16), A , B , A_1 , B_1 , A_2 , B_2 , A_3 , and B_3 are unknown constants, and Z_n and W_n represent n th order ordinary Bessel and modified Bessel functions, respectively. The specifics of Bessel function choice are given in appendix A. α and β contain the frequency ω , and the wavenumber k , and are given by

$$\alpha = \sqrt{\omega^2/c_1^2 - k^2} \quad (17)$$

$$\beta = \sqrt{\omega^2/c_2^2 - k^2}. \quad (18)$$

There are four functions f , h_1 , h_2 , h_3 containing the eight unknown constants, and only six boundary conditions that can be applied. The property of gauge invariance [17] allows for any one of h_1 , h_2 , h_3 to be equated to zero without loss of generality. Because stress-free boundary conditions are applied to the inner and outer surfaces of the tube, stress field equations are required to determine all the remaining unknown constants.

The stress fields are obtained via the elastic constitutive relation (Hooke's law),

$$\sigma_{ij} = \lambda e_{kk} \delta_{ij} + 2\mu e_{ij} \quad (19)$$

where Lamé's constant λ , and the shear modulus μ , are functions of E , and ν . The components of the strain tensor, e_{ij} , (on the right-side of equation (19)), are given by

$$e_{rr} = \frac{\partial u_r}{\partial r} \quad (20)$$

$$e_{\theta\theta} = \frac{1}{r} \frac{\partial u_\theta}{\partial \theta} + \frac{u_r}{r} \quad (21)$$

$$e_{zz} = \frac{\partial u_z}{\partial z} \quad (22)$$

$$e_{r\theta} = \frac{1}{2} \left(\frac{1}{r} \frac{\partial u_r}{\partial \theta} + \frac{\partial u_\theta}{\partial r} - \frac{u_\theta}{r} \right) \quad (23)$$

$$e_{rz} = \frac{1}{2} \left(\frac{\partial u_z}{\partial r} + \frac{\partial u_r}{\partial z} \right) \quad (24)$$

$$e_{\theta z} = \frac{1}{2} \left(\frac{\partial u_\theta}{\partial z} + \frac{1}{r} \frac{\partial u_z}{\partial \theta} \right) \quad (25)$$

and are determined by differentiation of equations (6)–(8).

Substituting equations (20)–(25) into (19) yields the stress field equations. The stresses σ_{rr} , σ_{rz} , $\sigma_{r\theta}$ are of the only concern and together contain the six unknown constants, A_1 , B_1 , A_2 , B_2 , A_3 , B_3 , where A and B have been eliminated by the application of gauge invariance [17]. The tractions at the inner, $r = R_i$, and the outer, $r = R_o$, boundaries are zero and therefore the stress components σ_{rr} , σ_{rz} , $\sigma_{r\theta}$ at the inner and outer boundaries are set to zero.

The Pochhammer-Chree frequency equation is derived by solving a matrix determinant. The elements of the matrix determinant are the coefficients of the six unknown constants (A_1 , B_1 , A_2 , B_2 , A_3 , B_3) in each of the six stress field equations. Because the unknown constants have nontrivial solutions, setting the six-by-six matrix determinant to zero satisfies the boundary conditions. Solutions to the frequency equation are values of k and ω that satisfy the six-by-six determinant

$$|c_{ij}| = 0 \quad i, j = 1 \cdots 6. \quad (26)$$

Components of equation (26) are given in appendix A.

Equation (26) is solved using a bisection algorithm written within MATLAB[®]. An infinite number of allowable frequency solutions of the type $\omega(n, m) = f(k)$ are obtained. The (n, m) solutions are the allowable harmonics or modes of vibration of the structure. Every azimuthal mode number, n , has an infinite number of corresponding radial solutions, m . A total of 50 radial modes, m , are first calculated for each azimuthal mode number, n , for $n = 0$ –50. The class of longitudinal and torsional modes are formed for values of $n = 0$. Flexural modes are represented by values of $n \geq 1$. Note that all flexural modes must be considered twice due to x and y flexural wave polarizations. Normalized frequencies ($\omega R_o/c_o$) are calculated for normalized wavenumber ($k R_o$) values from $k R_o = 0$ to $k R_o = (\pi R_o/a)$, where $a = 1.7835 \text{ \AA}$. This choice of the effective lattice constant, a , will be discussed in more detail in section 2.2.

Figure 1 compares the $n = 0$ and 1 dispersion curves calculated via equation (26), for a solid rod ($\gamma = 0$), a thick-walled tube ($\gamma = 0.5$), and a very thin-walled tube ($\gamma = 0.96$). Examination of figure 1 reveals the dependency of the allowable wave modes on the cross section geometry. First, a significant decrease in density of the allowable modes of vibration is observed with decreasing tube wall thickness (increasing γ). Secondly, as the outer radius of the tube is increased the density of the available modes of vibrations is observed to increase for all wall thicknesses. Lastly, of the four acoustic modes ($\omega \rightarrow 0$ as $k \rightarrow 0$), one torsional mode (TA) (figures 1(a), (c) and (e) long dashed), one longitudinal mode (LA) (figures 1(a), (c) and (e) short dashed), and one doubly degenerate flexural mode (FA) (figures 1(b), (d) and (f) short dashed), the normalized frequencies and group velocities

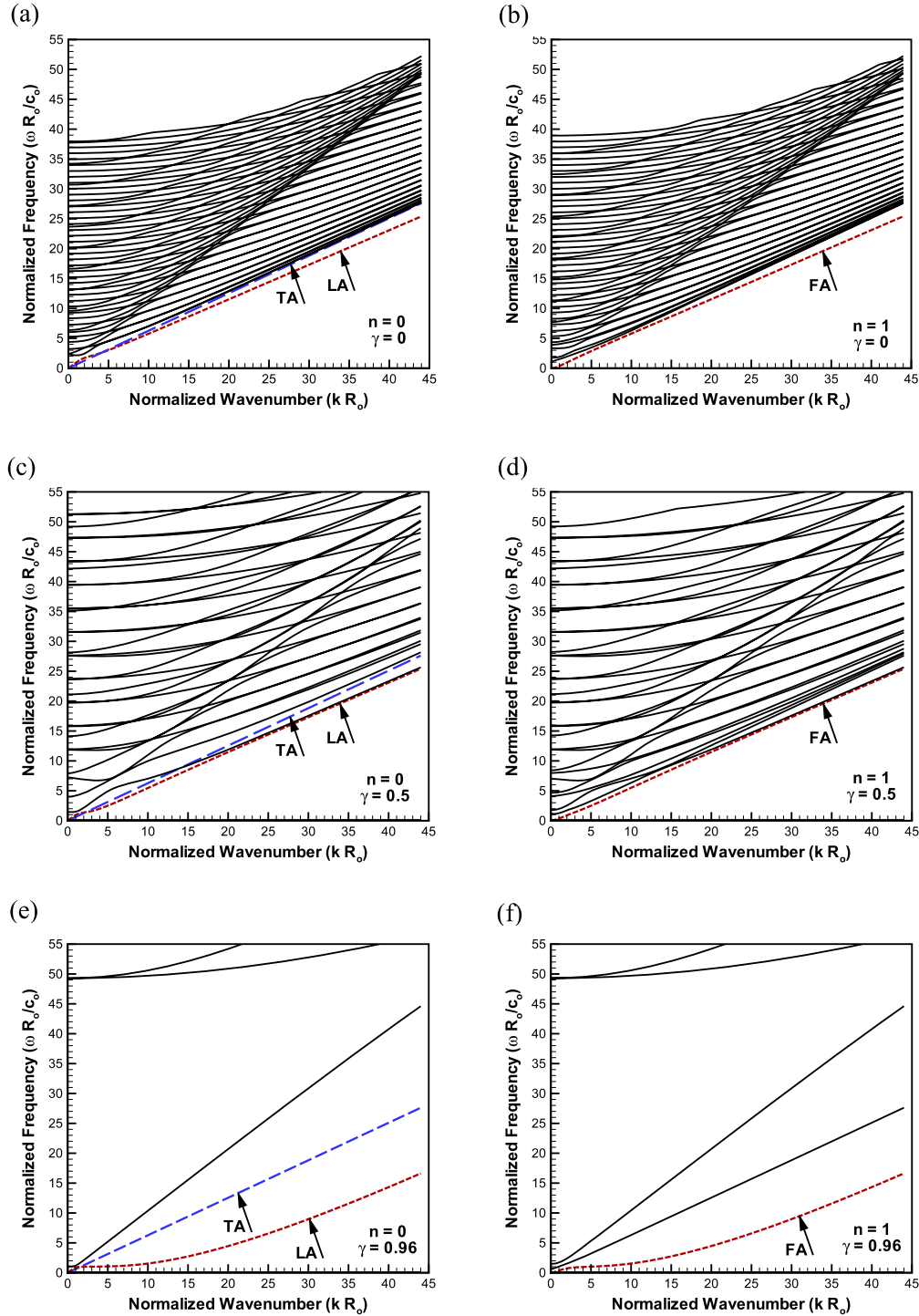


Figure 1. Elastic dispersion relations calculated by solving equation (26): (a) torsional and longitudinal modes ($n = 0$) of a solid wire ($\gamma = 0$); (b) flexural modes ($n = 1$) of a solid wire ($\gamma = 0$); (c) torsional and longitudinal modes ($n = 0$) of a thick-walled tube ($\gamma = 0.5$); (d) flexural modes ($n = 1$) of a thick-walled tube ($\gamma = 0.5$); (e) torsional and longitudinal modes ($n = 0$) of a thin-walled tube ($\gamma = 0.96$); (f) flexural modes ($n = 1$) of a thin-walled tube ($\gamma = 0.96$). The acoustic modes ($\omega \rightarrow 0$ as $k \rightarrow 0$) are marked by their respective dashed lines. The normalized frequency of the longitudinal acoustic (LA) mode and the flexural acoustic (FA) mode decrease with decreasing wall thickness (increasing γ). The slope of the torsional acoustic (TA) mode remains constant. The density of allowable mode vibrations increase with both the increase in wall thickness (decrease in γ) and the increase in outer radius, R_0 .

corresponding to the LA and FA modes are reduced with a decrease in the tube wall thickness (increasing γ).

Figure 2 is a schematic representation of low frequency TA, LA, and FA displacements of a nanotube having a wall

thickness characterized by $\gamma = 0.96$ and $R_0 = 2.5$ nm. The displacement fields are calculated at a frequency of 1 THz, corresponding to a normalized frequency of ~ 0.1 . The amplitudes are normalized for a qualitative comparison.

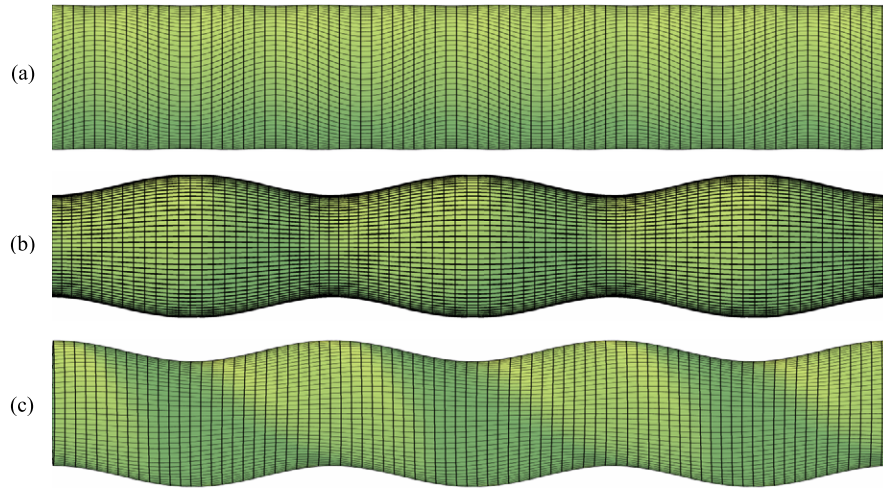


Figure 2. Schematic representation of acoustic mode displacements in $\gamma = 0.96$, 5 nm outer diameter nanotube. (a) Torsional acoustic mode (TA); (b) longitudinal acoustic mode (LA) and (c) doubly degenerate flexural acoustic modes (FA).

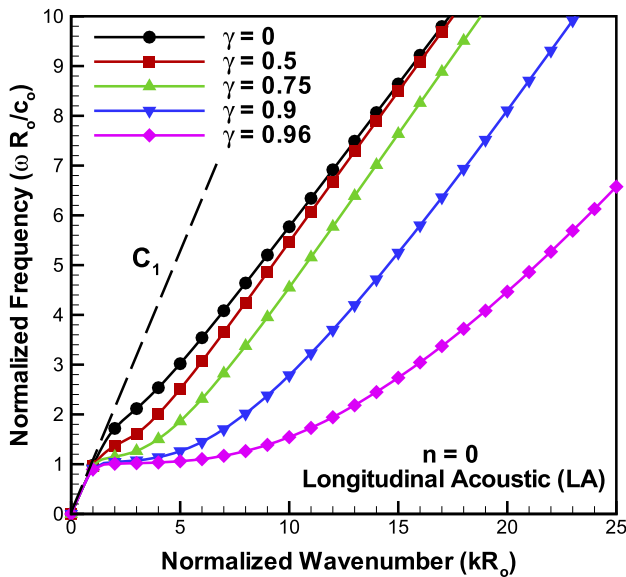


Figure 3. Comparison of $n = 0$ longitudinal acoustic (LA) mode dispersion of five structures having a varying ratio of inner to outer diameter, γ . $\gamma = 0$ is the solid wire, while $\gamma = 0.96$ represents a thin-walled tube. The non-dispersive $\omega = c_1 k$ behavior is shown (dashed line) as a reference.

Figures 3 and 4, respectively, show the variation in the acoustic LA and FA modes as a function of the tube wall thickness. From figure 3 we can infer that all nanostructure geometries studied in the present investigation show a nearly non-dispersive LA mode (similar to $\omega = c_1 k$) for $\omega R_o/c_o < 1.8$ and $k R_o < 1$. These non-dispersive waves exist only for $k R_o < 1$ and are confined to the structure's longitudinal z -axis, since the group velocity of these modes are that of a P-wave, c_1 (dashed line). As the wavenumber k is increased, for a fixed outer radius of the nanostructures, the thin-walled tube ($\gamma = 0.96$) shows the maximum deviation from the c_1 velocity, followed by structures with increasing wall thickness. This behavior is as expected since the

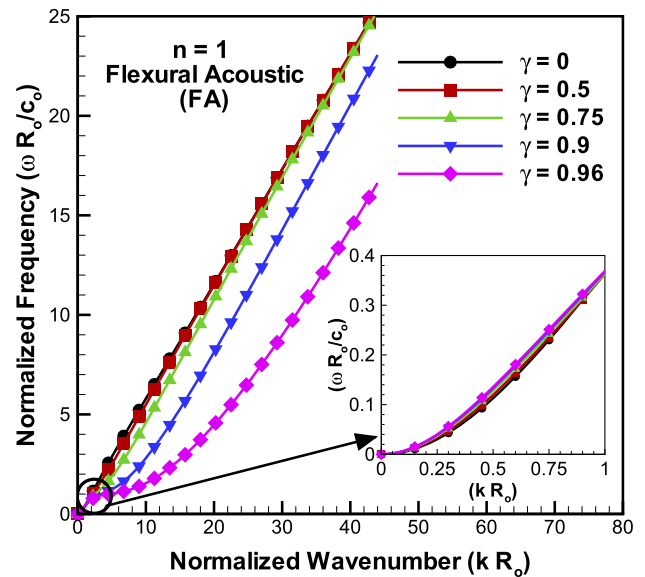


Figure 4. Comparison of $n = 1$ flexural acoustic (FA) mode dispersion behavior of five structures having a varying ratio of inner to outer diameter, γ . $\gamma = 0$ is the solid wire while $\gamma = 0.96$ represents a thin-walled tube. The inset shows quadratic dispersion behavior for $k R_o < 1$. The quadratic low frequency dispersion behavior is nearly identical to all tube geometries and responsible for the $T^{0.5}$ specific heat dependence at low temperatures [14].

thinnest wall tube has the greatest average circumference, allowing preferential circumferential mode population as the wavelength is decreased (wavenumbers increase). In summary, the LA mode's transition from non-dispersive to dispersive wave behavior, seen in figure 3 at $k R_o \sim 1$, is indicative of a transition from purely longitudinal wave propagation down the axis of the structure to a coupling of longitudinal waves and azimuthal waves around the structure's circumference.

The FA mode exhibits a quadratic behavior, $\omega \propto k^2$, for each structure for $k R_o < 1$ (figure 4). This behavior is in agreement with [21–23], and is unlike the linear flexural

dispersion relationship obtained from the graphene zone-folding method for thin-walled tubes [13]. Furthermore, both figures 3 and 4 suggest that at low wavenumbers, all acoustic modes are nearly independent of cross-sectional geometry. This behavior is to be expected, since, at lower frequencies the waves are primarily confined to the longitudinal z -axis. For $kR_o > 1$, the frequency of the LA and FA modes decrease with a reduction in wall thickness as wavenumbers increase past the point for which the wavelengths solely occupy the axial dimension of the tube or rod and transition to a coupled longitudinal and circumferential combined mode (figures 3 and 4).

2.2. Approximating the phonon dispersion relationship

The wavenumbers in the elastic dispersion relation represent waves that vary continuously along the tube axis and are not representative of a periodic Brillouin zone. To better utilize the elastic dispersion model as an approximation for phonon dispersion, the continuum-based frequency spectrum must be modified to account for the discreteness of the crystalline lattice and the continuity of the 3D continuum wave model.

The material used in the description of all nanostructures in this study is assumed to have a diamond lattice. However, it is not possible to choose a conventional unit cell of an interpenetrating face-centered cubic lattice structure so that the unit cell contains one atom per basis [24]. Similar to the work described in [25], an effective lattice constant, a , is employed by dividing the conventional unit cell lattice constant of the diamond lattice by one-half. This approximation provides an effective simple cubic lattice with approximately one atom per basis and is appropriate given the perspective of this investigation.

A Born–von-Karman boundary condition is employed to account for the lack of periodicity in the elastic dispersion relation by forcing the group velocity of the lowest frequency (n, m) modes to zero at the far right of the dispersion relation, $k_{\max} = \pi/a$. To apply the Born–von-Karman boundary condition, every (n, m) dispersion mode is multiplied by [14],

$$\sin(ka/2)/(ka/2). \quad (27)$$

Further discussion regarding equation (27) is provided in appendix B. Figure 5 shows a comparison between a typical elastic dispersion relation (solid lines) derived from the continuum wave model, and the phonon dispersion approximation (dashed lines) obtained by multiplying every (n, m) mode by equation (27). The maximum wavenumber represents the edge of the first Brillouin zone of a symmetric simple cubic lattice. This modification creates an effective standing wave within each lattice cell for the lowest frequency modes, thus allowing the elastic dispersion relations to better approximate the phonon dispersion relation.

The total number of required phonon modes is approximately equal to three times the total number of available lattice points in the cross-sectional area of the tube. The factor of three represents the three available degrees of freedom

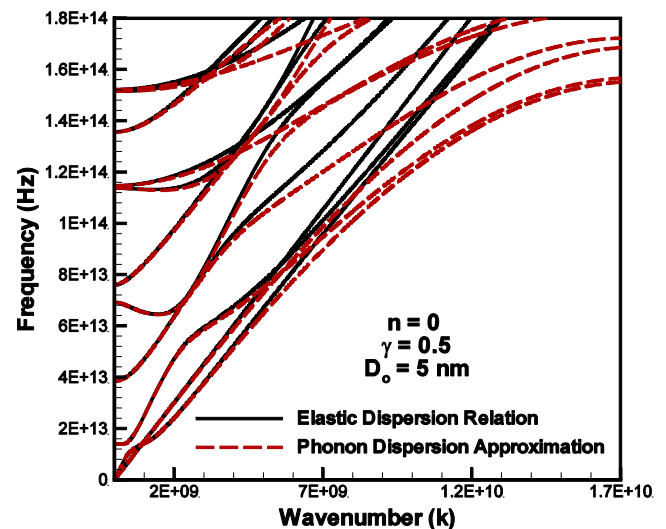


Figure 5. Torsional and longitudinal elastic dispersion (solid lines), and the torsional and longitudinal phonon dispersion relations (dashed lines) are shown for the case of a thick-walled nanotube ($\gamma = 0.5$) having a 5 nm outer diameter. An approximation of the phonon dispersion relation is acquired by modifying the elastic dispersion relation using equation (27). The modification of the elastic dispersion relation is performed for each value of γ . Group velocities of the low frequency modes approach zero at maximum wavenumber. The elastic dispersion relation and the newly acquired phonon dispersion approximations are nearly identical at low frequencies, which according to equation (31) are of greatest contribution throughout the temperature domain of 0.1–600 K.

for each mechanical oscillator. Because the system is approximated as a simple cubic lattice, the total number of (n, m) modes available for thermal population in the cross section of the structure should be three times the number of atoms in the cross-sectional plane. Estimation of the exact number and arrangement of atoms is avoided by limiting the investigation to a temperature domain below 600 K. Since the purpose of this investigation is to examine phonon confinement effects, the maximum value of specific heat is not of interest, and therefore, knowledge of an exact number of phonon modes is not essential. An exact number of phonon modes would be required if complete phonon mode saturation were to take place; this would occur at the maximum value of specific heat. As indicated in figure 6, mode saturation would occur at temperatures greater than 600 K, which is well past the point where specific heat values for each tube geometry would likely converge. Subsequent to the marked $C \propto T^3$ behavior, the short wavelength phonons are unconfined by the dimensions of the structure, and, therefore, temperatures exceeding 600 K are not of interest.

When calculating internal energy and specific heat it is important to have an ample set of phonon modes available for thermal population. As temperature increases the internal energy of the system activates a greater number of phonon modes that are higher in wavenumber and thus frequency. During the present calculations the upper bound of (n, m) is chosen such that the internal energy and thus the specific heat converges to a maximum at the temperature of interest. The

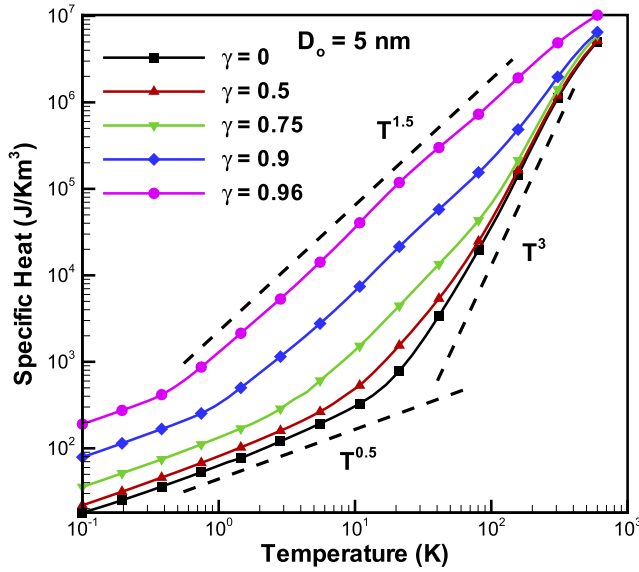


Figure 6. Specific heat versus temperature for five inner to outer tube radii ratios, γ . Each cylindrical geometry has a 5 nm outer diameter. As tube thickness increases, specific heat is shown to collapse onto that of a solid nanowire. The dashed lines are representative of $T^{0.5}$ '1D', $T^{1.5}$ '2D', and T^3 '3D' phonon confinement behavior.

convergence indicates that a proper number of phonon modes have been accounted for in the calculations.

2.3. Internal energy

The volumetric internal energy in the z -direction is calculated by summing the contributions from every (n, m) mode pair.

$$U(T) = \frac{1}{A_t} \sum_{(n,m)} \int \frac{d\vec{k}}{2\pi} \frac{\hbar\omega_{(n,m)}}{\exp(\beta\hbar\omega_{(n,m)}) - 1} = \frac{1}{A_t} \sum_{(n,m)} \int_0^{\pi/a} \frac{d\vec{k}}{\pi} \frac{\hbar\omega_{(n,m)}}{\exp(\beta\hbar\omega_{(n,m)}) - 1} \quad (28)$$

where A_t is the cross-sectional area of the nanotube wall thickness, and $\beta = 1/k_B T$.

The upper bound on the integral in equation (28), π/a , is the Debye wave vector cutoff describing the outer edge of the first Brillouin zone in the k -space. As also inferred from the denominator of the integrand, a surplus of modes beyond the maximum required (n, m) have negligible contribution since the higher order modes are of higher frequency. Therefore, as long as the internal energy converges to a maximum value, a sufficient number of (n, m) modes have been considered.

2.4. Specific heat and ballistic thermal conductance

Differentiating equation (28) with respect to temperature leads to the expression for specific heat capacity per unit volume,

$$C(T) = \frac{1}{A_t} \frac{d}{dT} \sum_{(n,m)} \int \frac{d\vec{k}}{2\pi} \frac{\hbar\omega_{(n,m)}}{\exp(\beta\hbar\omega_{(n,m)}) - 1} = \frac{1}{A_t k_B T^2} \sum_n \sum_m \int_0^{\pi/a} \frac{d\vec{k}}{\pi} \frac{\hbar^2 \omega_{(n,m)}^2 e^{\beta\hbar\omega_{(n,m)}}}{(\exp(\beta\hbar\omega_{(n,m)}) - 1)^2}. \quad (29)$$

Similar to equation (28), the above expression does not require any externally imposed mode cut-offs due to the temperature dependent nature of the denominator.

The ballistic conductance in the z -direction is the sum of contributions from each (n, m) mode,

$$g(T) = \sum_n \sum_m \frac{A_t}{2} C_{(n,m)} v_{(n,m)} = \frac{1}{2} \frac{1}{k_B T^2} \sum_n \sum_m \int_0^{\pi/a} \frac{d\vec{k}}{\pi} \frac{\hbar^2 \omega_{(n,m)}^2 e^{\beta\hbar\omega_{(n,m)}}}{(\exp(\beta\hbar\omega_{(n,m)}) - 1)^2} v_{(n,m)}. \quad (30)$$

In equation (30), $v_{(n,m)}$ is the group velocity, the slope of the (n, m) dispersion band, at wavenumber k .

When $\hbar\omega/k_B T \ll 1$, all three integrands in equations (28)–(30) have appreciable contributions to the value of their respective integrals. Therefore, phonon frequencies satisfying

$$\omega \ll k_B T / \hbar \quad (31)$$

are the most significant contributors to the internal energy, specific heat, and the ballistic thermal conductance [26]. Most importantly, equation (31) provides the criteria for thermal mode activation.

Equations (29)–(31) reveal that specific heat and ballistic thermal conductance are primarily controlled by three phonon mode characteristics within a typical nanostructure. First, of all the allowable phonon modes, the lowest frequency phonon modes are the first to thermally populate with increasing temperature. Secondly, lower frequency phonon modes are the greatest contributors to internal energy, specific heat, and the ballistic thermal conductance. Lastly, the total thermal contribution is the sum of all the thermally activated phonons at a particular temperature.

3. Results and discussion

Qualitatively, geometric phonon confinement effects can be explained in terms of the dominant phonon wavelength of the system [1]. The dependence of the dominant phonon wavelength, λ_d on temperature is given by [26],

$$\lambda_d \approx 2\pi \hbar c_{avg} / k_B T \quad (32)$$

where c_{avg} is an averaged phonon group velocity, which can be calculated from any one or group of (n, m) modes for any range wavenumbers from 0 to π/a . Decreasing the temperature of the system drives the dominant phonon wavelength of the system higher. Lower temperatures will eventually cause the wall thickness and circumferential dimensions of the nanotube to become 'frozen-out' as the dominant phonon wavelength exceeds the respective characteristic length of the dimension. Similar to the elastic waves, larger phonon wavelengths (smaller wavenumbers) are confined to the length of the tube, giving rise to the 1D regime. As temperatures increase, the dominant phonon wavelength becomes smaller and begins to occupy the next smaller dimensions of the system, starting with the circumferential length (2D regime), and followed by the radial dimensions,

i.e., the wall thickness or the diameter. Phonon population of the wall thickness marks the 3D regime. Once this occurs, with regards to phonon confinement, the structure is thermally analogous to its bulk material.

3.1. Tube thickness variation

Figure 6 shows the specific heat capacities (per unit volume) for five cylindrical geometries. As expected, with an increase in the wall thickness the thermal behavior converges onto that of a solid nanowire. Evidence of 1D \rightarrow 2D \rightarrow 3D transitional behavior is apparent with increasing temperature (figure 6).

In the low temperature limit, according to equation (31), acoustic phonon modes contribute significantly to equations (29) and (30). In the case of nanowires, the acoustic dispersion relations have been approximated with analytic forms for LA ($\omega = c_1 k$), TA ($\omega = c_2 k$), and FA ($\omega = c_0 D k^2$) modes, where $c_0 = \sqrt{E/\rho}$ and D is the diameter of the nanowire [14]. Contributions to specific heat from each aforementioned phonon mode can be independently found using equation (29). At low temperatures, the LA and TA phonon mode contributions to specific heat exhibit a $C \propto T$ behavior, while the FA phonon mode contribution shows a $C \propto T^{0.5}$ behavior [14]. In this study, FA phonon mode dominance in the low temperature limit is present for all geometries and shown by a $C \propto T^{0.5}$ behavior (figure 6). FA mode dominance is justified since the quadratic mode behaviors (figure 4 inset) are of lower frequency, and thus are higher contributing when compared with the LA and TA modes between $kR_0 = 0$ and 1, which are shown in figure 3. Figures 3 and 4 also suggest that the available phonon modes at low frequencies are nearly independent of the nanostructure's cross section geometry, especially for values of $kR_0 < 1$. Because the wavenumber is $2\pi/\lambda$, phonon modes in this regime have wavelengths greater than the radial dimension of the nanostructure. Consequently, low temperature specific heat and ballistic thermal conductance for both the nanowire and nanotube systems are driven by a similar flexural phonon mode mechanism that is independent of cross-sectional geometry.

With increasing temperatures, the $T^{0.5}$ dependent specific heat regime is followed by $C \propto T^{1.5}$ dependence (figure 6). According to [1], the 2D mid-temperature regime is a result of thermally populated regions of the dispersion curves $kR_0 > 1$ and $kt < 1$, where t is the thickness of the nanotube. Figures 3 and 4 indicate that this regime of the dispersion curve is difficult to approximate with analytical forms. Past literature has described the 2D specific heat regime as T^2 dependent [27]; but the described study was based on approximated phonon dispersion relations. As expected, $kR_0 > 1$ and $kt < 1$ correspond to dominant phonon wavelengths capable of populating the length and circumferential dimensions of the structure, but too long to populate the wall dimensions.

Figure 6 shows that the thin-walled tube ($\gamma = 0.96$) is the first to exhibit 2D specific heat dependence as the temperature is increased above 0.1 K. Because $\gamma = 0.96$ has a larger mean circumference compared to the thicker walled tubes, its circumferential dimension is more readily

populated with phonon wavelengths as the wavelengths shorten with increasing temperature. Moreover, the elastic dispersion relations shown in figures 3 and 4 reveal that the $\gamma = 0.96$ tube supports lower frequency/longer wavelength LA and FA modes over a wider range of wavenumbers.

Similar to the work in [14, 25], above 20 K, the nanowire's specific heat ($\gamma = 0$) transitions to a $C \propto T^3$ dependent regime. Past literature has fit specific heat to a $C \propto T^3$ dependence by applying the commonly used Debye approximation [14, 25]. The 3D Debye approximation for specific heat is acquired by replacing the entire dispersion relation with one LA mode, $\omega = c_1 k$, and two transverse phonon modes, $\omega = c_2 k$, which is widely accepted as the phonon behavior in a bulk crystal. The 3D specific heat of a nanowire at elevated temperatures is derived by substituting the aforementioned bulk phonon relations into equation (29). As in the described literature, a $C \propto T^3$ specific heat suggests that the nanostructure does not experience phonon confinement.

The results of the present study suggest that the temperature at which the transition from 2D to 3D behavior occurs is dependent on the wall thickness of the nanotubes. Figure 6 shows that for each of the nanotube geometries investigated, except for the case of the thinnest wall tube ($\gamma = 0.96$), the specific heat converges to the T^3 behavior of the nanowire. Interestingly, the $\gamma = 0.96$ nanotube is observed to be exempt from the T^3 transition. At 600 K the dominant phonon wavelength, λ_d , is estimated using equation (32) to be approximately 1.67 nm. Because the $\gamma = 0.96$ nanotube has a 1 Å wall thickness, the phonons in the radial dimension of the nanotube (at 600 K) are incapable of thermal activation because their wavelengths are larger than the wall thickness of the tube.

Figure 7 shows the calculated ballistic conductance of cylindrical geometries $\gamma = 0, 0.5, 0.75, 0.9$, and 0.96 normalized by the value of quantum conductance $g_0 = \pi k_B^2 T / 6h$ [28]. These geometries correspond to wall thicknesses of a solid nanowire, 1.25 nm, 0.625 nm, 0.25 nm and 1 Å, respectively. The similarity in conductance at low temperatures confirms that the same transport mechanisms exist in nanowires and nanotubes regardless of wall thickness. Figures 3 and 4 verify that each structure's geometry supports comparable mode vibrations at low frequencies. Therefore, the low temperature thermal behavior of nanowires and nanotubes are conclusively identical.

According to figure 7, at temperatures between 0.3 and 150 K, ballistic conductance is seen to increase with decreasing wall thickness. At 20 K, the thermal conductance of the thinnest walled tube ($\gamma = 0.96$) is 300% greater than that of the solid nanowire ($\gamma = 0$). Reducing the nanotube wall thickness decreases the frequency of the LA and FA phonon modes, thereby increasing the integrand of equation (29), and increasing the value of thermal conductance. Interestingly, as the temperature increases past 150 K, the trend in conductance changes. At 300 K, the ballistic thermal conductance of the thinnest walled nanotube shows a 50% decrease compared to the solid nanowire (figure 7). Plausibly, because the number of thermally populated phonon modes increases with increasing temperature (via equation (30)). It is possible

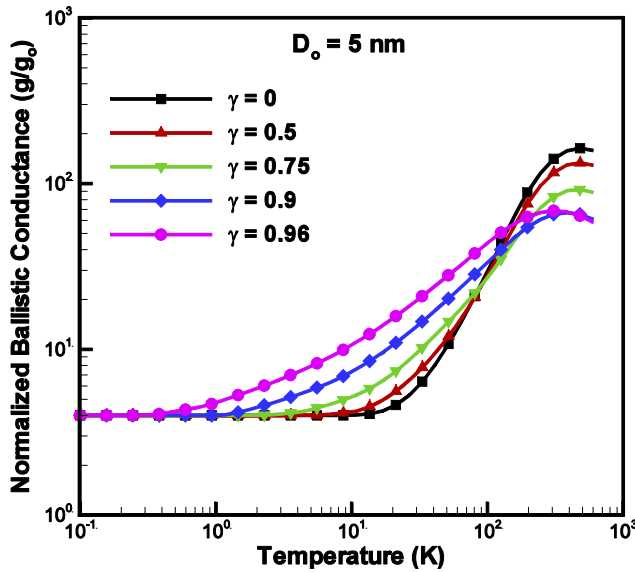


Figure 7. Normalized ballistic conductance versus temperature for five cylindrical geometries. The conductance is normalized by the quantum of thermal conductance, $g_0 = \pi^2 k_B^2 T / 3h$ [28]. Conductance values converge to $4g_0$ at low temperatures due to contributions from the four acoustic modes.

that the temperature, above 150 K, is high enough so that the effect of the increased number of contributing phonon modes supersedes the effect of the highly contributing lower frequency phonon modes which were understood to play a dominant role at lower temperatures.

3.2. Outer diameter variations

Figure 8 shows the calculated specific heat for a thick-walled nanotube ($\gamma = 0.5$) as a function of outer diameter. Specific heat is shown to decrease with increasing outer diameters at low temperatures. This reduction of specific heat in nanotubes with increasing outer diameter follows a trend similar to those observed in nanowires [14, 25].

With increasing temperatures, larger diameter nanotubes having the same value of γ are first to deviate from a 1D specific heat regime (figure 8). A similar phenomenon is seen by increasing γ for a nanotube having a fixed outer diameter (figure 6). These results suggest that increasing the outer diameter of a fixed γ nanotube is mechanistically similar to keeping the outer diameter of the tube fixed and decreasing the wall thickness. In both cases, the mean circumference of the nanostructure increases. As previously discussed in the case of the elastic dispersion curves (section 2.1), a cylindrical nanostructure with an increased mean circumference is more apt to coupled longitudinal and circumferential phonon population with increasing temperatures, and will therefore be the first structure to enter a 2D phonon confinement regime.

Figure 9 indicates that increasing the diameter of a nanotube with fixed γ increases its ballistic thermal conductance. When compared to small outer diameter nanotubes, the larger 20 nm outer diameter nanotube with the same value of γ ($\gamma = 0.5$) begins to show elevated thermal

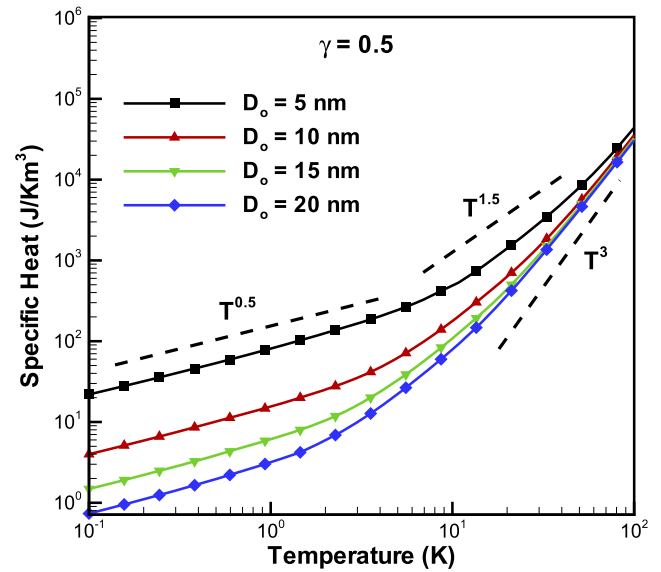


Figure 8. Specific heat versus temperature for thick-walled nanotubes ($\gamma = 0.5$) having varying outer diameter. The dashed lines are representative of $T^{0.5}$ ‘1D’, $T^{1.5}$ ‘2D’, and T^3 ‘3D’ phonon confinement behavior.

conductance values, at approximately 2 K. An approximate one order of magnitude increase in thermal conductance between the 20 nm outer diameter nanotube and the 5 nm outer diameter nanotube is observed at 200 K. The inversion of the temperature trend in conductance shown in figure 7 is not present in figure 9. According to figure 1, increasing the outer radius of the nanostructure creates a greater number of available (n, m) phonon modes within a set frequency range for a fixed value of γ ($\gamma = 0.5$). Thereby, increased temperatures increase the number of contributing phonon modes and provide a greater number of (n, m) contributions to the summations in equations (28)–(30). This explains the elevation in thermal conductance with temperature for the larger radius nanotubes.

It is worth discussing the absence of a trend inversion in ballistic conductance in figure 9, which is present in figure 7. Unlike γ variations, changing R_0 does not alter the phonon group velocities within the nanostructure, or lower the available (n, m) phonon frequencies. According to equation (31), of the few thermally populated phonons in the thin-walled structure, the lower frequency acoustic phonons have a higher contribution to internal energy when compared to the acoustic phonons in the relatively thick-walled nanostructures. Therefore, thinner walled nanostructures of the same outer diameter are shown to have a higher conductance between 2 and 150 K. As temperature increases, the lower frequency phonons, which have a greater energy contribution per mode, must compete with the sum contribution from the growing number of total (n, m) phonon modes, which, although having less contribution per mode, are more numerous in thicker walled nanostructures. Because increasing R_0 does not lower the frequency of available phonons, the contribution of each phonon to the nanostructure’s thermal conductance remains the same, therefore, variations in R_0

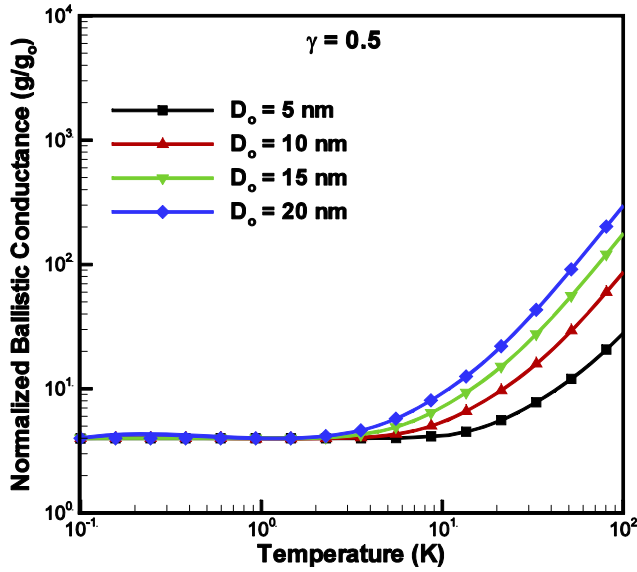


Figure 9. Normalized ballistic conductance versus temperature of a thick-walled nanotube ($\gamma = 0.5$) having varying outer diameter. The conductance is normalized by the quantum of thermal conductance, $g_o = \pi^2 k_B^2 T / 3h$ [28]. Conductance values converge to $4g_o$ at low temperatures due to contributions from the four acoustic modes.

while maintaining a fixed value of γ (figure 9) do not produce the trend inversion seen in figure 7.

4. Summary

Complete dispersion relations obtained from solving the Pochhammer-Chree frequency equation are shown to be a useful tool for investigating the thermal property dependence on geometry and size of elastic non-metallic crystalline nanotubes. While past literature has extensively evaluated 1D to 3D transitions in nanowires with temperature, this work captures similar trends in cylindrical nanotubes with varying geometry. The results of the study suggest that at low temperatures similar thermal transport mechanisms exist in nanowires and/or nanotubes regardless of their wall thickness or outer diameter. Elastic dispersion relations confirm each structure's capability to support comparable low frequency/low wavenumber modes. The transitions unique to nanotubes in the mid-temperature range are found to be dependent on geometry, and exhibit an initial $T^{1.5}$ dominance evolving towards bulk- T^3 behavior as the temperature is increased. An elevation in the thermal conductance of thin-walled nanotubes, compared to the same size outer diameter nanowire, is possible between 2 and 150 K, and is attributed to the reduction in the frequency of acoustic phonon modes. At room temperature, the same thin-walled nanotube shows a decrease in ballistic thermal conductance when compared to the nanowire comprised of the same material.

Acknowledgments

The authors thank Ravi Prasher and Tao Tong for their helpful discussion on thermal calculations of Si nanowires, Fernando

Seco Granja for his correspondence and extremely helpful PCDisp code, and Mark Marietta for his help providing ample computing resources via the 'cluster'. We also acknowledge the support of the Air Force Office of Scientific Research grant AFOSR: FA9550-08-1-0372.

Appendix A

$$\begin{aligned}
 c_{11} &= \{2n(n-1) - (\beta^2 - k^2)a^2\}Z_n(\alpha_1 a) \\
 &\quad + 2\lambda_1 \alpha_1 a Z_{n+1}(\alpha_1 a), \\
 c_{12} &= 2k\beta_1 a^2 Z_n(\beta_1 a) - 2ka(n+1)Z_{n+1}(\beta_1 a), \\
 c_{13} &= -2n(n-1)Z_n(\beta_1 a) + 2\lambda_2 n\beta_1 a Z_{n+1}(\beta_1 a), \\
 c_{14} &= \{2n(n-1) - (\beta_1^2 - k^2)a^2\}W_n(\alpha_1 a) \\
 &\quad + 2\alpha_1 a W_{n+1}(\alpha_1 a), \\
 c_{15} &= 2\lambda_2 k\beta_1 a^2 W_n(\beta_1 a) - 2(n+1)ka W_{n+1}(\beta_1 a), \\
 c_{16} &= -2n(n-1)W_n(\beta_1 a) + 2n\beta_1 a W_{n+1}(\beta_1 a), \\
 c_{21} &= 2n(n-1)Z_n(\alpha_1 a) - 2\lambda_1 n\alpha_1 a Z_{n+1}(\alpha_1 a), \\
 c_{22} &= -k\beta_1 a^2 Z_n(\beta_1 a) + 2ka(n+1)Z_{n+1}(\beta_1 a), \\
 c_{23} &= -\{2n(n-1) - \beta^2 a^2\}Z_n(\beta_1 a) - 2\lambda_2 \beta_1 a Z_{n+1}(\beta_1 a), \\
 c_{24} &= 2n(n-1)W_n(\alpha_1 a) - 2n\alpha_1 a W_{n+1}(\alpha_1 a), \\
 c_{25} &= -\lambda_2 k\beta_1 a^2 W_n(\beta_1 a) + 2ka(n+1)W_{n+1}(\beta_1 a), \\
 c_{26} &= -\{2n(n-1) - \beta^2 a^2\}W_n(\beta_1 a) - 2\beta_1 a W_{n+1}(\beta_1 a), \\
 c_{31} &= 2nk\alpha_1 Z_n(\alpha_1 a) - 2\lambda_1 k\alpha_1 a^2 Z_{n+1}(\alpha_1 a), \\
 c_{32} &= n\beta_1 a Z_n(\beta_1 a) - (\beta^2 - k^2)a^2 Z_{n+1}(\beta_1 a), \\
 c_{33} &= -nka Z_n(\beta_1 a), \\
 c_{34} &= 2nka W_n(\alpha_1 a) - 2k\alpha_1 a^2 W_{n+1}(\alpha_1 a), \\
 c_{35} &= \lambda_2 n\beta_1 a W_n(\beta_1 a) - (\beta^2 - k^2)a^2 W_{n+1}(\beta_1 a), \\
 c_{36} &= -nka W_n(\beta_1 a), \\
 c_{41} &= \{2n(n-1) - (\beta^2 - k^2)b^2\}Z_n(\alpha_1 b) \\
 &\quad + 2\lambda_1 \alpha_1 b Z_{n+1}(\alpha_1 b), \\
 c_{42} &= 2k\beta_1 b^2 Z_n(\beta_1 b) - 2kb(n+1)Z_{n+1}(\beta_1 b), \\
 c_{43} &= -2n(n-1)Z_n(\beta_1 b) + 2\lambda_2 n\beta_1 b Z_{n+1}(\beta_1 b), \\
 c_{44} &= \{2n(n-1) - (\beta_1^2 - k^2)b^2\}W_n(\alpha_1 b) \\
 &\quad + 2\alpha_1 b W_{n+1}(\alpha_1 b), \\
 c_{45} &= 2\lambda_2 k\beta_1 b^2 W_n(\beta_1 b) - 2(n+1)kb W_{n+1}(\beta_1 b), \\
 c_{46} &= -2n(n-1)W_n(\beta_1 b) + 2n\beta_1 b W_{n+1}(\beta_1 b), \\
 c_{51} &= 2n(n-1)Z_n(\alpha_1 b) - 2\lambda_1 n\alpha_1 b Z_{n+1}(\alpha_1 b), \\
 c_{52} &= -k\beta_1 b^2 Z_n(\beta_1 b) + 2kb(n+1)Z_{n+1}(\beta_1 b), \\
 c_{53} &= -\{2n(n-1) - \beta^2 b^2\}Z_n(\beta_1 b) - 2\lambda_2 \beta_1 b Z_{n+1}(\beta_1 b), \\
 c_{54} &= 2n(n-1)W_n(\alpha_1 b) - 2n\alpha_1 b W_{n+1}(\alpha_1 b), \\
 c_{55} &= -\lambda_2 k\beta_1 b^2 W_n(\beta_1 b) + 2kb(n+1)W_{n+1}(\beta_1 b), \\
 c_{56} &= -\{2n(n-1) - \beta^2 b^2\}W_n(\beta_1 b) - 2\beta_1 b W_{n+1}(\beta_1 b), \\
 c_{61} &= 2nk\alpha_1 Z_n(\alpha_1 b) - 2\lambda_1 k\alpha_1 b^2 Z_{n+1}(\alpha_1 b), \\
 c_{62} &= n\beta_1 b Z_n(\beta_1 b) - (\beta^2 - k^2)b^2 Z_{n+1}(\beta_1 b), \\
 c_{63} &= -nkb Z_n(\beta_1 b), \\
 c_{64} &= 2nkb W_n(\alpha_1 b) - 2k\alpha_1 b^2 W_{n+1}(\alpha_1 b), \\
 c_{65} &= \lambda_2 n\beta_1 b W_n(\beta_1 b) - (\beta^2 - k^2)b^2 W_{n+1}(\beta_1 b), \\
 c_{66} &= -nkb W_n(\beta_1 b),
 \end{aligned}$$

where $a = R_o$ and $b = R_i$. If α^2 or β^2 is greater than zero, Z_n is the n th order Bessel Function of the first kind J_n . If α^2 or β^2 is less than zero, Z_n corresponds to the modified Bessel function of the first kind I_n . Similarly, W_n corresponds to the Bessel function of the second kind, Y_n , or modified Bessel function of the second kind, K_n , depending on the sign of α^2 or β^2 . The constants λ_1 , and λ_2 are $+1$ if Bessel functions J and Y are used, and -1 if I and K are used. The reader is referred to [17], for further specifics regarding the derivation of the elastic frequency equation.

Appendix B

Equation (27) is designed to force the group velocity of only the acoustic modes ($m = 1$ for $n = 0$ and 1) to zero at maximum wavenumber. While not designed to do so, the group velocity of modes $m = 2$ and 3 for $n = 0$ and 1 are near zero. For $m > 3$ for $n = 0$ and 1, and for all m modes belonging to $n > 1$, modification of the elastic dispersion relation using equation (27) causes slightly negative group velocities at maximum wavenumber, especially for higher frequency modes. This has been found to be a mathematical artifact having no physical meaning. Using equation (31) and considering the temperature domain of interest, 0.1–600 K, the highest thermally contributing frequencies of the dispersion curve may be estimated as those frequencies below 71 THz. Therefore, using the modification term creates an effective ‘Born–von-Karman’ boundary condition at k_{\max} in the modes that contribute most to specific heat and thermal conductance and is therefore a better approximation for phonon dispersion than the elastic dispersion curves. While the calculation of thermal conductivity would require further estimation of phonon scattering effects and is therefore beyond the scope of this investigation, it is unarguably a natural extension of the current findings. It has been suggested in the literature that using the elastic dispersion relations without further modification would only affect thermal conductivity calculations by less than 10% [29].

References

- [1] Prasher R 2008 Thermal boundary resistance and thermal conductivity of multiwalled carbon nanotubes *Phys. Rev. B* **77** 075424
- [2] Chen G 2000 Particularities of heat conduction in nanostructures *J. Nanoparticle Res.* **2** 199–204
- [3] Chen R *et al* 2008 Thermal conductance of thin silicon nanowires *Phys. Rev. Lett.* **101** 105501
- [4] Li D *et al* 2003 Thermal conductivity of individual silicon nanowires *Appl. Phys. Lett.* **83** 2934–6
- [5] Hochbaum A I *et al* 2008 Enhanced thermoelectric performance of rough silicon nanowires *Nature* **451** 163–7
- [6] Chen Y *et al* 2005 Monte Carlo simulation of silicon nanowire thermal conductivity *J. Heat Transfer* **127** 1129–37
- [7] Mingo N *et al* 2003 Predicting the thermal conductivity of Si and Ge nanowires *Nano Lett.* **3** 1713–6
- [8] Mingo N 2003 Calculation of Si nanowire thermal conductivity using complete phonon dispersion relations *Phys. Rev. B* **68** 113308
- [9] Berber S, Kwon Y-K and Tománek D 2000 Unusually high thermal conductivity of carbon nanotubes *Phys. Rev. Lett.* **84** 4613
- [10] Hone J *et al* 1999 Thermal conductivity of single-walled carbon nanotubes *Phys. Rev. B* **59** R2514–6
- [11] Lukes J R and Zhong H 2007 Thermal conductivity of individual single-walled carbon nanotubes *J. Heat Transfer* **129** 705–16
- [12] Savin A V, Hu B and Kivshar Y S 2009 Thermal conductivity of single-walled carbon nanotubes *Phys. Rev. B* **80** 195423
- [13] Dresselhaus M S 2000 Phonons in carbon nanotubes *Adv. Phys.* **49** 705–814
- [14] Tong T, Prasher R and Majumdar A 2007 Heat capacity and thermal conductance calculations for non-metallic crystalline nanowires based on elastic dispersion relations *ASME Conf. Proc.* **2007** 631–7
- [15] Pokatilov E P, Nika D L and Balandin A A 2005 Acoustic phonon engineering in coated cylindrical nanowires *Superlatt. Microstruct.* **38** 168–83
- [16] Pokatilov E P, Nika D L and Balandin A A 2005 Acoustic-phonon propagation in rectangular semiconductor nanowires with elastically dissimilar barriers *Phys. Rev. B* **72** 113311
- [17] Graff K 1991 *Wave Motion in Elastic Solids* (Mineola, NY: Dover)
- [18] Song F, Huang G and Varadan V 2009 Study of wave propagation in nanowires with surface effects by using a high-order continuum theory *Acta Mech.* **209** 129–39
- [19] Gu M X *et al* 2006 Change in thermal conductivity of cylindrical silicon nanowires induced by surface bonding modification *J. Appl. Phys.* **100** 094304
- [20] Linli Z and Xiaojing Z 2009 Modification of the phonon thermal conductivity in spatially confined semiconductor nanofilms under stress fields *Europhys. Lett.* **88** 36003
- [21] Popov V N, Van Doren V E and Balkanski M 2000 Elastic properties of single-walled carbon nanotubes *Phys. Rev. B* **61** 3078
- [22] Mahan G D and Jeon G S 2004 Flexure modes in carbon nanotubes *Phys. Rev. B* **70** 075405
- [23] Mahan G D 2002 Oscillations of a thin hollow cylinder: carbon nanotubes *Phys. Rev. B* **65** 235402
- [24] Kittel C 2004 *Introduction to Solid State Physics* (New York: Wiley)
- [25] Prasher R, Tong T and Majumdar A 2008 Approximate analytical models for phonon specific heat and ballistic thermal conductance of nanowires *Nano Lett.* **8** 99–103
- [26] Ashcroft N and Mermin D 1976 *Solid State Physics* (Stamford, CT: Thomson Learning)
- [27] Dames C 2006 Thermal properties of nanowires and nanotubes: modeling and experiments *Mechanical Engineering* (Massachusetts: Massachusetts Institute of Technology)
- [28] Schwab K *et al* 2000 Measurement of the quantum of thermal conductance *Nature* **404** 974–7
- [29] Au Yeung T C *et al* 2006 Impact of surface bond-order loss on phonon dispersion relations and thermal conductivity of cylindrical Si nanowires *Phys. Rev. B* **74** 155317

Thermal Properties of Nanotubes and Nanowires with Acoustically Stiffened Surfaces

Michael F. P. Bifano and Vikas Prakash*

Case Western Reserve University

Department of Mechanical and Aerospace Engineering

10900 Euclid Avenue

Cleveland, OH 44106-7222

**Author to whom correspondence should be addressed vikas.prakash@case.edu*

ABSTRACT

A core-shell elasticity model is employed to investigate the effect of a nanowire and nanotube's increased surface moduli on its specific heat, ballistic thermal conductance, and thermal conductivity as a function of temperature. Phonon confinement is analyzed using approximated phonon dispersion relations that result from the solutions to the frequency equation of a vibrating tube. The results of the investigation indicate an approximate 10 % decrease in lattice thermal conductivity and ballistic thermal conductance for a 10 nm outer diameter crystalline nanotube with an inner diameter of 5 nm when the average Young's Modulus of the first three atomic layers on both the inner and outer free surfaces are increased by a factor of 1.53. The specific heat of the tube structure is also found to decrease by up to 20 % at 150 K. In contrast, a 10 nm outer diameter nanowire composed of similar material exhibits up to a 10 %

increase in thermal conductivity, a 25 % increase in ballistic thermal conductance, and a 48 % increase in specific heat when its outer free surface is acoustically stiffened to the same degree. Our simplified model may be extended to investigate the acoustic tuning of nanowires and nanotubes by inducing surface stiffening or softening via appropriate surface chemical functionalization or coatings.

Keywords: Nanowire, Nanotube, Thermal Conductivity, Surface Effects, Surface Stress, Phonon Confinement

1. Introduction

Nanowire and nanotubes with diameters below tens of nanometers experience a significant increase in the surface area to volume ratio. As a result, a large number of surface atoms become under-coordinated due to bond order differences. With decreasing diameter the rising number of under-coordinated surface atoms begin to influence the overall material properties of the nanostructure¹. Both the application of stress as well as the presence of acoustically stiffened lateral surfaces are expected to alter the mechanical¹, electrical², and thermal properties^{3, 4} of nanostructures. While residual surface stresses are present to some degree in all nanostructures, the vast majority of theoretical nanowire and nanotube thermal conductivity predictions have not accounted for the actual surface moduli⁵⁻⁹, potentially leading to significant errors in predicted values.

In general, the thermal conductivity of a nanowire or nanotube is dependent on the geometric confinement of phonon modes (dictated by phonon dispersion) as well as scattering mechanisms due to phonon-phonon, phonon-electron, phonon-impurity, and phonon-boundary

interactions. Since all these scattering mechanisms are frequency and/or group velocity dependent¹⁰, they are expected to be altered by phonon confinement effects. Even in the absence of boundary scattering effects, phonon confinement is believed to play a role in the modification of thermal conductivity. In this regards, Zou and Balandin⁸ have shown that in nanostructures, geometric phonon confinement effects lead to 9 % reduction in bulk thermal conductivity in the absence of boundary scattering, *i.e.*, purely specular boundaries, for nanowires whose diameter is comparable to the phonon mean free path. In the present study, we show that besides geometrical effects, phonon confinement is also altered by the presence acoustic stiffening at the walls of the nanowires and nanotubes.

In recent studies, continuum elastic dispersion relations have been used to show the importance of geometric phonon confinement on specific heat and ballistic thermal conductance of single crystalline nanowires with temperature¹¹⁻¹⁴. Lu, *et al.*¹² have shown that phonon dispersion combined with phonon radiative transport, accounting for non-equilibrium phonon distributions, is capable of accurately predicting the thermal conductivity of 10 x 20 nm rectangular cadmium telluride nanowires. Chen *et al.*¹¹ have used Monte Carlo simulations to show that phonon dispersion relations derived from continuum elasticity could be effectively used to evaluate the thermal conductivity of silicon nanowires on the sub 100 nm scale. Based on these studies, geometric phonon confinement effects are necessary when predicting the thermal properties of nanowires and nanotubes whose characteristic lengths are of the order of the dominant phonon wavelengths of the system.

Phonon dispersion is understood to be not only affected by geometry of the nanostructures, but also on the boundary conditions¹⁵⁻²⁰. Mukdadi *et al.*¹⁶ have used a semi-analytical continuum-based analysis to show how phonon dispersion is altered in rectangular

nanowires comprised of bilayers of two perfectly bonded materials. Pokatilov *et al.* have used the elastic continuum approach to demonstrate how phonon dispersion is altered when rectangular nanowires^{17, 18} and thin films¹⁹ are embedded in both acoustically soft and acoustically hard materials. Their results suggest that the sound velocity mismatch at the core-clad interface is a potentially significant parameter in acoustic tuning of composite nanostructures. Using an elastic continuum analysis, Zou *et al.*²⁰ found that in GaN thin films coated with 2 nm AlN, partial phonon confinement can lead to an enhancement in thermal conductivity, and that the thermal conductivity could be tuned to higher or lower values by adjusting the clad-layer thickness while maintaining the thickness of the heterostructure. Phonon confinement effects due to the presence of stiffer boundary coatings may be analogous to the acoustic stiffening of surfaces. If so, the thermal conductivity would be dependent on the surface properties of the nanostructure, *i.e.*, surface moduli, especially as characteristic dimensions of the structure are reduced.

The Bond-order-length-strength (BOLS) model correlates the coordination number of atoms to bond-length and stiffness as well as other properties, such as, localization of charge and electro-affinity⁴. The stiffness of under-coordinated surface atoms is in particular related to the elastic properties, *e.g.*, the Young's modulus and density. Yueng⁴ utilized a continuum elastic dispersion model along with the BOLS model to analyze the effect of surface stiffening on the thermal conductivity of Si nanowires. The study determined how a stiffened surface alters the separate contributions from the torsional, longitudinal and flexural phonon branch's thermal conductivity as a nanowire's outer diameter decreases. The study did not calculate a total thermal conductivity by summing the contributions from each phonon branch.

In the present work, we investigate the specific heat, ballistic thermal conductance, and thermal conductivity of a single crystalline carbon lattice nanowire with an acoustically stiffened outer shell. These results are compared with a nanotube having the same outer diameter and composed of the same lattice material but with both the inner and outer surfaces perfectly bonded to a thin acoustically stiffened skin. The inclusion of the stiffened skin on the inner free surface of a nanotube is found to have interesting consequences on its predicted thermal properties. Thermal conductivity is found to increase by up to 10 % when the acoustically stiffened skin is placed on the outside of the nanowire, but decrease when the acoustically stiffened skin is placed on both the inner and outer wall surfaces of the nanotube. Such capability to tune (decrease) thermal conductivity via confinement of phonon modes by acoustic stiffening in nanotubes may improve the efficiency of next generation thermoelectric devices. On the contrary, a more complete understanding of thermal transport in the presence of acoustically stiffened surfaces in nanowires may lead to the improvement of thermal management materials with increased thermal conductivity.

2. The Core-Shell BOLS Model

In the present study, we use an isotropic continuum wave model to obtain dispersion relations, *i.e.*, relationship between mode frequency ω , and wavenumber k , in a 10 nm outer diameter nanowire and nanotube both in the presence and absence of acoustically stiffened surface(s). Phonon confinement is analyzed by using the $\omega = f(k)$ dispersion relationship as an approximation for the actual phonon dispersion relation in the nanostructure. The continuum approximation is an accurate description of the actual phonon dispersion relation since the average phonon mean free path is of the order of the nanowire or nanotube diameter²¹. First,

calculations of specific heat and ballistic thermal conductance are performed. Subsequently, estimates of thermal conductivity are obtained by use of a combined relaxation time accounting for phonon boundary, impurities, and Umklapp scattering. In the present study the absolute magnitudes of specific heat, ballistic thermal conductance, and thermal conductivity are of less concern, instead, the focus is to determine the relative changes in the thermal properties of nanowire and nanotubes with the inclusion of acoustically stiffened surface(s). The material investigated in the present study is a single crystalline carbon structure with a diamond lattice, but the core-skin elasticity model can easily be extended to materials with a variety of lattice constants and material properties, including various nanolayer coatings on nanotubes and nanowires.

The acoustically stiffened surfaces of the nanowire and nanotube are modeled using a BOLS model for the elastic moduli. In this model, the Young's modulus of each atomic layer increases as

$$\frac{E_i}{E_1} = \alpha_i^{-(w+3)} \quad (i = 1, 2, 3), \quad (1)$$

where i is the layer index ($i = 3$ corresponding to the outermost layer); E_1 represents the Young's modulus of the bulk material; w is an adjusting parameter related to the material, for carbon $w = 2.56$ ¹; α_i is the bond contraction coefficient and is equal to the bond length in the i^{th} atomic layer divided by the bond length in the bulk material. The bond contraction coefficient is determined for each of the outer three surfaces layers using coordination numbers (CN) of 3.91, 6, and 12 corresponding to the outer, middle, and inner three surface layers of a face-center cubic lattice (Fig. 2). Note, for the outer surface layer, the CN has been reduced from 4 to 3.91, so as to account for surface curvature¹.

Eq. (1) is averaged over the last three atomic surface layers forming a ratio for the Young's moduli of two separate materials: a core material having a Young's Modulus E_1 , and density ρ_1 , and likewise a shell structure on both inner and outer surfaces having a Young's Modulus E_2 , and density ρ_2 (Fig. 1). Note that the new subscript, 2, refers to an acoustically stiffened material having the elastic properties of the average of the three atomic surface layers.

Assuming the Poisson's ration, ν , to be the same for the core and the shell regions, the Lamé' constants for the core and shell regions, *i.e.*, $\lambda_{1,2}$ and $\mu_{1,2}$, are proportional to $E_{1,2}$, where $\lambda_{1,2} = \nu E_{1,2} / ((1+\nu)(1-2\nu))$ and $\mu_{1,2} = E_{1,2} / 2(1+\nu)$. In the present study, the Young's modulus of the core material is chosen to be $E_1 = 1.3$ TPa, $\nu = 0.27$, and $\rho_1 = 2260$ Kg/m³. Subsequently, according to the BOLS model^{1, 4}, the acoustically stiffened surface layer(s) have moduli and wave speeds that are 1.53 and 1.18 times that of the core material, respectively.

The discontinuity in the material properties at the interface between the skin and the core structure is handled by enforcing the displacement and stress fields to be continuous across the interface. The cylindrical nanostructures maintain an outer radius, R_o , of 5 nm. The dispersion relations are solved for ratios of inner to outer tube radius, γ , where $\gamma = R_i/R_o$. $\gamma = 0$ and 0.5 are investigated, where $\gamma = 0$ represents a solid nanowire, and $\gamma = 0.5$ represents a thick-walled tube. The skin thickness, δ , of the BOLS affected layer is maintained at 0.534 nm and is assumed to be equal to $3d$, where $d = 1.78$ Å, the lattice constant of the crystal. The solid nanowire ($\gamma = 0$) has an acoustically stiffened layer on the outer surface, while the nanotube ($\gamma = 0.5$) is modeled with acoustically stiffer layers having similar elastic properties on both the inner and outer surfaces (Fig. 1). In the $\gamma = 0.5$ case, the distances from the tube axis to the first and second interfaces are denoted by a and b , respectively (Fig. 1). The nanowire case, $\gamma = 0$, is modeled using $R_i = a = 0$.

For comparison, a similar wave model is established for a nanowire and nanotube ($\gamma = 0$ and 0.5) lacking acoustically stiffened BOLS layers.

3. Calculating Elastic Dispersion Relations

The frequency equation for the nanostructures is derived using a decomposition of the displacement field into a scalar potential, $\phi_{1,2}$, and a vector potential, $\mathbf{H}_{1,2}$, in both the core and shell materials denoted by subscripts 2 and 1, respectively:

$$\mathbf{u}_{1,2} = \nabla \phi_{1,2} + \nabla \times \mathbf{H}_{1,2} \quad (2)$$

The potentials $\phi_{1,2}$ and $\mathbf{H}_{1,2}$ satisfy their respective wave equations

$$\nabla^2 \phi_{1,2} = \frac{1}{c_{l,2}^2} \frac{\partial^2 \phi_{1,2}}{\partial t^2} \quad (3)$$

$$\nabla^2 \mathbf{H}_{1,2} = \frac{1}{c_{t,2}^2} \frac{\partial^2 \mathbf{H}_{1,2}}{\partial t^2} \quad (4)$$

where the transverse and longitudinal wave speeds are defined as $c_{t,2} = \sqrt{\mu_{1,2}/\rho_{1,2}}$ and $c_{l,2} = \sqrt{\lambda_{1,2} + 2\mu_{1,2}/\rho_{1,2}}$, respectively.

According to Eq. (2), the scalar components with respect to a cylindrical coordinate system of the displacement field in the core and shell materials can be described as (Fig. 1):

$$u_{r,2} = \frac{\partial \phi_{1,2}}{\partial r} + \frac{1}{r} \frac{\partial H_{z,2}}{\partial \theta} - \frac{\partial H_{\theta,2}}{\partial z} \quad (5)$$

$$u_{\theta_{1,2}} = \frac{1}{r} \frac{\partial \phi_{1,2}}{\partial \theta} + \frac{\partial H_{r_{1,2}}}{\partial z} - \frac{\partial H_{z_{1,2}}}{\partial r} , \quad (6)$$

$$u_{z_{1,2}} = \frac{\partial \phi_{1,2}}{\partial z} + \frac{1}{r} \frac{\partial}{\partial r} (r H_{\theta_{1,2}}) - \frac{1}{r} \frac{\partial H_{r_{1,2}}}{\partial \theta} . \quad (7)$$

Using the potentials we look for solutions of the form²²:

$$\phi_{1,2} = f(r)_{1,2} \cos n\theta \cos(\omega t + kz) , \quad (8)$$

$$H_{r_{1,2}} = h_r(r)_{1,2} \sin n\theta \sin(\omega t + kz) , \quad (9)$$

$$H_{\theta_{1,2}} = h_\theta(r)_{1,2} \cos n\theta \sin(\omega t + kz) , \quad (10)$$

$$H_{z_{1,2}} = h(r)_{1,2} \cos n\theta \cos(\omega t + kz) . \quad (11)$$

The radially dependent functions in the above product solutions, $f(r)$, $h_r(r)$, $h_\theta(r)$, and $h(r)$ are linear combinations of Bessel functions. The radial functions are decomposed into the following

$$f_{1,2} = A_{1,2} Z_n(|\alpha_{1,2}|r) + \bar{A}_{1,2} W_n(|\alpha_{1,2}|r) , \quad (12)$$

$$h_{1,2} = C_{1,2} Z_n(|\beta_{1,2}|r) + \bar{C}_{1,2} W_n(|\beta_{1,2}|r) , \quad (13)$$

$$h_{r1,2} = -h_{\theta1,2} = B_{1,2} Z_{n+1}(|\beta_{1,2}|r) + \bar{B}_{1,2} W_{n+1}(|\beta_{1,2}|r) , \quad (14)$$

where $A_{1,2}, \bar{A}_{1,2}, B_{1,2}, \bar{B}_{1,2}, C_{1,2}, \bar{C}_{1,2}$ are 12 unique unknown constants. The bar above the unknown constants represents coefficients to the modified Bessel functions (W_n) of order n .

Because W_n is unbounded at $r = 0$, the barred constants are zero in the core material of the solid nanowire ($\gamma = 0$). Since the shell material is always a cylinder, even in the $\gamma = 0$ BOLS case, unbounded solutions are permitted at the origin and therefore the hardened shell material contains both unbarred and barred constants.

The dispersion relation, *i.e.*, the relationship between frequency, ω , and wavenumber k , is embedded in the terms α and β as $\alpha_{1,2} = \sqrt{\omega^2/c_{l_{1,2}}^2 - k^2}$ and $\beta_{1,2} = \sqrt{\omega^2/c_{t_{1,2}}^2 - k^2}$, respectively.

Stress fields are written via the isotropic elastic constitutive relationship (Hooke's Law):

$$\sigma_{ij_{1,2}} = \lambda_{1,2} e_{kk_{1,2}} \delta_{ij} + 2\mu_{1,2} e_{ij_{1,2}}. \quad (15)$$

The components of the strain tensor, $e_{ij_{1,2}}$, are given by

$$e_{rr_{1,2}} = \frac{\partial u_{r_{1,2}}}{\partial r}, \quad (16)$$

$$e_{\theta\theta_{1,2}} = \frac{1}{r} \frac{\partial u_{\theta_{1,2}}}{\partial \theta} + \frac{u_{r_{1,2}}}{r}, \quad (17)$$

$$e_{zz_{1,2}} = \frac{\partial u_{z_{1,2}}}{\partial z}, \quad (18)$$

$$e_{r\theta_{1,2}} = \frac{1}{2} \left(\frac{1}{r} \frac{\partial u_{r_{1,2}}}{\partial \theta} + \frac{\partial u_{\theta_{1,2}}}{\partial r} - \frac{u_{\theta_{1,2}}}{r} \right), \quad (19)$$

$$e_{rz_{1,2}} = \frac{1}{2} \left(\frac{\partial u_{z_{1,2}}}{\partial r} + \frac{\partial u_{r_{1,2}}}{\partial z} \right), \quad (20)$$

$$e_{\theta z_{1,2}} = \frac{1}{2} \left(\frac{\partial u_{\theta_{1,2}}}{\partial z} + \frac{1}{r} \frac{\partial u_{z_{1,2}}}{\partial \theta} \right), \quad (21)$$

and are determined by differentiation of Eqs. (5) to (7).

The displacement field is assumed to be a continuous function of the radius, r . As shown in Fig. 1, $u(R_i < r < a)$ corresponds to the respective inner shell equations, $u(a < r < b)$ corresponds to core material equations, and $u(b < r < R_o)$ corresponds to outer shell equations. The arduous task that remains is to establish a set of homogeneous equations that include the imposed boundary and interface conditions. This set of homogeneous equations can be written as $\mathbf{A}\mathbf{c} = 0$, where \mathbf{c} is the vector containing the unknown constants (up to 18 elements from $[A_{1,2}, \bar{A}_{1,2}, B_{1,2}, \bar{B}_{1,2}, C_{1,2}, \bar{C}_{1,2}]$). The matrix \mathbf{A} contains the coefficients to these unknown constants and is unique given the necessary boundary conditions for the cases when $\gamma = 0$ (nanowire) with acoustically stiffened outer surface, $\gamma = 0.5$ (nanotube) with stiffened inner and outer surfaces, and $\gamma = 0$ and 0.5 without stiffened surface(s). Non-trivial ω vs. k solutions are found by numerically solving the appropriate frequency equation, *i.e.*, the determinant $|\mathbf{A}| = 0$.

3.1. Boundary Conditions

The appropriate homogenous equations written from the applicable boundary and interface conditions are presented below in the following order: 1) $\gamma = 0$ without a stiffened surface; 2) $\gamma = 0.5$ without stiffened surfaces; 3) $\gamma = 0$ with a stiffened outer surface; 4) $\gamma = 0.5$ with stiffened inner and outer surfaces. The resulting frequency equation is solved using a custom bisection algorithm written in MATLAB.

3.1.1. Nanowire without a Stiffened Surface

The case of a nanowire without a stiffened surface involves only the core material. The inner radius is $R_i = a = 0$. The outer radius is $b = R_o = 5$ nm. Moreover, for the unstiffened nanowire

$$\sigma_{r\theta_1}(R_o) = \sigma_{r\theta_1}(R_o) = \sigma_{rz_1}(R_o) = 0, \quad (22)$$

and

$$|u_{i_1}(0)| < \infty \quad i = r, \theta, z. \quad (23)$$

Eq. (23) is automatically satisfied by setting the barred constants of Eqs. (12) to (14) to zero. The traction free surface condition at $r = R_o$ is satisfied by constructing a 3x3 \mathbf{A} matrix having each row corresponding to an equation from Eq. (22), and each column corresponds to a coefficient from one of the 3 unknown constants, A_I , B_I , and C_I .

3.1.2. Nanotube without Stiffened Surfaces

The inner radius of the nanotube $a = R_i = 2.5$ nm while the outer radius $b = R_o = 5$ nm. As in the case of the nanowire, equations which correspond to only the core material remain. The boundary conditions are written as:

$$\sigma_{r\theta_1}(R_o) = \sigma_{r\theta_1}(R_o) = \sigma_{rz_1}(R_o) = 0 \quad (24)$$

and

$$\sigma_{r\theta_1}(R_i) = \sigma_{r\theta_1}(R_i) = \sigma_{rz_1}(R_i) = 0. \quad (25)$$

The inner and outer traction free surfaces at $r = R_i$ and $r = R_o$ are satisfied by constructing a 6x6 **A** matrix having each row corresponding to an equation from Eq. (24) and Eq. (25), and each column corresponding to a coefficient from one of the 6 unknown constants, $A_1, \bar{A}_1, B_1, \bar{B}_1, C_1, \bar{C}_1$. Barred constants are now permitted for the nanotube since unbounded solutions are of no concern at $r = 0$.

3.1.3. Nanowire with a Stiffened Outer Surface (Outer BOLS Skin Layer)

The outer most surface of the stiffened shell material is a free surface, and therefore traction free boundary conditions apply⁴:

$$\sigma_{rr_2}(R_o) = \sigma_{r\theta_2}(R_o) = \sigma_{rz_2}(R_o) = 0 \quad (26)$$

The above equations represent 3 rows of the **A** matrix having 6 unknown constants $A_2, \bar{A}_2, B_2, \bar{B}_2, C_2, \bar{C}_2$. The coefficients to these constants form the first 6 columns of the 9 x 9 **A** matrix. At $r = b$, the tractions at the interface are continuous and written as,

$$\sigma_{rr_2}(b) - \sigma_{rr_1}(b) = 0, \quad (27)$$

$$\sigma_{r\theta_2}(b) - \sigma_{r\theta_1}(b) = 0, \quad (28)$$

$$\sigma_{rz_2}(b) - \sigma_{rz_1}(b) = 0. \quad (29)$$

The first terms in Eqs. (27) through (29) share the same 6 constants as Eqs. (26) and therefore share the first 6 columns. The second set of terms in Eqs. (27) through (29) belong to the solid core material and contain the coefficients to the unbarred constants A_I, B_I, C_I , forming the 4th- 6th rows and 7th - 9th columns of the 9 x 9 **A** matrix. The final 3 rows of **A** are formed from the homogeneous displacement equations,

$$u_{r_2}(b) - u_{r_1}(b) = 0 \quad (30)$$

$$u_{\theta_2}(b) - u_{\theta_1}(b) = 0 \quad (31)$$

$$u_{z_2}(b) - u_{z_1}(b) = 0 \quad (32)$$

The first terms of Eqs. (30) to (32) are associated with the stiffened outer surface and compose of rows 7 – 9 and columns 1 – 6. These **A** matrix terms contain the coefficients to the constants $A_2, \bar{A}_2, B_2, \bar{B}_2, C_2, \bar{C}_2$. The second set of terms of Eqs. (30) to (32) are associated with the core material and make up rows 7 – 9 and columns 7 – 9, corresponding to coefficients to the constants A_1, B_1, C_1 . The bounded condition at $r = 0$ is automatically satisfied by the condition that $\bar{A}_1 = \bar{B}_1 = \bar{C}_1 = 0$. Note that since the stiffened surface is a cylinder, the barred constants $\bar{A}_2, \bar{B}_2, \bar{C}_2 \neq 0$.

3.1.4. Nanotube with Stiffened Surfaces (BOLS Skins)

The nanotube with stiffened inner and outer surfaces (BOLS skins) lead to the most complicated **A** matrix (18 x 18 matrix) satisfying 3 traction free equations at $r = R_o$, 6 interface equations at $r = b$, 6 interface equations at $r = a$, and 3 traction free equations at $r = R_i$. Since, the three layers are comprised of hollow concentric cylinders, each term in the **A** matrix is a coefficient belonging to one of the 6 constants, $A_{1,2}, \bar{A}_{1,2}, B_{1,2}, \bar{B}_{1,2}, C_{1,2}, \bar{C}_{1,2}$. The constants for the stiffened skins are considered twice, forming 18 columns.

The 3 homogenous traction free boundary conditions of Eq. (26) apply to the outer stiffened surface. The interface at $r = b$ is described by Eqs. (27) to (32). The additional interface between the core material and inner stiffened surface is defined using Eqs. (27) to (32),

but with b replaced by a . The innermost surface is defined by traction free equations similar to Eq. (26), but with R_o replaced with R_i .

3.2. Frequency Solutions of $|\mathbf{A}| = 0$

An infinite number of allowable modes of vibration of the structure, each defined by $\omega(n,m,k)$, can be obtained from solutions of the appropriate \mathbf{A} determinant. The azimuthal mode number, n , is equal to the number of radial nodal lines between $\theta = 0$ and π . Therefore, $n = 0$ describes azimuthally independent modes such as the class of longitudinal and torsional mode types. $n = 1$ has one nodal line between $\theta = 0$ and π , and classifies the first flexural mode. $n > 1$ describes higher order flexural modes. m is the radial mode number equal to the number of nodal lines perpendicular to an arbitrary radius r , between $r = R_i$ and $r = R_o$. Because two solutions are present for $n = 0$, past analysis of wave propagation in cylindrical structures have separated the longitudinal and torsional mode types into separate solvable determinants²². Given the objective of gathering and subsequently integrating the appropriate number of phonon branches, this preprocessing step is not performed.

In the present study, 51 azimuthal dispersion plots of ω vs. k are found each having 175 m branches; $n = 0$ consists of both the torsional and longitudinal mode types, while $n = 1$ to 50 represents the flexural modes. Flexural modes in the x - and y - directions are identical in the wave analysis of vibrating isotropic rods and cylinders. Given this symmetry, flexural modes are counted twice.

4. Approximating the Phonon Dispersion Relation

In the present study, we are interested in the frequency versus wavenumber relationship of waves whose wave fronts propagate along the longitudinal z -axis of the rod or tube. The

wavenumber is the magnitude of the wavevector, $\mathbf{k} = k_z$ with the subscript z dropped for convenience. Unlike dispersion relations derived from lattice dynamics, the elastic dispersion relations are derived assuming continuum theory and lack upper bounds on the wavenumber. For use as the phonon dispersion relation, the continuum based dispersion relations are modified by multiplying every mode by²³

$$\frac{\sin(k d/2)}{(k d/2)}. \quad (33)$$

For simplicity, the conventional unit cell length is chosen to be half the lattice constant of diamond, to approximate a carbon-based material with one atom per unit cell¹³. While it is impossible to accurately choose a unit cell of a diamond lattice that contains one atom per basis, the chosen lattice constant is deemed suitable given the perspective of this investigation. The modification given by Eq. (33), forces the slope of the lowest dispersion branch to be zero at a wavenumber equal to $k_{max} = \pi/d$. If the approximated dispersion relation is reflected about the frequency axis, i.e., $\omega(k) = \omega(-k)$, the modified elastic dispersion relation better approximates a phonon dispersion relation by enforcing a periodic boundary condition every $2\pi/d$ wavenumbers.

The frequency equations for $\gamma = 0$ and $\gamma = 0.5$, have an infinite number of (n,m) solutions. The calculation of thermal properties is performed by selecting n and m such that the total number of phonon branches equals three times the number of atoms in the nanotube or nanowire cross-section to account for the three translational degrees of freedom of each atomic oscillator. All phonon branches are sorted from lowest to highest cutoff frequency and subsequently renamed using subscript α ($\alpha = 1, 2, 3 \dots$). The maximum value of α is chosen as 7530 for the nanowire ($\gamma = 0$) and 3897 for the nanotube ($\gamma = 0.5$).

5. Calculation of Specific Heat, Ballistic Conductance, and Thermal Conductivity

The contribution toward the internal energy per unit volume, $U(T)$, from each α phonon branch is summed²⁴.

$$U(T) = \frac{1}{\pi A} \sum_{\alpha} \int_0^{\pi/d} \frac{\hbar \omega(\alpha, k)}{\exp(\beta \hbar \omega(\alpha, k)) - 1} dk \quad (34)$$

where A is the cross-sectional area of the nanowire or nanotube, and $\beta = 1/k_b T$. The limits of integration in Eq. (34) are normally from $-\pi/d$ to π/d . However, due to the symmetry of the first Brillouin zone, the integral is doubled and taken from 0 to π/a .

According to the Bose-Einstein distribution function (denominator of integrand in Eq. (34)), a greater population of phonons occupy lower energy states at a particular temperature. More specifically, the distribution function, gives the average phonon population of energy states $\hbar \omega$ at a given temperature ($k_b T$). With increasing temperature the distribution function permits lower energy states (mode frequencies) to be populated prior to higher energy states.

Phonon confinement that results in the reduction of phonon mode frequencies, and thus phonon branches (mode softening), result in a greater number of populated lower phonon modes at a particular temperature²⁵. The lower frequency phonon modes, because of their greater phonon population, will increase internal energy (and thus specific heat) as compared to the less populated higher frequency modes. Moreover, the effects of phonon confinement on thermal properties become more pronounced when the shifted phonon branches are those of an already lower frequency since the lower frequency phonon modes are occupied by a greater average number of phonons. Therefore it is of interest to identify which phonon branches are more

susceptible to the inclusion of acoustically stiffened surfaces and or acoustically mismatched coatings.

Specific heat (per unit volume) is determined by differentiating Eq. (34) with respect to temperature:

$$C(T) = \frac{1}{\pi A k_B T^2} \sum_{\alpha} \int_0^{\pi/d} \frac{\hbar^2 \omega(\alpha, k)^2 \exp(\beta \hbar \omega(\alpha, k))}{(\exp(\beta \hbar \omega(\alpha, k)) - 1)^2} dk \quad (35)$$

The ballistic conductance in the z -direction corresponds to phonon transport occurring with a mean free path (λ) equal to the length of the structure:

$$g(T) = \frac{A}{2} \sum_{\alpha} \int_0^{\pi/d} C(\alpha, k, T) v(\alpha, k) dk, \quad (36)$$

where $v(\alpha, k)$ is the phonon group velocity. The group velocity is defined as the slope of the α phonon branch (mode) at wavenumber k . Ballistic thermal conductance is dependent on phonon confinement effects as well as the phonon group velocity. Specific heat and ballistic thermal conductance reveal differences in geometric phonon confinement (or simply geometric effects) via the phonon dispersion relations since these quantities do not require an additional assumption regarding the scattering nature of phonons through either a phonon relaxation time τ , or a phonon mean free path λ , where for an individual phonon, $\lambda = v\tau$.

Often in many phonon dynamic simulations an effective relaxation time of all phonons, τ_{eff} , can be linked to various individual scattering mechanisms using Mathiessen's rule

$$\tau_{eff}^{-1} = \tau_{boundary}^{-1} + \tau_{umklapp}^{-1} + \tau_{impurity}^{-1}, \quad (37)$$

In the present study, the boundary scatter term, τ_{eff} is described by,

$$\tau_{boundary}^{-1} = (1-p) \frac{v(\alpha, k)}{D}, \quad (38)$$

where p is the specularity parameter ranging from 0 to 1. $p = 1$ is complete specular (non-resistive) and $p = 0$ is complete diffuse (resistive) phonon scattering. Specular scattering is assumed not to resist phonon propagation since the overall phonon momentum is conserved²⁴. The boundary relaxation time is largely governed by the length dimension term, D , taken as the nanowire diameter, or the nanotube wall thickness. The phonon relaxation times corresponding to Umklapp and impurity scattering are taken to be of the form

$$\tau_{umklapp}^{-1} = C_1 T \omega(\alpha, k)^2 e^{-C_2/T} \quad (39)$$

$$\tau_{impurity}^{-1} = C_3 \omega(\alpha, k)^4 \quad (40)$$

The constants in the Umklapp and impurity relaxation times, $C_1 = 1.73 \times 10^{-19}$, $C_2 = 137.3$, and $C_3 = 1.32 \times 10^{-45}$ are chosen as representative values. These values have been previously used to obtain the thermal conductivity of bulk monocrystalline silicon⁵.

The thermal conductivity of the nanowire or nanotube structure, in terms of the assumed effective relaxation time is given by

$$\kappa(T) = \frac{1}{2\pi\beta T} \sum_{\alpha} \int_0^{\pi/d} \frac{\hbar^2 \omega(\alpha, k)^2 \exp(\beta \hbar \omega(\alpha, k))}{(\exp(\beta \hbar \omega(\alpha, k)) - 1)^2} v(\alpha, k)^2 \tau_{eff} dk. \quad (41)$$

which is of the form $\kappa = C v \lambda^{21, 24}$, but computed using the summation of contributions from each phonon branch integrated over the first Brillouin zone.

6. Results and Discussion

Figures 3 and 4 depict a portion of the dispersion branches, prior to the application of Eq. (33), for the nanowire ($\gamma = 0$) and nanotube ($\gamma = 0.5$) both in the presence (*dashed black lines*) and absence (*solid red lines*) of the acoustically stiffened BOLS layer(s). The non-dimensional frequency ranges are chosen for two reasons. First, convenience in visualizing changes in phonon confinement due to the presence of the BOLS layer(s) given the large numbers of branches computed, and secondly, to highlight the more accurate low frequency region of the dispersion relation. The continuum approximation is most valid at lower frequencies where phonon confinement occurs due to the dominant phonon wavelength being comparable to the diameter of the nanowire or nanotube ²¹. At temperatures approaching the Debye temperature, full lattice dynamic calculations are more appropriate for calculating high frequency phonon branches since the dominant phonon wavelength is of the order of the lattice constant of the crystal. Therefore at increased temperatures, a continuum analysis of the crystal becomes decreasingly valid. Moreover when the dominant phonon wavelength of the system becomes smaller than the diameter of the nanowire, or wall thickness of the nanotube, phonon confinement effects vanish ²⁵. In the present study, the prediction of all thermal properties is performed to a maximum temperature of 600 K, which is well below the Debye temperature of carbon. A comparison to experimental data would be necessary to ascertain the exact temperature limit at which a continuum approximation of the crystal lattice is most valid, but that analysis is beyond the scope of the present investigation.

Figure 5 displays the total number of phonon branches existing within a frequency window having a width of $0.02 \omega R_o/c_{ol}$ and spanning from $\omega R_o/c_{ol} = 0$ to 80. The window size is arbitrarily chosen but remains constant for each set of dispersion curves investigated. A formal density of states (DOS) calculation is not performed since the modeled nanotube is

infinitely long, *i.e.*, significantly longer than the phonon mean free path. A DOS calculation would require a count of the total number of phonon modes within a frequency range ω and $\omega + \Delta \omega$. But since a crystal length is not assumed, the wavevector spacing of the phonon modes are infinitesimally close together instead of having a $2\pi/L$ spacing²⁴. Therefore, instead of a DOS calculation, Fig. 5 counts the number of phonon branches versus individual modes to avoid tallying the number of phonon modes within each branch. Figure 5 is a useful tool for identifying which geometry creates a greater number of phonon branches at a particular frequency.

6.1. Nanowire Results

The presence of a larger numbers of phonon modes and therefore branches, especially at lower frequencies, is expected to increase specific heat, ballistic thermal conductance, and thermal conductivity. In the case of the nanowire, the outer stiffened BOLS affected surface layer (the $\delta/R_o = 0.107$ case) is found to decrease the frequency of the long wavelength (low wavenumber) branches for normalized frequencies $\omega R_o/c_{ol} < 5$ (Fig. 3 inset). Figure 3 also indicates that higher order (larger α) small wavenumber branches show a transition to higher frequency in the presence of the acoustically stiffened outer layer. The transition to higher frequency is most noticeable in short wavelength (large wavenumber) modes and is also reflected by a reduction of phonon branches in $10 < \omega R_o/c_{ol} < 23$ frequency range (Fig. 5 inset). This shift to high frequencies is likely due to the general increase in wave velocities as shown by Fig. 3. The slight reduction in the number of phonon branches for $10 < \omega R_o/c_{ol} < 23$ likely result in the reduction in specific heat, and thus ballistic thermal conductance, and thermal conductivity

in the presence of the acoustically stiffened outer surface of the nanowire for temperatures below approximately 140 K (Fig. 6a).

Figure 6a also suggests that the increase in phonon branches for normalized frequencies greater than $24 \omega R_o/c_{ol}$, as shown by Fig. 5 in the case of the nanowire with the acoustically stiffened outer surface, leads to the significant increase in specific heat, ballistic thermal conductance, and thermal conductivity for temperatures greater than 140 K. Because the total number of phonon branches is the same for the nanowire with the acoustically stiffened skin (BOLS skin) and without the acoustically stiffened skin, the increase in the number of phonon branches for normalized frequencies greater than $24 \omega R_o/c_{ol}$ is due to a shift of phonon branches from higher to lower frequencies. The shift in frequency explains the increase in specific heat, which is found to increase by up to 48 % at 460 K. The lesser percent increase in ballistic thermal conductance and thermal conductivity of the nanowire is likely due to the greater numbers of contributing high frequency phonon branches having near zero to negative group velocities, similar to the optical modes present in lattice dynamic calculations.

The relative change in specific heat and ballistic thermal conductance is reduced following 460 K. Fig. 5 indicates a sharp decrease in the number of phonon branches present for $\omega R_o/c_{ol} > 70$ in the case of the nanowire with an acoustically stiff surface layer and a gradual increase of phonon branches for the nanowire lacking the surface layer. The decrease in the number of BOLS affected nanowire branches and the increase in the number of phonon branches of the non-BOLS nanowire explain the decline in the relative change of specific heat for temperatures greater than 460 K (Fig. 6a). However, this result is likely a manifestation of the continuum approximation, which is less valid at higher temperatures and therefore has limited credibility. However, assuming the complete validity of the continuum assumption at the

temperature range presented, the thermal conductivity is slower to experience then reduction following 460 K because thermal conductivity is a function of the square of the phonon group velocities (Eq. 41), which is found to be elevated for nanowires with stiffened surfaces (Fig. 3).

While it is admittedly difficult to analyze the physical meaning of an individual phonon branch, it is worth noting that the acoustic phonon branches ($m = 0$ for both $n = 0$ and $n = 1$) (Fig. 3a and 3b, respectively) experience a noticeable increase in frequency corresponding to the phonon modes, and thus in wave-speed for wavenumbers $kR_o > 10$. This equates to wavelengths smaller than 1/10 of the outer circumference of the structure or smaller than 2π times the width of the stiffened surface (considering the width of the stiffened surface layer is approximately $R_o/10$). This shift is plausibly due to the modes becoming confined to the stiffer outer surface layer that has a greater longitudinal and transverse sound speed compared to the core material. For acoustic modes ($\omega R_o/c_{oI} \rightarrow 0$ for $kR_o \rightarrow 0$) whose wavelengths are comparable to or larger than the outer circumference of the structure ($kR_o \leq 1$), the phonon dispersion relations are nearly equivalent (Fig. 3). This behavior is not surprising since these waves are expected to be geometrically confined, *i.e.*, too ‘large’ to occupy the acoustically stiffened BOLS affected region.

6.2. Nanotube Results

Figure 5 indicates that when the inner and outer surfaces of the nanotube ($\gamma = 0.5$) are acoustically stiffened, the phonon branches experience a shift to higher frequencies. The shift is plausibly due to an average increase in each modes group velocity. Figure 5 reveals that a more subtle difference occurs in the number of phonon branches versus normalized frequency for the nanotube compared to the nanowire when the surfaces of these structures become acoustically

stiffened. However, inspection of Fig. 4 reveals how drastically different phonon branch shapes are created when the stiffened surfaces are attached to both the inner and outer nanotube. These newly created branches are seemingly non-analogous to the branches present in the non-BOLS affected nanotube and readily appear for $m > 3$ for $n = 0$, and $m > 2$ for $n > 1$. The only similarly existing branches are the long wavelength ($kR_o \geq 1$) low frequency acoustic branches ($\omega R_o/c_{ol} \rightarrow 0$ for $kR_o \rightarrow 0$). These acoustic modes are geometrically confined to the length of the nanotube/nanowire structures due to their long wavelengths being larger than the structures circumference or diameter/wall-thickness. Due to the confinement of acoustic phonon modes, these phonons do not recognize the presence of the stiffened surface layers.

The relative change in specific heat, ballistic thermal conductance, and thermal conductivity of the nanotube is negative throughout the entire range of temperatures investigated (Fig. 6b). The higher frequency shift in the DOS of the BOLS affected nanotube reduces specific heat since higher frequency phonon branches have a smaller occupation of phonons as described by the Bose-Einstein distribution function. A 16 % reduction in specific heat at 300 K is predicted for a nanotube with acoustically stiffened surfaces. Ballistic thermal conductance and thermal conductivity do not experience the same degree of reduction due to their dependency on the increased phonon group velocities which are readily apparent for nondimensional wavenumber $kR_o \geq 10$ (Fig. 4). As discussed, modes having wavenumbers in this regime have wavelengths capable of populating the width of the BOLS affected stiffened surface layer. With increasing temperature, the increased phonon group velocities attempt to recover the loss of ballistic thermal conductance and thermal conductivity caused by the reduction in available phonon branches. Near room temperature, the results indicate an approximate 6 % decrease in thermal conductivity for the nanotube with acoustically stiffened surfaces. Comparison of the

trend between ballistic conductance and thermal conductivity indicates that these two quantities remain within 2 % of one another throughout the temperature domain studied (Fig 6b). While the use of Eq. (33) is believed to increase the accuracy of the model, especially for higher wavenumber/frequency modes, it is difficult to conjecture a valid hypothesis based on a 2 % variation.

7. Conclusion

A model to capture the effects of increased surface moduli on specific heat, ballistic thermal conductance, and thermal conductivity of nanowires and nanotubes is presented. Of the three thermal properties investigated, our results indicate that the specific heat of a nanowire and nanotube is the most sensitive thermal property to surface modification, *i.e.*, surface stiffening. The thermal conductivity of the nanowire and nanotube having acoustically stiffened surface(s) remained within 10 % of the thermal conductivity of the nanostructure lacking surface modification. While a 10 % variation may seem insignificant, our simplified model suggests that a more advanced study of the topic is warranted that would contain variations of the elastic properties of the core and or coating materials. Such models might include the effect of lattice anisotropies, which would permit the analysis of more specific materials, as well as more complex geometries.

Unfortunately, there are little to no experimental data available of specific heat and thermal conductivity for nanowires and nanotubes having diameters less than 5 nm. Moreover, the effect of varying boundary conditions on individual nanowires and nanotubes of these dimensions is best left to theoretical comparisons until more advanced measurement and synthesis techniques are developed.

The most accurate model for the acoustic stiffening of surfaces may be molecular dynamic simulations, where surface stiffening effects are implicitly accounted for in the simulations. However, the consequence of omitting surface modification may be best captured through the comparison of such atomistic models to elasticity theory as presented in this investigation.

The present study also supports the small body of work that investigates the use of acoustically stiffened and/or softened surface coatings using chemical functionalization to tune thermal conductivity in nanostructures with varying geometry. The results of this study suggest that surface modulus modification (stiffening) of the inner surface of a nanostructure will shift the available phonon modes to higher frequency thus reducing thermal conductivity. Similarly, based on the acoustic stiffening results of the nanowire's outer surface, it is plausible that the opposite effect can be achieved, *i.e.*, a reduction in thermal conductivity, if an acoustically soft material is bonded to the outer nanowire surface. Moreover, considering these two conditions, one might expect that the lowest thermal conductivity reduction may be possible using nanotubes with acoustically stiffer inner coatings and acoustically softer outer surface coatings. Thermal conductivity reductions created by phonon confinement effects due to surface coatings will undoubtedly be compounded by increased phonon boundary scattering. Validation of these hypotheses are currently underway.

The relationship between phonon confinement effects and thermal properties is fairly well understood. Understanding how to alter phonon confinement seems to be the next logical step in engineering more efficient thermoelectric and thermal management materials.

ACKNOWLEDGEMENTS

The authors would like to acknowledge the support of the Air Force Office of Scientific Research (AFOSR) grant FA9550-08-1-0372 for conducting this research.

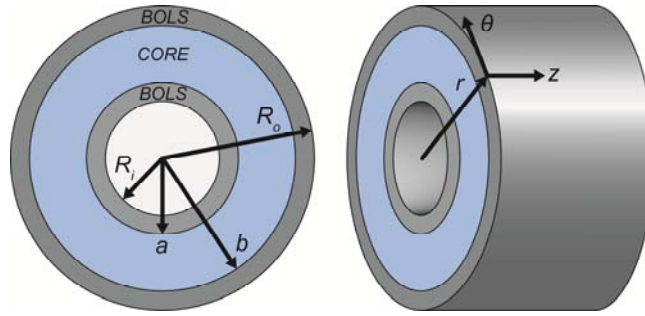


Figure 1: Schematic diagram of core skin structure nanotube. For all structures investigated $R_o = 5\text{nm}$ is maintained. The acoustically stiff surfaces (BOLS affected layers) are applied to the inner and outer tube walls and has a thickness of $\delta = 0.534\text{ nm}$ (3 atomic layers). The nanowire is similarly modeled except with $R_i = a = 0$. The models are compared to nanowires and nanotubes lacking stiffened surfaces ($a = R_i$, $b = R_o$ for the nanotube and $a = R_i = 0$, $b = R_o$ for the nanowire).

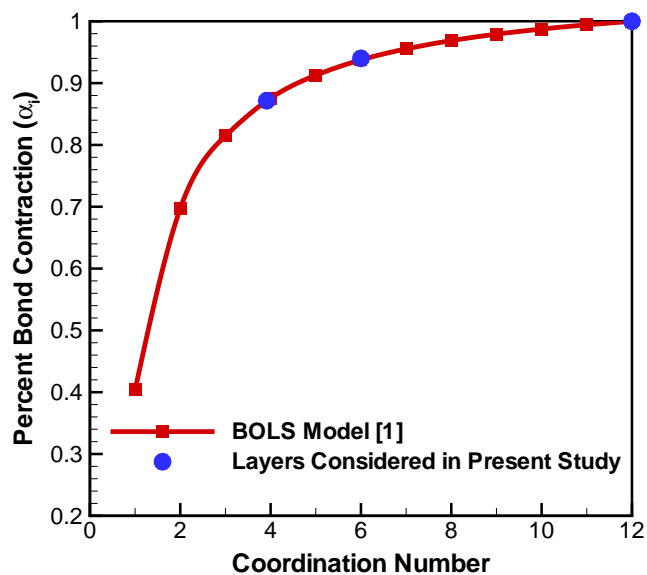


Figure 2. BOLS Model for bond contraction as a function of atomic coordination number. The coordination numbers are assumed to decrease in the first 3 atomic layers exposed to a free surface. Beginning at the surface, the coordination numbers used in the present study are approximately 3.91, 6, and 12 (*blue circles*). The 3rd most atomic layer from the surface has a coordination number of 12 and is therefore assumed to belong to the bulk medium of an FCC structure. *C.Q. Sun, S. Li, and C.M. Li, The Journal of Physical Chemistry B* **109**, 415 (2005).

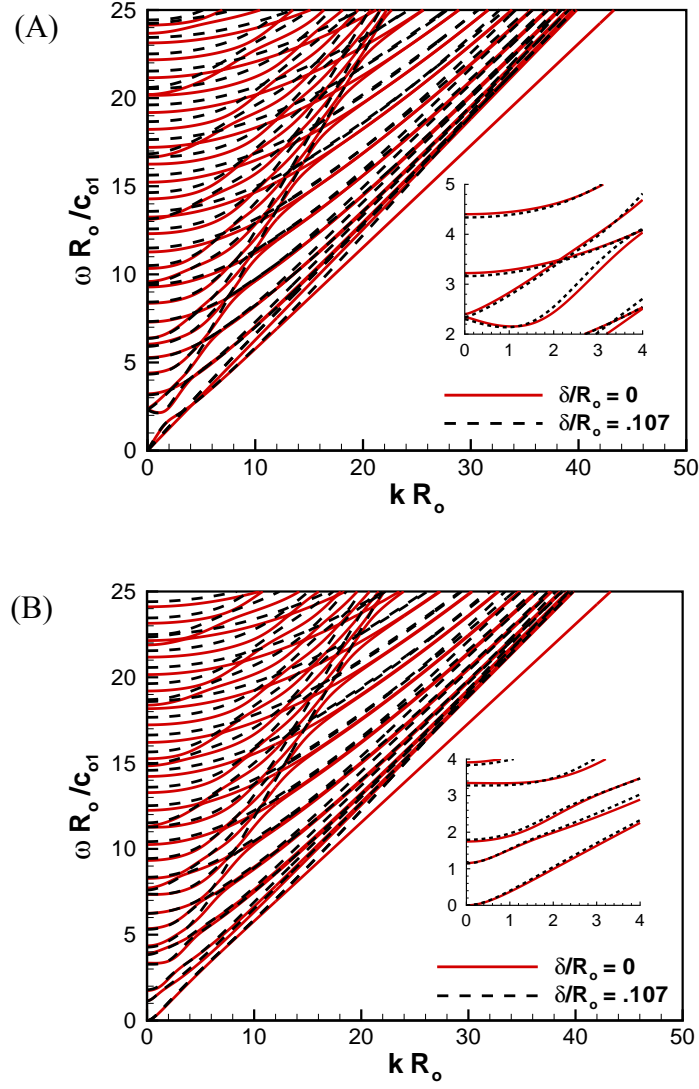


Figure 3. Elastic dispersion relations for the solid rod ($\gamma = 0$) for the non-BOLS affected case ($\delta/R_o = 0$) (*solid red lines*) and the BOLS-affected case ($\delta/R_o = 0.107$) (*dashed*). (a) $n = 0$ combination of both torsional and longitudinal modes. (b) $n = 1$ flexural modes. In the BOLS-affected case, the acoustically stiffened skin thickness is $\delta = 0.534$ nm.

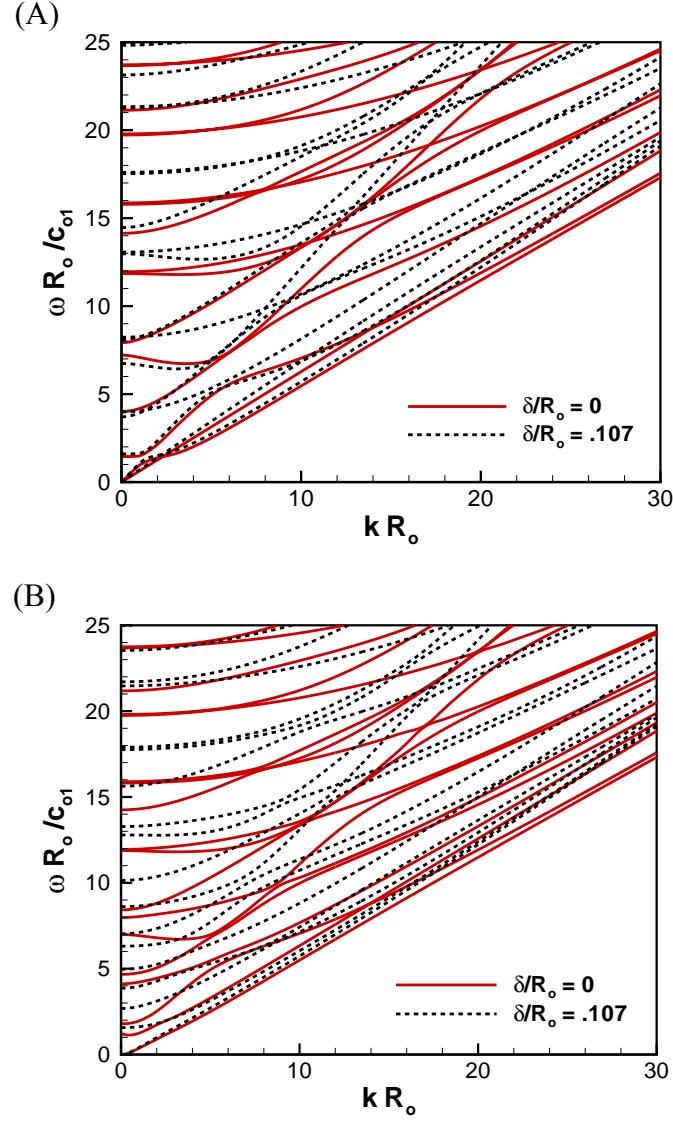


Figure 4. Elastic dispersion relations for the tube ($\gamma = 0.5$) for the non-BOLS affected case ($\delta/R_o = 0$) (solid red lines) and the BOLS-affected case ($\delta/R_o = 0.107$) (dashed). (a) $n = 0$ combination of both torsional and longitudinal modes. (b) $n = 1$ flexural modes. In the BOLS-affected case, the acoustically stiffened skin thickness is $\delta = 0.534$ nm.

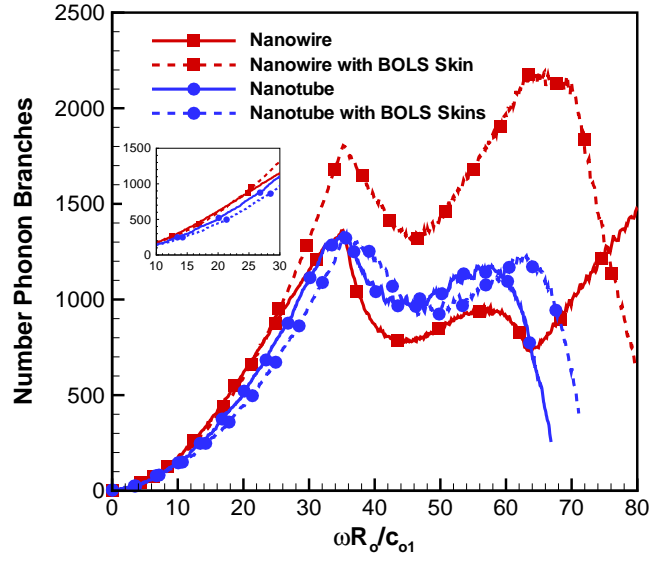


Figure 5. Number of phonon branches as function of non-dimensional frequency for a nanowire (*red squares*) and nanotube (*blue circles*) having a 5 nm outer diameter. The nanotube wall-thickness is 2.5 nm. The BOLS skin layer refers to an acoustically stiffened material bonded to the outer wall of the nanowire and both the outer and inner walls of the nanotube. The inset is shown with the same units and depicts the nanowire and nanotube with and without the BOLS affected skin layer (s).

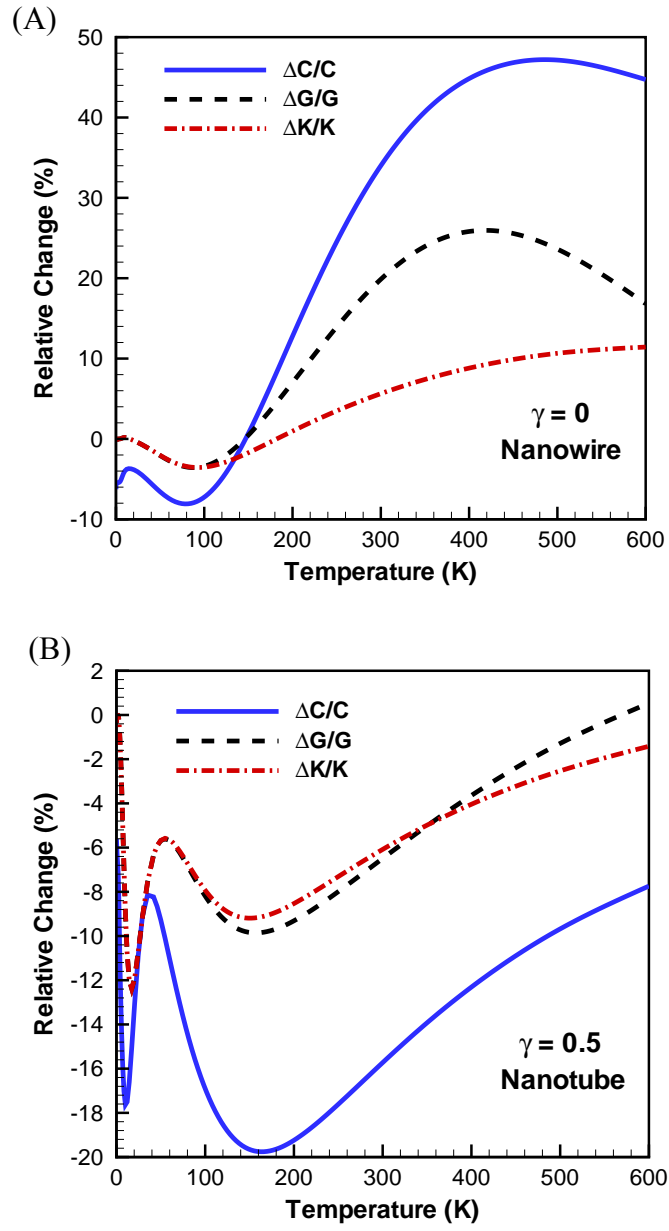


Figure 6. Relative change in specific heat ($\Delta C/C$), ballistic thermal conductance ($\Delta G/G$), and thermal conductivity ($\Delta K/K$) as caused by the presence of BOLS hardened surface(s) for (a) The nanowire ($\gamma = 0$); (b) The nanotube ($\gamma = 0.5$).

REFERENCES CITED

1. C. Q. Sun, S. Li, and C. M. Li, The Journal of Physical Chemistry B **109**, 415 (2005).
2. T. C. Au Yeung, C. Q. Sun, T. C. Chiam, R. Ramanathan, W. Z. Shangguan, and C. H. Kam, Journal of Applied Physics **98**, 104308 (2005).
3. Z. Linli and Z. Xiaojing, EPL (Europhysics Letters) **88**, 36003 (2009).
4. T. C. Au Yeung, M. Gu, C. Sun, G. Chen, D. Wong, and V. Nosik, Physical Review B **74**, (2006).
5. N. Mingo, Physical Review B **68**, 113308 (2003).
6. N. Mingo, L. Yang, D. Li, and A. Majumdar, Nano Letters **3**, 1713 (2003).
7. N. Mingo and D. A. Broido, Physical Review Letters **93**, 246106 (2004).
8. J. Zou and A. Balandin, Journal of Applied Physics **89**, 2932 (2001).
9. R. Chen, A. I. Hochbaum, P. Murphy, J. Moore, P. Yang, and A. Majumdar, Physical Review Letters **101**, (2008).
10. P. G. Klemens, *Thermal Conductivity and Lattice Vibrational Modes*, in *Solid State Physics*, S. Frederick and T. David, Editors. (Academic Press, 1958).
11. Y. Chen, D. Li, J. R. Lukes, and A. Majumdar, Journal of Heat Transfer **127**, 1129 (2005).
12. X. Lu, J. H. Chu, and W. Z. Shen, Journal of Applied Physics **93**, 1219 (2003).
13. T. Tong, R. Prasher, and A. Majumdar, ASME Conference Proceedings **2007**, 631 (2007).
14. R. Prasher, T. Tong, and A. Majumdar, Nano Letters **8**, 99 (2008).
15. F. Song, G. L. Huang, and V. K. Varadan, Acta Mechanica **209**, 129 (2009).

16. O. M. Mukdadi, S. K. Datta, and M. L. Dunn, *Journal of Applied Physics* **97**, 074313 (2005).
17. E. Pokatilov, D. Nika, and A. Balandin, *Physical Review B* **72**, (2005).
18. E. Pokatilov, D. Nika, and A. Balandin, *Superlattices and Microstructures* **38**, 168 (2005).
19. E. Pokatilov, *Journal of Applied Physics* **95**, 5626 (2004).
20. J. Zou, X. Lange, and C. Richardson, *Journal of Applied Physics* **100**, 104309 (2006).
21. N. Ashcroft and D. Mermin, *Solid State Physics*. (Thomson Learning, Inc., 1976).
22. K. F. Graff, *Wave Motion in Elastic Solids*. (Dover Publications, New York, NY, 1991).
23. T. Tong, R. Prasher, and A. Majumdar. Heat Capacity and Thermal Conductance for Non-Metallic Crystalline Nanowires Based on Elastic Dispersion Relations. in *Proceedings of IMECE2007*. 2007. Seattle, Washington: ASME.
24. C. Kittel, *Introduction to Solid State Physics*. (Wiley Ltd., 2004).
25. M. F. P. Bifano, P. B. Kaul, and V. Prakash, *Nanotechnology* **21**, 235704 (2010).